



universität
wien

MASTERARBEIT / MASTER'S THESIS

Titel der Masterarbeit / Title of the Master's Thesis

**MRI Microscopy on Biocompatible Materials and
Polymers with Short T_2^* Times:
Validation and Quality Control of UTE Pulse Sequences
for Short Detection Times on a Microscopy Insert to a
High-Field Human MR Scanner**

verfasst von / submitted by

Fabian Valka, BSc

angestrebter akademischer Grad / in partial fulfilment of the requirements for the degree of

Master of Science (MSc)

Wien, 2015 / Vienna 2015

Studienkennzahl lt. Studienblatt /
degree programme code as it appears on
the student record sheet:

A 066 876

Studienrichtung lt. Studienblatt /
degree programme as it appears on
the student record sheet:

Masterstudium Physik UG2002

Betreut von / Supervisor:

Ao. Univ.-Prof. Dipl.-Phys. Dr. Andreas Berg

Zusammenfassung

Einleitung: Die Magnetresonanztomographie ist eine der wichtigsten bildgebenden Verfahren in der Medizin. Sie wird für ein breites Spektrum von Anwendungsfällen, besonders zur Kontrastierung von Weichgewebe, herangezogen. Viele “Software”-Messprotokolle (“Sequenzen”) sind für klinische Anwendungen verfügbar, diese sind aber hauptsächlich auf Messungen von Proben mit langen Zerfallszeiten ($T2^*$) ausgelegt. Teile des menschlichen Körpers wie Sehnen, die Substantia compacta, die Menisci, Zähne und viele mehr, besitzen sehr kurze $T2^*$ -Zeiten. Das Gleiche gilt für Kompositwerkstoffe, welche in der Medizin und darüber hinaus verwendet werden. Ultrashort TE (UTE) Sequenzen besitzen TE-Zeiten, welche um einen Faktor 10 bis 20 kleiner sind als die von Sequenzen, welche derzeit im klinischen Bereich verfügbar sind.[1] Microimaging ist MR-Bildgebung mit sehr hohen Auflösungen bis in den mikroskopischen Bereich ($< 100\mu m$) hinein. Microimaging wird sowohl auf spezialisierten Systemen als auch auf Zusätzen für Ganzkörperscanner durchgeführt. Der Microimaging-Einschub ermöglicht die Messung mit Auflösungen, welche sonst auf einem Ganzkörperscanner nicht möglich wären. Die Kombination von UTE und einem Microimaging-Zusatzsystem auf einem Ganzkörperscanner erlaubt es, sehr feine Strukturen und Defekte in Geweben und Materialien mit kurzen $T2^*$ Zeiten sichtbar zu machen. **Methodik:** Es wurde eine spezielle Teststruktur (“Phantom”), gefüllt mit Silikon, welches eine $T2^*$ Zeit von $(11.6 \pm 1.1)ms$ besitzt, entwickelt. Dieses enthält verschiedene Strukturen für die Auflösungsmessung mittels Edge Spread Function (ESF) und Point Spread Function (PSF). Das Phantom enthält außerdem Bereiche zur Schichtdickenmessung, zur Messung der geometrischen Verzerrung und zur Signal-Rausch-Verhältnis (“Signal to noise ratio”) Messung. Standard Protokolle wurden für die untersuchten Sequenzen definiert, um einen direkten Vergleich der Sequenzen zu ermöglichen. Messungen mit den XD VTE, CV UTE und DA-3DPR Sequenzen wurden am Exzellenzzentrum für Hochfeld-MR der Medizinischen Universität Wien durchgeführt. Vergleichsmessungen mit den Bruker UTE3D und Zero TE (ZTE) Sequenzen wurden am Institut für Molekulare Biotechnologie der österreichischen Akademie der Wissenschaften auf einem 15.2T vorklinischem Bruker System durchgeführt. **Ergebnisse:** UTE-, ZTE- und VTE-Sequenzen zeigen starke Artefakte, diese werden hauptsächlich durch Kantenanhebung verursacht und sind auf k-Raum Pfadfehler zurückzuführen. Diese Fehler werden durch die Abweichung der realen von der idealen Gradientenleistung verursacht. Korrekturen für diese Artefakte wurden zwar bereits umgesetzt[2, 3], sind aber systemspezifisch und nicht ohne weiteres zum direkten Einsatz bei UTE-Messungen verfügbar. Die besten Ergebnisse wurden mit der XD VTE Sequenz erreicht, mit einer Auflösung von $(103.02 \pm 0.80)\mu m$ bei Pixelgrößen von $62.5\mu m$ und einem SNR (ROI) von 40.88 ± 0.35 . Für UTE Sequenzen wurden die besten Resultate mit der DA-3DPR Sequenz erzielt, eine Auflösung von $(446.5 \pm 8.9)\mu m$ (ESF-MTF), bei einem SNR von 9.175 ± 0.041 (ROI) / 20.79 ± 0.15 (NEMA Differenzbildmethode[4]) und einer Pixelgröße von $125\mu m$ konnten demonstriert werden.

Abstract

Background: Magnetic resonance imaging has become one of the most important medical imaging methods. It is used in a wide area of pathologies especially related to soft tissue, e.g. tumors. Although many different sequences are available for clinical applications, these sequences are mainly focused on measurements of soft tissues with long $T2^*$ times.[1] Some parts of the human body, like tendons, cortical bone, menisci, teeth and many more, are mostly made up of components with short $T2^*$ times. This also holds true for composite materials used in medicine and beyond. Ultrashort TE (UTE) sequences have echo times about 10 to 20 times shorter than what is available on current clinical whole body mr scanners.[1] Microimaging is mr imaging at microscopic or better resolutions. This is performed using both dedicated systems and speciality inserts for whole body scanners. The micro imaging gradient insert enables the use of a whole body scanner at resolutions which are unachievable using the scanner by itself. Usage of UTE imaging with a micro gradient insert on a whole body scanner enables visualization of very small structures and defects in tissues and materials with short $T2^*$ times.

Methods: A special microimaging phantom filled with silicone, which has a short $T2^*$ time of $(11.6 \pm 1.1)ms$, has been constructed. This phantom contains multiple structures for resolution measurements using both point spread function and edge spread function analysis. The phantom also includes structures for slice thickness measurements in one direction, geometric accuracy and signal to noise ratio. Standard protocols were defined for the sequences under investigation to enable direct comparison of the resulting data. Measurements using the XD VTE, CV UTE and DA 3DPR sequences have been performed on a micro gradient insert to a 7T high field whole body scanner at the MR center of excellence, Medical University of Vienna. Comparison measurements employing different UTE and Zero TE (ZTE) sequences have also been performed, at the Institute for Molecular Biology of the Austrian Academy of Sciences (IMBA), on a 15.2T Bruker pre clinical imaging system.

Results: UTE, ZTE and VTE sequences produce strong artefacts in their images, mostly due to edge enhancement caused by k-space trajectory errors from non ideal gradient performance. While correction methods, which improve these artefacts, have been implemented before[2, 3] these remain specific to certain systems and are not easily employed in regular UTE measurements. The best results have been achieved using the XD VTE sequence with resolutions up to $(103.02 \pm 0.80)\mu m$ at pixel sizes of $62.5\mu m$ and SNR (ROI based) of 40.88 ± 0.35 . Using UTE sequences the best results achieved were resolutions of $(446.5 \pm 8.9)\mu m$ (ESF-MTF), at a SNR of 9.175 ± 0.041 (ROI) / 20.79 ± 0.15 (NEMA differences[4]) and pixel size of $125\mu m$ using the DA-3DPR sequence.

Acknowledgements

First and foremost I would like to thank my adviser Prof. Andreas Berg for his patience and support on my masters thesis and beyond. His scientific vision of the world and integrity as well as wealth of knowledge always served as an inspiration to me.

I would also like to thank Joachim Friske for his help during the practical work for this thesis.

Without X. Deligianni and A. Nagl this thesis would not have been possible. Special thanks to them for making their XD VTE and DA 3DPR sequences available to this research project. Thanks to Siemens for making the CV UTE sequence available as a work in progress (“WIP”) package.

Jelena Zinnanti and Lydia Zopf allowed me to perform measurements at the 15T pre clinical imaging system at the Institute for Molecular Biology of the Austrian Academy of Sciences, thank you for this opportunity and making this comparison possible.

Thanks to Lars G. Hanson for giving me permission to use his figures of nuclear spin ensembles in my introductory chapter.

My good friends Carla Schuler, Michaela Kirsch, Moritz Cizek, Bernhard Fischer, Alina Huber, Anna Hofmann, Rita Ertl and Walter Kraus as well as my parents Waltraud Valka and Karl Valka supported me throughout this endeavour, thank you!

Contents

Zusammenfassung	iii
Abstract	v
Acknowledgements	vii
Contents	ix
List of Figures	xv
List of Tables	xxiii
Abbreviations	xxv
Symbols	xxvii
1 Introduction	1
1.1 Introduction to Magnetic Resonance Imaging	1
1.1.1 Relaxation	4
1.1.1.1 T1 Relaxation	5
1.1.1.2 T2 Relaxation	6
1.1.1.3 T2* Relaxation	7
1.1.2 Sequences	7
1.1.3 Image Generation	7
1.1.4 Gradient Echo Sequence	11
1.2 Ultrashort TE Imaging	11
2 Methods	15
2.1 Image Reconstruction from DICOM	15
2.2 Error Estimation	16
2.3 Signal to Noise Ratio	16
2.3.1 Region of Interest Selection	17
2.3.2 Correction for Fourier Reconstruction	17
2.3.3 NEMA Difference Images Method	17
2.4 Resolution	18
2.4.1 Edge Spread Function	18
2.4.2 Point Spread Function	22
2.5 Ringing and Edge Overshoot Artefacts	23
2.6 Geometric Accuracy	24

2.7	Slice Thickness	26
2.8	Mathematica Analysis Toolkit	28
2.8.1	Settings	28
2.8.2	Validation of the LSF Analysis	30
3	Artefacts	31
3.1	Gibbs Ringing	31
3.2	Edge Enhancement	31
3.2.1	Analysis Method	33
3.3	Blurring	33
3.4	Zero Point Artefact	33
3.5	Susceptibility	34
4	Phantom	35
4.1	Structure	36
4.1.1	Resolution	36
4.1.2	Slice Thickness	37
4.2	Uniformity Phantom	37
4.3	Material	37
4.3.1	Spectrum	37
4.3.2	T1 of the Phantom Silicone Material	38
4.3.3	T2* of the Phantom Silicone Material	40
4.3.4	Uniformity of the Material	41
4.3.5	Air Bubbles	42
5	Measurements	43
5.1	MRI System	43
5.2	Measurement Preparation	44
5.3	Standard Protocol	46
5.3.1	Goal	46
5.3.2	Target Parameters	46
5.4	Parameter Variation	47
5.4.1	Overview of the Result Quantities	47
5.5	Thermal Behavior	48
6	XD VTE	49
6.1	Sequence	49
6.2	Standard Protocol	50
6.2.1	Signal to Noise Ratio using ROIs	50
6.2.2	Signal to Noise Ratio using Difference Images	51
6.2.3	Resolution	52
6.2.3.1	Edge Spread Function	52
6.2.3.2	Edge Spread Function using LSF Fit	54
6.2.3.3	Point Spread Function using Fourier Transform	55
6.2.3.4	Point Spread Function using Gaussian Fits	55
6.2.4	Diameter	56
6.2.5	Results	57

6.3	Thermal Behavior	58
6.4	Parameter Variation	59
6.4.1	Echo Time	59
6.4.2	Averages	60
6.4.3	Matrix Size	60
6.4.4	Bandwidth	62
6.4.5	Filters	63
6.4.5.1	Recommendations	66
6.4.6	Other Settings	66
6.4.7	Settings Which Cause Execution Errors	69
6.5	Artefacts	70
6.5.1	Ringling	70
6.5.1.1	K Space Distortion Simulation	70
6.5.2	Zero Point Artefact	73
6.6	High Resolution	74
6.6.1	Signal to Noise Ratio	74
6.6.2	Resolution using ESF and MTF	75
6.6.3	Results	76
6.7	Slice Thickness	76
7	CV UTE	79
7.1	Sequence	79
7.2	Standard Protocol	80
7.2.1	Signal to Noise Ratio using ROIs	81
7.2.2	Signal to Noise Ratio using Difference Images	81
7.2.3	Resolution	82
7.2.3.1	Edge Spread Function	82
7.2.3.2	Point Spread Function using Gaussian Fit	83
7.2.4	Edge Overshoot	84
7.2.5	Results	85
7.3	Thermal Behavior	87
7.4	Minimum TE	88
7.5	Parameter Variation	88
7.5.1	Echo Time	90
7.5.2	Averages	90
7.5.3	Matrix Size	91
7.5.4	Radial Views	92
7.5.5	Bandwidth	94
7.5.6	Filters	95
7.5.7	Other Settings	98
7.5.8	Settings Which Cause Execution Errors	100
7.6	Artefacts	100
7.6.1	Blurring and Edge Enhancement	100
7.6.2	Zero Point Artefact	100
7.6.3	Ringling or Moire Artefact	101
7.7	Overnight Measurements	102

7.8	Slice Thickness	103
8	DA-3DPR	105
8.1	Sequence	105
8.2	Reconstruction	107
8.3	Standard Protocol	108
8.3.1	Signal to Noise Ratio using ROIs	109
8.3.2	Signal to Noise Ratio using Difference Images	110
8.3.3	Resolution	111
8.3.3.1	Edge Spread Function using MTF	111
8.3.3.2	Point Spread Function using Gaussian Fits	112
8.3.4	Edge Overshoot	113
8.3.5	Results	113
8.4	Thermal Behavior	114
8.5	Parameter Variation	114
8.5.1	Matrix Size in Reconstruction	114
8.5.2	Projections	115
8.5.3	Pulse Duration	116
8.5.4	Pulse Sequence Timing - T_0	117
8.5.5	Settings Which Cause Execution Errors	118
8.6	Artefacts	119
8.6.1	Blurring and Edge Enhancement	119
8.7	Improved Standard Protocol	119
8.7.1	Signal to Noise Ratio using ROIs	120
8.7.2	Signal to Noise Ratio using Difference Images	120
8.7.3	Resolution	121
8.7.3.1	Edge Spread Function using MTF	121
8.7.3.2	Point Spread Function using Gaussian Fits	122
8.7.4	Edge Overshoot	123
8.7.5	Results	123
8.8	Slice Thickness	124
9	IMBA 15.2T	125
9.1	Introduction	125
9.2	Analysis	125
9.3	Measurements	126
9.4	Bruker UTE3D	126
9.4.1	Sequence	126
9.4.2	Measurement	126
9.4.3	Signal to Noise Ratio using ROIs	127
9.4.4	Signal to Noise Ratio using Difference Images	127
9.4.5	Resolution	128
9.4.5.1	Edge Spread Function using Modulation Transfer Function	128
9.4.5.2	Point Spread Function using Gaussian Fits	129
9.4.6	Edge Overshoot	130
9.4.7	Results	130

9.4.8	Artefacts	131
9.4.8.1	Blurring	131
9.4.8.2	Edge Enhancement	131
9.5	Bruker ZTE	132
9.5.1	Sequence	132
9.5.2	Measurement	133
9.5.3	Signal to Noise Ratio using ROIs	133
9.5.4	Signal to Noise Ratio using Difference Images	134
9.5.5	Resolution	135
9.5.5.1	Edge Spread Function using Modulation Transfer Function . . .	135
9.5.5.2	Point Spread Function using Gaussian Fits	135
9.5.6	Edge Overshoot	136
9.5.7	Results	137
9.5.8	Artefacts	137
10	Results	139
10.1	Reliability of Results	139
10.2	Standard Protocols	141
10.3	Resolution	141
10.4	Signal to Noise Ratio	142
10.5	Edge Overshoot and Ringing	144
11	Conclusions & Outlook	147
A	Mathematica Analysis Toolkit	151
A.1	Introduction	151
A.2	Documentation	151
A.2.1	General Functions	151
A.2.2	Signal to Noise Ratio	152
A.2.3	Ringling and Edge Overshoot	152
A.2.4	Resolution	153
A.2.5	Geometric Accuracy	154
A.3	General Functions	155
A.4	Settings	157
A.5	Signal to Noise Ratio	157
A.6	Ringling and Edge Overshoot	157
A.7	Resolution	158
A.7.1	Line Spread Function	158
A.7.2	Edge Spread Function	160
A.7.3	Point Spread Function	161
A.8	Geometric Accuracy	162
A.9	Usage Example	164
A.10	Difference Images SNR	165
A.11	T1 Analysis	166

B Simulations	169
B.1 XD VTE K Space Distortion	169
C Curriculum Vitae	171
 Bibliography	 175

List of Figures

1.1	Nuclear spin ensemble with no external magnetic field (left) and external field applied (right). When the nuclei ensemble is placed inside the external magnetic field they precess with the Larmor frequency and the spatial distribution is shifted towards the external field B_0 and a net magnetization M in z direction can be observed. Image source: Hanson, L.[5], reprinted with his permission.	2
1.2	Explanation of the rotational frame of reference and application of this view to the response of the system to an incoming rf pulse. Image source: Hanson, L.[5], reprinted with his permission.	3
1.3	Signal induced from the rotating net magnetization which was rotated by 90° into the x-y plane.	4
1.4	Free induction decay. The signal observed in MR in the transverse direction after excitation. As measured in the laboratory frame of reference.	4
1.5	T1 relaxation time evolution. Equilibrium value of the magnetization is set to 1.	5
1.6	T2 relaxation time evolution.	6
1.7	Change in Larmor frequency when a gradient is applied to the sample.	8
1.8	Slice selection based on the change in Larmor frequency caused by a gradient applied along the x direction.	8
1.9	Single line of voxels before and after gradient application.	9
1.10	Single line of voxels with a pattern. No gradient field applied.	9
1.11	Single line of voxels with a pattern in a gradient field after some time has passed.	9
1.12	Example of the reconstruction of an image based on patterns/spatial frequencies using the Fourier transform.	10
1.13	2 dimensional pattern of spins in two gradients after some time.	10
1.14	Sequence diagram for a gradient echo sequence.[6] Echo shape based on:[7]. The lines inside the gradients indicate that the measurement is repeated for each combination of different gradient strengths. The whole measurement is repeated for each of these gradient settings.	11
1.15	Radial k-space sampling at multiple points along each spoke. This image is based on the image of radial sampling by Robson M.[1].	12
1.16	Sequence diagram for a UTE sequence as published by Robson M.[1] and Tyler D.[8]. This illustration is based on their sequence illustrations. A half rf excitation pulse is shown. The lines inside the gradients indicate that the measurement is repeated for each combination of different gradient strengths. The whole measurement is repeated for each gradient setting with the slice selection gradient pointing in the opposite direction.	13
2.1	Relationship between different optical transfer functions	19
2.2	Illustration of the effect of the edge spread function	19
2.3	Line profile of an edge for determining the ESF	19

2.4	Line spread function for the ESF in figure 2.3. Scaled to the difference between minimum and maximum of the ESF and divided by the pixel size.	20
2.5	Modulation transfer function for the LSF in figure 2.4.	21
2.6	Effect of the point spread function explained by convolution.	22
2.7	Algorithm for the analysis of the diameter.	25
2.8	Line diameters inside a single slice.	26
2.9	Geometric considerations for the analysis of slice thickness measurements.	27
2.10	Line profile for the calculation of the slice thickness in the XD VTE sequence.	27
2.11	Gaussian function for validation of the LSF analysis method.	30
3.1	Illustrations of the Gibbs phenomenon.	31
3.2	Illustration of an edge enhancement artefact. Digitally altered.	32
3.3	Illustration of a zero point artefact. Digitally altered based on multiple images of the XD VTE sequence.	33
3.4	Artefacts most likely caused by susceptibility differences between the phantom silicone and air bubbles.	34
4.1	Photo of the FV2 silicone filled UTE phantom constructed for this thesis.	35
4.2	Structure of the phantom FV2 as used in this thesis. The views are based on MRI images but have been digitally altered.	36
4.3	Spectrum of the silicone material used inside the phantom. Central frequency 297.222008 MHz. Acquired using the frequency adjustment in the 7T Magnetom MR scanner using the STEAM 10 Hz sequence.	38
4.4	Spin echo sequence for the T1 measurement of the phantom silicone material. Also showing the region of interest used for the T1 fit. The resulting placement was slightly offset from the slice positions displayed on the localizer when setting up the measurement. Therefore the phantom is not directly in the center of the FOV.	39
4.5	Fit of T1 using a partial saturation recovery using a spin echo sequence. This figure shows all 11 slices and their respective fits used in the final calculation of the T1 value of the silicone material.	40
4.6	One of the slices used for the T2 mapping of the silicone filling material used in the phantom.	41
4.7	T2* map for the silicone used in the phantom. Also depicting the ROIs used for the analysis.	41
4.8	Uniform silicone phantom analyzed using a spin echo sequence.	42
5.1	39mm two channel RX/TX 1H resonator produced by RAPID Biomedical used for the XD VTE, CV UTE and DA-3DPR measurements.	43
5.2	Tuning and matching of the coil with the phantom already inserted.	44
5.3	Adjustment procedure used for measurement preparation.	45
6.1	XD VTE sequence diagram and illustration of variable TE. Image source: Deligianni, X.[9]	50
6.2	Regions of interest used for the SNR analysis in the XD VTE sequence.	51
6.3	Difference image of two successive slices used for SNR calculation.	51

6.4	Edge spread function region of interest as well as left and right edge spread functions for the XD VTE standard protocol. Both edge spread function cut outs are scaled to maximum dynamic range inside the cut out.	52
6.5	All 304 modulation transfer functions used for the analysis of the XD VTE standard protocol. The density histogram has a bin size of $0.2\frac{1}{mm}$ on the x-axis and 0.05 on the y-axis. The smooth density histogram was generated using Mathematicas SmoothDensityHistogram function. The 3D histogram shows the number of data points in each bin in its height, this includes more than 304 data points in total due to zero filling. Bin size for the 3D Histogram is $0.3\frac{1}{mm}$ on the x-axis and 0.05 on the y-axis. Please note that these graphs are only shown to illustrate the shape and were not used in any way to obtain the numerical results for the ESF based resolution.	53
6.6	Line spread function obtained from the edge spread function and fitted using a Gaussian function in fityk[10].	54
6.7	Fourier transforms obtained from the point spread functions for 8 different slices in the XD VTE standard protocol. Phantom size $(204.8 \pm 0.2)\mu m$	55
6.8	Point spread function analysis using Gaussian fits in XD VTE. Data points shown are without spline baseline subtraction but with constant baseline adjustment performed by subtracting the average of the data points left of the peak.	56
6.9	Lengths in a single slice of the XD VTE standard protocol used to determine the diameter.	57
6.10	Standard protocol for the XD VTE sequence.	57
6.11	Thermal behavior of the XD VTE sequence as shown in a log-log plot. Temperature increase at TR 200 can be disregarded as a measurement artefact.	58
6.12	Signal drop in XD VTE with echo time of 10ms.	59
6.13	Comparison between pixel sizes and resolution achieved for the XD VTE sequence. Shows that the actual resolution does not remain constant with pixel size. Meaning that an increase in matrix size still provides an improvement of the actual resolution achieved but doubling the matrix size does not double the actual resolution.	61
6.14	MTF for different matrix sizes in the XD VTE parameter variation. Rendered using Mathematicas SmoothDensityHistogram function, using identical axes ranges for easier comparison. Each plot contains 304 modulation transfer functions.	62
6.15	Standard protocol with 512x512 matrix, XD VTE sequence.	62
6.16	Comparison of different bandwidth settings for the XD VTE sequence.	63
6.17	Comparison of different filter settings and their effects on the modulation transfer functions based on the edge spread functions.	64
6.18	Ringing artefact in the XD VTE sequence. The sequence image has been enhanced by increasing the contrast in the brightness range of the ringing. The white line at the 9 o'clock position shows the source of the line profile. X position shown is in pixels and not length units. Pixel size is $125\mu m$ for this image.	70
6.19	Original and manipulated k-space quadrant of the simulation and k-space weighting factors. The central frequency is in the top left corner of the k-space images. Positions are in pixels, the adjustment factor is dimensionless.	71
6.20	Simulation of the k-space distortion due to variable echo time in the XD VTE sequence.	72
6.21	Comparison of the shapes between the line profiles of the simulation result and the line profile found in the XD VTE standard protocol image.	72

6.22	Comparison of the unadjusted simulation with the actual XD VTE standard protocol measurement.	73
6.23	Zero point artefact in the XD VTE sequence. This image does not contain the full dynamic range.	73
6.24	Overnight high resolution measurement, XD VTE sequence.	74
6.25	Regions of interest used for the SNR analysis in the high resolution overnight XD VTE measurement.	75
6.26	Modulation transfer function and the edge spread functions upon which this MTF is based for the XD VTE high resolution overnight measurement.	75
6.27	Cut out of the left upper quadrant of the XD VTE high resolution, overnight measurement, figure 6.24. Showing the two smallest PSF phantom structures and their diameters, estimated error of these diameters is $0.2\mu m$	76
6.28	Slice for the thickness measurment of the XD VTE sequence.	77
6.29	Line profile for the calculation of the slice thickness in the XD VTE sequence. . .	77
7.1	Sequence diagram and illustration of the k-space trajectory as provided in the CV UTE documentation.[11] This image was published by Chan, C.[12], no source is provided in the documentation and the image as shown and published by Chan, C. is available under open access and a permissive licence and was therefore used instead. Image source: Chan, C.[12], published under a CC BY 2.0 licence. . . .	79
7.2	Regions of interest used for the SNR analysis in the CV UTE sequence.	81
7.3	Difference image of two successive slices used for SNR calculation.	81
7.4	Modulation transfer function obtained from the ESF using numerical derivatives of the LSF for the CV UTE sequence. Showing a density histogram of 532 MTFs from 13 slices with bin widths of $0.15\frac{1}{mm}$ in x direction and $0.2\frac{1}{mm}$ in y direction. . . .	82
7.5	Histograms of the resolution results obtained for the CV UTE sequence from ESF-MTF analysis. The histogram on the left hand side has a bin width of 0.1. The one on the right hand side has a bin width of 0.01.	83
7.6	Point spread function analysis using Gaussian fits of the line spread function in CV UTE. Data points shown are without spline baseline subtraction but with constant baseline adjustment performed by subtracting the average of the data points left of the peak.	83
7.7	Line profiles of all lines used for the edge overshoot analysis in the CV UTE sequence. Normalized by dividing each line by the mean inside the edges. . . .	84
7.8	Standard protocol for the CV UTE sequence.	85
7.9	Thermal behavior of the CV UTE sequence as shown in a log-log plot.	87
7.10	Temperature rise during the CV UTE 25ms measurement for the investigation of the sequences thermal behavior. The measurement was stopped at approximately the 30st temperature measurement.	87
7.11	CV UTE sequence at minimum TE and standard protocol otherwise.	88
7.12	CV UTE standard protocol with TE changed to 10ms.	90
7.13	CV UTE at 128x128 matrix size and 60 000 radial views. Otherwise the standard protocol was used.	92
7.14	Base size of 512x512 with 60 000 radial views in the CV UTE sequence during parameter variation.	93
7.15	Comparison of different radial view settings.	94
7.16	Filters for the CV UTE sequence, added to the standard protocol.	95
7.17	CV UTE standard protocol with asymmetric echo set to off.	98

7.18	Zero point artefact in the CV UTE sequence.	101
7.19	Ringling artefact in the CV UTE sequence.	101
7.20	CV UTE over night, high resolution measurement at minimum TE.	102
7.21	CV UTE high resolution measurement with a TE of 0.8ms.	103
7.22	CV UTE slice thickness analysis data.	103
8.1	DA-3DPR sequence diagram. Image source: Nagel, A. et al[13]	106
8.2	Screenshot of the custom software for reconstruction of data acquired with the DA-3DPR sequence.	107
8.3	DA-3DPR with comp set to postcomp in reconstruction.	108
8.4	Standard protocol for the DA-3DPR sequence. Using a 256 reconstruction matrix.	109
8.5	Regions of interest used for the SNR analysis in the DA-3DPR sequence.	110
8.6	Difference image of two successive slices used for SNR calculation.	110
8.7	Modulation transfer function obtained from the ESF using numerical derivatives of the LSF for the DA-3DPR sequence. Showing a density histogram of 180 MTFs from 8 slices with bin widths of $0.08\frac{1}{mm}$ in x direction and $0.1\frac{1}{mm}$ in y direction.	111
8.8	Line spread function obtained by integrating the PSF in y direction for the DA-3DPR sequence. Also showing one of the Gaussian fits used for the resolution analysis.	112
8.9	Line profiles of all lines used for the edge overshoot analysis in the DA-3DPR sequence. Normalized by dividing each line by the mean inside the edges.	113
8.10	Thermal behavior of the DA-3DPR sequence as shown in a log-log plot.	114
8.11	Different reconstruction matrix sizes in DA-3DPR.	115
8.12	Comparison of different projection settings.	116
8.13	Comparison of different pulse duration settings.	117
8.14	Comparison of different pulse duration settings.	118
8.15	Improved standard protocol for the DA-3DPR sequence.	119
8.16	Regions of interest used for the SNR analysis in the DA-3DPR sequence improved standard protocol.	120
8.17	Difference image of two successive slices used for SNR calculation.	121
8.18	Modulation transfer function obtained from the ESF using numerical derivatives of the LSF for the DA-3DPR improved standard protocol. Showing a density histogram of 480 MTFs from 15 slices with bin widths of $0.08\frac{1}{mm}$ in x direction and $0.05\frac{1}{mm}$ in y direction.	121
8.19	Line spread function obtained by integrating the PSF in x direction for the DA-3DPR improved standard protocol. Also showing one of the Gaussian fits used for the resolution analysis.	122
8.20	Line profiles of all lines used for the edge overshoot analysis in the DA-3DPR improved standard protocol. Normalized by dividing each line by the mean inside the edges.	123
9.1	Bruker 15.2T UTE comparison measurement.	127
9.2	Regions of interest used for the SNR analysis in the Bruker UTE3D measurement.	127
9.3	Difference image of two successive slices used for SNR calculation of the Bruker UTE3D measurement.	128

9.4	Modulation transfer function obtained from the ESF using numerical derivatives of the LSF for the Bruker UTE3D sequence. Showing a smooth density histogram of 484 MTFs. Please note that this plot is only provided to illustrate the shape of the MTF and was not used for the analysis of the resolution.	129
9.5	Point spread function analysis using Gaussian fits in Bruker UTE. Data points shown are without spline baseline subtraction but with constant baseline adjustment performed by subtracting the average of the data points left of the peak.	129
9.6	Line profiles of all lines used for the edge overshoot analysis in the Bruker UTE3D measurement. Normalized by dividing each line by the mean inside the edges. .	130
9.7	Edge spread function for the comparison measurement using the UTE sequence on the Bruker 15.2T system.	131
9.8	Line profile from a slice in the comparison measurement, figure 9.1, UTE on Bruker 15.2T.	132
9.9	Bruker ZTE sequence diagram. Image source: Bruker, Paravision 6.0 manual[14]	132
9.10	Bruker 15.2T zero TE measurement.	133
9.11	Regions of interest used for the SNR analysis in the Bruker ZTE measurement. .	134
9.12	Difference image of two successive slices used for SNR calculation.	134
9.13	Modulation transfer function obtained from the ESF using numerical derivatives of the LSF for the Bruker ZTE sequence. Showing a smooth density histogram of 484 MTFs.	135
9.14	Point spread function analysis using Gaussian fits in Bruker ZTE. Data points shown are without spline baseline subtraction but with constant baseline adjustment performed by subtracting the average of the data points left of the peak.	136
9.15	Line profiles of all lines used for the edge overshoot analysis in the Bruker ZTE measurement. Normalized by dividing each line by the mean inside the edges. .	136
9.16	Edge artefact in which the edge has a lower signal around its corner in the Bruker ZTE sequence.	138
9.17	Line profile from a circular part of the slice in the Bruker 15.2T ZTE sequence, taken from figure 9.10.	138
10.1	Standard protocols for the XD VTE, CV UTE and DA-3DPR sequences and images acquired using these standard protocols. Images acquired for the comparison with the 15.2T pre clinical imaging system using the Bruker UTE3D and Bruker ZTE sequences and the parameters used in those sequences.	140
10.2	Resolution results for the different standard protocols in this thesis. The color of the bars refers to the reliability of each measurement as provided in table 10.1. ESF is the ESF-MTF method. PSF Y is the Gaussian fits on the LSF in y direction from PSF integration in x direction method. Please note that two graphs have errors so small that the error bars are not visible. Pixel sizes for the XD VTE, CV UTE, Bruker UTE3D and Bruker ZTE are $125\mu m$, the DA-3DPR standard protocol has a pixel size of $244.9\mu m$ and the DA-3DPR improved protocol pixel size is $168\mu m$	142
10.3	Signal to noise ratio results. Two different methods, ROI and Diff are shown. These are the region of interest method and the difference images method. For all values marked with a “*” the difference image has been obtained using consecutive slices instead of different measurements.	143

10.4	Edge enhancement and ringing results. 100% means that there is no overshoot and this would be the ideal situation. The artefact described in the XD VTE sequence is best understood as ringing, or a mixture of ringing and edge enhancement. The other overshoots along the edge are due to edge enhancement.	145
------	--	-----

List of Tables

5.1	Standard sequence target parameters condensed overview.	47
5.2	Overview of the evaluation parameters in quality control, also found in parameter variation result tables.	48
6.1	XD VTE standard protocol.	50
6.2	Measurement results for the XD VTE standard protocol.	58
6.3	Echo time parameter variation, XD VTE sequence. Pixel size: $125\mu m$	59
6.4	Averages parameter variation, XD VTE sequence.	60
6.5	Matrix sizes parameter variation, XD VTE sequence.	60
6.6	Bandwidth parameter variation, XD VTE sequence.	63
6.7	Parameter variation for the Resolution/Filters in the XD VTE sequence.	65
6.8	Parameter variation of other settings in the XD VTE sequence.	68
6.9	Results for the XD VTE overnight high resolution measurement and comparison to the standard protocol.	76
7.1	CV UTE standard protocol.	80
7.2	Measurement results for the CV UTE standard protocol.	85
7.3	CV UTE at minimum TE of 0.07ms, otherwise using the standard protocol.	88
7.4	Echo time parameter variation for the CV UTE sequence.	89
7.5	Averages parameter variation, CV UTE sequence.	91
7.6	Matrix size variation, CV UTE sequence.	91
7.7	Radial views parameter variation with 256x256 matrices, CV UTE sequence.	93
7.8	Bandwidth parameter variation, CV UTE sequence.	94
7.9	Parameter variation for the filters in the CV UTE sequence.	97
7.10	Parameter variation of the other settings of the CV UTE sequence.	99
8.1	DA-3DPR standard protocol.	109
8.2	Measurement results for the DA-3DPR standard protocol.	113
8.3	DA-3DPR parameter variation with regard to projections.	115
8.4	Parameter variation of the pulse duration.	117
8.5	Parameter variation of the T_0 pulse sequence timing setting.	118
8.6	DA-3DPR improved standard protocol.	120
8.7	Measurement results for the DA-3DPR improved standard protocol.	123
9.1	Parameters for the Bruker 15.2T comparison measurement.	126
9.2	Measurement results for comparison protocol of the Bruker 15.2T UTE sequence.	131
9.3	Parameters for the Bruker 15.2T comparison measurement.	133
9.4	Measurement results for comparison protocol of the Bruker ZTE sequence.	137
10.1	Overview of the grading system for result reliability.	139

Abbreviations

UTE	Ultrashort TE
VTE	Variable TE
ZTE	Zero TE
MRI	Magnetic R esonance I maging
NMR	Nuclear Magnetic R esonance
NMV	Net Magnetization V ector
RF	Radio F requency
FOV	Field O f V iew
ROI	Region O f I nterest
TR	Repetition time
TE	Echo time
TA	Acquisition time
Avg	Averages
Seq	Sequence
Proj	Projections
BW	Band W idth
SNR	Signal to Noise R atio
ESF	Edge Spread F unction
LSF	Line Spread F unction
PSF	Point Spread F unction
MTF	Modulation T ransfer F unction
OBJ	O bject

IMG	I mage
IR	I nversion R ecovery
FWHM	F ull W idth H alf M aximum

Symbols

B_0	Magnetic flux density vector, static field	T
B_1	Magnetic flux density vector, rf field	T
M	Net magnetization vector	T
M_z	Net magnetization vector z direction	T
M_{xy}	Net magnetization vector in xy plane	T
\bar{x}	Mean	
Δx	Standard error of the mean	
n	Sample size	
μ_d	Mean signal of image data	
σ_b	Standard deviation of background	
σ_{SNR}	Standard deviation, SNR	
Sl_i	Matrix of the i-th slice	
ΔSNR	Standard error, SNR	
SNR_{corr}	SNR corrected	
$\Delta \text{SNR}_{\text{corr}}$	Standard error of corrected SNR	
SNR_{diff}	SNR using difference images	
$\delta(x)$	Dirac delta function	
\mathcal{F}	Fourier transform	
r	Resolution	μm
I	Intensity	
I_{mean}	Mean intensity	
x_{start}	Start position in x direction	mm

x_{end}	End position in x direction	mm
$d_{\text{line},i}$	Length of the i-th line profile	mm
d_{θ}	Diameter at angle θ	mm
σ_d	Standard deviation of diameter	mm
$\sigma_{d,\text{rel}}$	Relative standard dev. of diameter	mm
h	Slice thickness	mm
s	Length of slice profile	mm
Δr	Pixel shift	pixels
$\Delta\chi$	Magnetic susceptibility difference	
c_{shape}	Object shape constant	
G	Gradient strength	$\frac{T}{m}$
$\nu_{1/2}$	FWHM of the line spectrum	Hz
$\Delta\nu_{1/2}$	Standard error of $\nu_{1/2}$	Hz
ω_L	Larmor frequency	Hz
γ_n	Gyromagnetic ratio	$\frac{\text{rad}}{sT}$
α	Flip angle	$^{\circ}$
σ	Standard deviation	
γ	Angle of slice thickness phantom plate	$^{\circ}$

Introduction

1.1 Introduction to Magnetic Resonance Imaging

Magnetic resonance imaging has become one of the most important medical imaging methods. It is used in a wide area of diagnostic applications.

Nuclear magnetic resonance is the mechanism which forms the basis of MRI investigations. It is based on the fundamentally quantum mechanical phenomena of nuclear spin.

Some nuclei, depending on their proton and neutron composition, exhibit a non zero nuclear spin and therefore a magnetic moment.

Nuclear spin vectors are aligned randomly when no external field is present, figure 1.1a.

In the case of NMR these nuclei are placed in an external magnetic field, which we will assume to be totally homogeneous. We will refer to the magnetic flux density of this field as B_0 , this vector describes the orientation of the magnetic field.

Having applied the external magnetic field B_0 we can use this field to define a spatial direction. We will use this as the mathematical basis for our state vector. This basis has the basis vectors of nuclear spins aligned parallel to the external magnetic field $|\uparrow\rangle$ and anti parallel to the external magnetic field $|\downarrow\rangle$. Please note that this choice of basis vectors is useful but we could choose any other complete basis without changing the underlying physics.

The state vector $|\Psi\rangle$, with complex numbered coefficients c_\uparrow and c_\downarrow , of an individual spin is given by equation 1.1.[5]

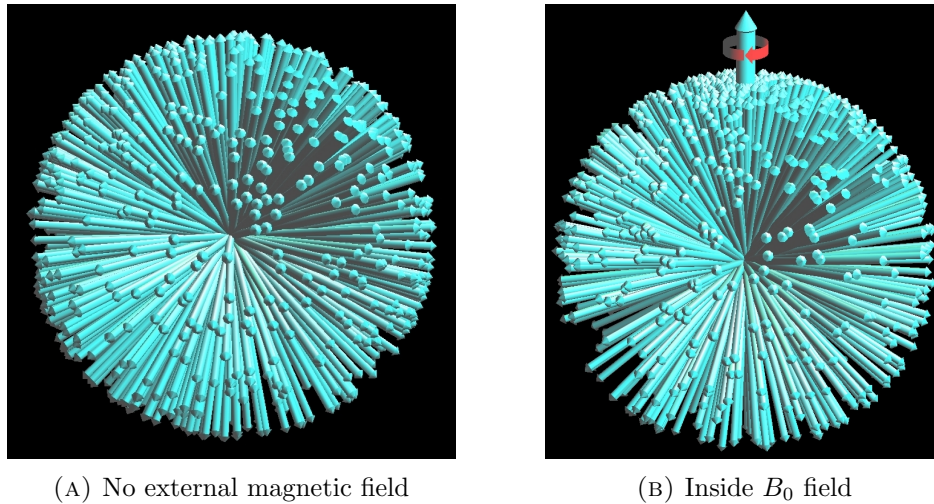


FIGURE 1.1: Nuclear spin ensemble with no external magnetic field (left) and external field applied (right). When the nuclei ensemble is placed inside the external magnetic field they precess with the Larmor frequency and the spatial distribution is shifted towards the external field B_0 and a net magnetization M in z direction can be observed.

Image source: Hanson, L.[5], reprinted with his permission.

$$|\Psi\rangle = c_{\uparrow}|\uparrow\rangle + c_{\downarrow}|\downarrow\rangle \quad (1.1)$$

As has been explained by Feynman and Hanson, the nuclear spins are not all aligned either parallel or anti parallel to the external field after placing them inside this external field, but there is a shift in probability toward alignment with the external magnetic field. This situation is illustrated in figure 1.1b. A complete parallel or anti parallel alignment would only be found after the wave function of each individual spin has been collapsed into an eigenstate by performing a measurement on each individual nuclear spin without disturbing the other spins. [5, 15]

It is important to note at this point that in NMR measurements it is always ensembles of nuclei which contribute in the measurement and these measurements are not measurements of individual nuclear spins. This gives rise to many classical analogies used for explanation which conform to the quantum mechanical descriptions.[5]

A MR measurement just introduces a perturbation to this spin ensemble and is not in itself sufficient to collapse the individual wave functions into their eigenstates. For a detailed calculation of this please refer to Hanson “Is quantum mechanics necessary for understanding magnetic resonance?”.[5]

As soon as these nuclei are placed inside the B_0 field they also start to precess at a distinct frequency ω_L which is dependant on the magnetic field strength B_0 and the gyromagnetic ratio γ_n . This precession frequency is called the Larmor frequency. It is given by equation 1.2.

$$\omega_L = \gamma_n B_0 \quad (1.2)$$

The shift in probability of alignment towards the external magnetic field leads to a net magnetization which can be described by the net magnetization vector M .

So far this experimental set up allows no measurements. To acquire a signal we will rotate the net magnetization vector M away from its equilibrium position using a second magnetic field B_1 perpendicular to the static magnetic field B_0 . A static second field which is weaker than the B_0 field would not cause much rotation. This is different when the second field B_1 is alternating. A coil is used to produce a magnetic field based on an alternating current. When this second field has the right frequency to always push the NMV in just the right moment a classical resonance phenomenon occurs and even a relatively weak magnetic field can rotate the NMV around any angle. The frequency for this resonance is also the Larmor frequency. This second magnetic field is referred to as a rf-pulse.

For the further explanation a simplification of our viewpoint will be introduced. In our current frame of reference, the laboratory frame, the nuclear spin vectors precess with the Larmor frequency around the external magnetic field B_0 . We will move from this frame of reference into a rotating frame of reference in which the net magnetization vector (NMV) M only changes when a second magnetic field B_1 is applied or the NMV is still returning back to its equilibrium position after such an application.

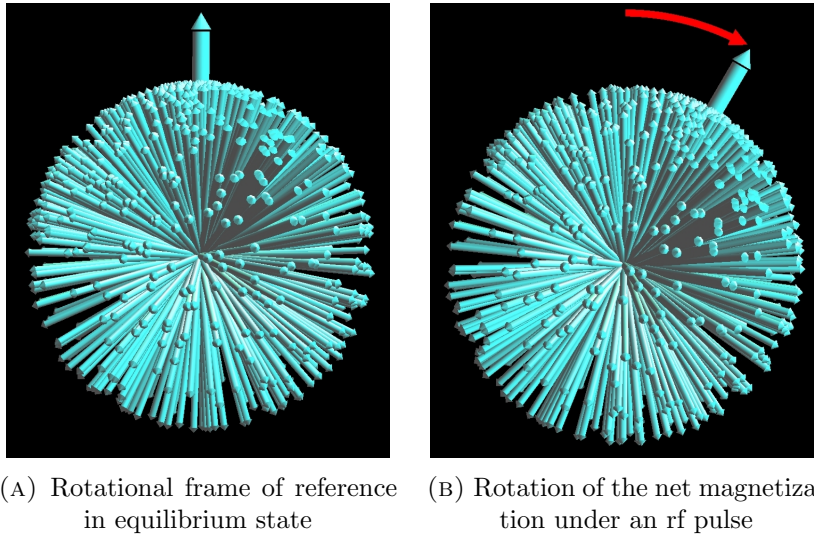


FIGURE 1.2: Explanation of the rotational frame of reference and application of this view to the response of the system to an incoming rf pulse.

Image source: Hanson, L.[5], reprinted with his permission.

The rotating NMV induces a signal in a coil also placed perpendicular to the B_0 field.[16] This can be either the same coil used to generate the RF pulse or a second receive coil.

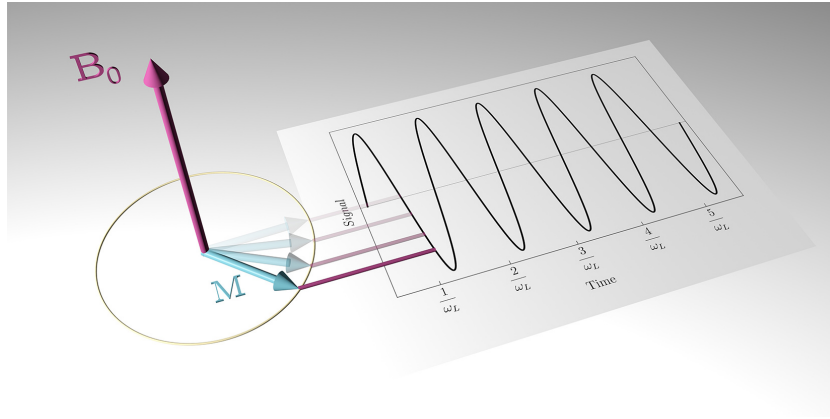


FIGURE 1.3: Signal induced from the rotating net magnetization which was rotated by 90° into the x-y plane.

Such a signal has a carrier frequency of the Larmor frequency.

The signal produced after excitation of the nuclei ensemble is called a free induction decay. Such a signal is shown in figure 1.4. It has a frequency of the Larmor frequency. Additionally this signal is attenuated over time because the net magnetization vector returns back to its equilibrium state as will be described in more detail in section 1.1.1.

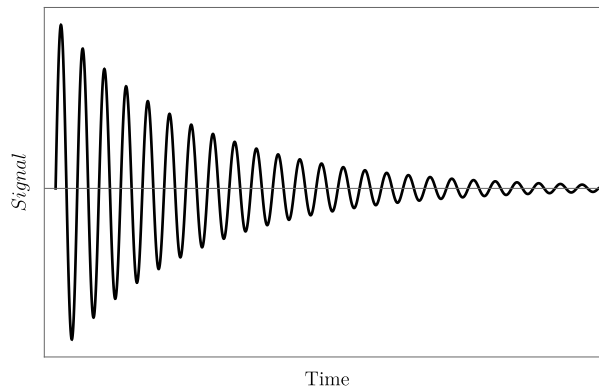


FIGURE 1.4: Free induction decay. The signal observed in MR in the transverse direction after excitation. As measured in the laboratory frame of reference.

1.1.1 Relaxation

Two different relaxation processes play an important role in NMR measurements, and therefore MR image creation. These will be explained in more detail in this section.

1.1.1.1 T1 Relaxation

We will look at the magnetization in the direction of the external static magnetic field B_0 , this component of the NMV M will be called M_z .

After excitation the longitudinal magnetization returns back to its original equilibrium position. This process is inelastic and caused by interactions between the moving nuclei. T1 relaxation is therefore also called spin-lattice relaxation. It is described by equation 1.3.

$$M_z(t) = M_z(\infty) \left(1 - e^{-\frac{t}{T_1}}\right) \quad (1.3)$$

The magnetization in M_z direction will return back to its equilibrium value $M_z(\infty)$ asymptotically. The relaxation constant of this process is called T1. As we can see when $t = T_1$, equation 1.3 becomes equation 1.4.

$$M_z(T_1) = M_z(\infty) \left(1 - e^{-\frac{T_1}{T_1}}\right) = M_z(\infty) (1 - e^{-1}) = M_z(\infty) \left(1 - \frac{1}{e}\right) \approx 0.63 M_z(\infty) \quad (1.4)$$

After a time of the length of T1 after excitation has passed the magnetization in z direction M_z has returned back to about 63% of its original value.

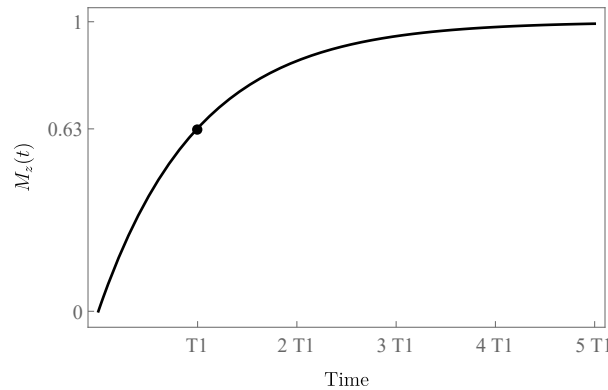


FIGURE 1.5: T1 relaxation time evolution. Equilibrium value of the magnetization is set to 1.

This relaxation process is also shown in figure 1.5.

T1 generally becomes shortest when the random interactions between the nuclei fulfill the resonance condition, which is the case in matter of medium firmness. Neither very firm solids nor fluids exhibit the shortest T1 times.[17]

1.1.1.2 T2 Relaxation

Additionally to the inelastic interactions between nuclei and the lattice there is another relaxation process which is very important in NMR. This process is called spin-spin relaxation and is observed in transversal direction. We will therefore describe it by the net magnetization vector in the x-y or transversal plane M_{xy} , this vector is perpendicular to B_0 .

The process is described in equation 1.5 and shown in figure 1.6.

$$M_{xy}(t) = M_{xy}(0)e^{\frac{-t}{T_2}} \quad (1.5)$$

As with T1 relaxation we can investigate the case where $t = T_2$, equation 1.6. As T_2 is the relaxation constant of this relaxation process the transversal magnetization has decayed to about 37% after a time span of T_2 after the excitation has stopped.

$$M_{xy}(T_2) = M_{xy}(0)e^{\frac{-T_2}{T_2}} = M_{xy}(0)e^{-1} = M_{xy}(0)\frac{1}{e} \approx 0.37M_{xy}(0) \quad (1.6)$$

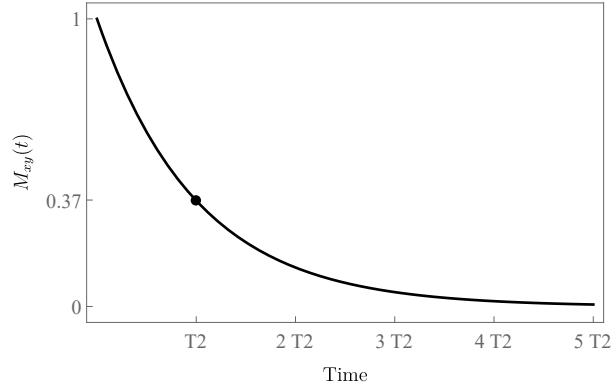


FIGURE 1.6: T2 relaxation time evolution.

T_2 relaxation is caused by both the inelastic processes which cause T_1 as well as additional elastic processes.[17] Therefore the relationship $T_1 \leq T_2$ generally holds true.

Each nucleus is exposed to a magnetic field which is slightly different from the static B_0 field due to local fluctuations in the magnetic field.[18] This causes a slight change or detuning in the Larmor frequency of the different nuclei. This causes them to rotate at slightly different speeds and they therefore begin to dephase.

The length of T_2 depends mainly on the structure in which the nuclei is embedded with fluids having long T_2 times and solids having very short T_2 times.

1.1.1.3 T2* Relaxation

In addition to the T2 relaxation mechanism inhomogeneities in the outside magnetic field and in the sample also lead to changes in the magnetic field experienced by the nuclei.[19]

This additional dephasing is described using the relaxation constant T2'. T2* is the relaxation constant of both the T2' and T2 processes combined, equation 1.7.

$$\frac{1}{T2^*} = \frac{1}{T2'} + \frac{1}{T2} \quad (1.7)$$

The T2* time is therefore equal to or smaller than the T2 time. Whether T2 or T2* is measured in NMR experiment depends on the sequence used. The VTE, UTE and ZTE sequences discussed in this thesis all measure T2* and not T2.

1.1.2 Sequences

Sequences are MR measurements procedures which define the physical contrast which is obtained from the resulting data. They are usually implemented in specialized software packages which are specific to a scanner type and manufacturer.

A simple pulse sequence would for example be the FID sequence as described above, recapped and formulated as an algorithm.

1. RF pulse which flips the NMV M by 90° into the xy plane.
2. Turn on the analog digital converter and record the FID signal.

1.1.3 Image Generation

Gradients are a key concept to understanding image creation in MR imaging. Gradients are additional magnetic fields, produced by electromagnets so called gradient coils, which can be controlled in software and cause a dependency of the field strength on the location in space.

Applying a gradient to the sample causes the Larmor frequencies to change inside the sample depending on the location in relation to the gradient. This situation is illustrated in figure 1.7.

In standard 2DFT sequences the first spatial direction is encoded using the gradients for slice selection.



FIGURE 1.7: Change in Larmor frequency when a gradient is applied to the sample.

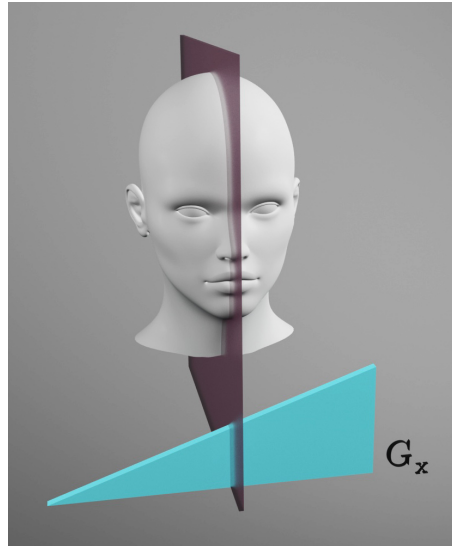


FIGURE 1.8: Slice selection based on the change in Larmor frequency caused by a gradient applied along the x direction.

Slice selection works by turning on the Gradient in the direction in which the slices are to be imaged, which in turn causes a change in the local Larmor frequency.

As discussed before the Larmor frequency is also the resonance frequency for the RF pulse interaction which flips the NMV M from its equilibrium position. Now that the gradient is turned on only the part of the sample which has the Larmor frequencies contained in the pulse will be in resonance and therefore flip. These slice selection gradients have to be turned on for every rf pulse which is contained in the sequence.

The process of slice selection is also illustrated in figure 1.8.

An MR image is always divided into single pixels, which are just the dots which make up the image. But we also have to consider the third spatial direction, the slice thickness. The resulting volume is called a voxel, which is a single signal unit in our MR measurement.

Now two spatial directions remain to be encoded. We will first look at a one dimensional example. This is a single line of voxels. Please note that the arrows shown in these graphics always represent the net magnetization of the spin ensemble inside the voxel and not single spins.

When we apply a gradient to this line the nuclei in each voxel will start to rotate with different Larmor frequencies, due to the different magnetic field that they experience. This situation is shown in figure 1.9.

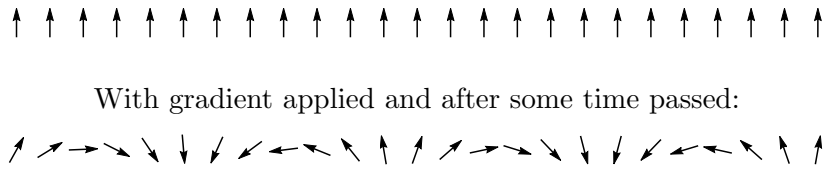


FIGURE 1.9: Single line of voxels before and after gradient application.

We can now see that in this case all the magnetization vectors cancel each other out, we will get no signal in total.[17]

Lets look at a different situation where not all the voxels are equal, but there is some kind of pattern in our sample, figure 1.10.



FIGURE 1.10: Single line of voxels with a pattern. No gradient field applied.

Once again a gradient can be applied to this sample, the magnetization vectors will start to rotate at different frequencies again, figure 1.11.

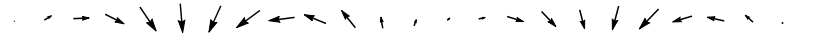


FIGURE 1.11: Single line of voxels with a pattern in a gradient field after some time has passed.

We notice that for the same situation which is depicted in figure 1.9 now a net signal will emerge.

This process of pattern matching can be repeated for different times after which the voxels have rotated while the gradient field is applied. Each of these will describe a different pattern, and each will return a signal intensity which represents how strongly this pattern is represented in the sample.

After repeating this process often enough we can add up all the patterns (figure 1.12a), multiplied by their signals and obtain an image of the sample, shown in figure 1.12b.

This is the process of obtaining the Fourier transformation of the frequency data which represent a spatial frequency inside the sample. This process can be performed directly from a single time signal for one spatial dimension. As we can see if we let the spins rotate while recording the signal produced this signal will have different frequencies which can than be reconstructed into an image using a Fourier transform.

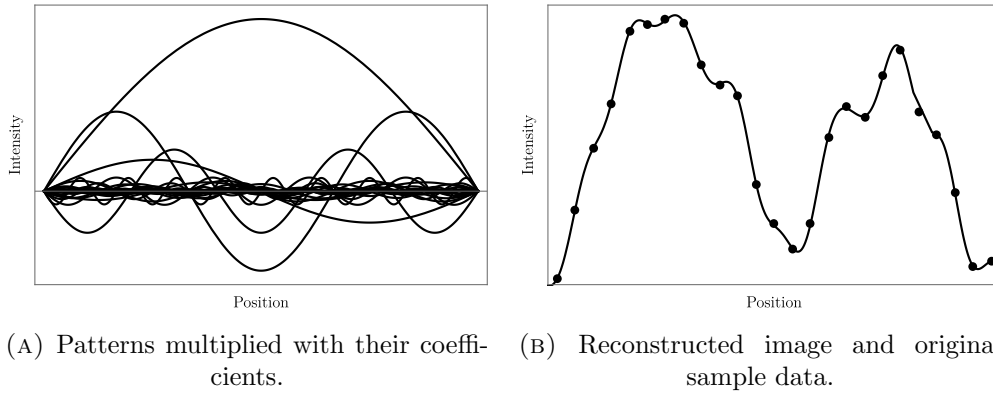


FIGURE 1.12: Example of the reconstruction of an image based on patterns/spatial frequencies using the Fourier transform.

Spatial frequency space is called k-space. The above example provides a path through a one dimensional k-space. Each point in k-space represents a single spatial frequency, where 0 is a uniform object and the highest frequency represents the highest detail.[20]

The same principle can be extended to more dimensions. In sequences with slice selection, as described above, this k-space sampling happens in two dimensions, an example for a 2d pattern of spins is shown in figure 1.13.

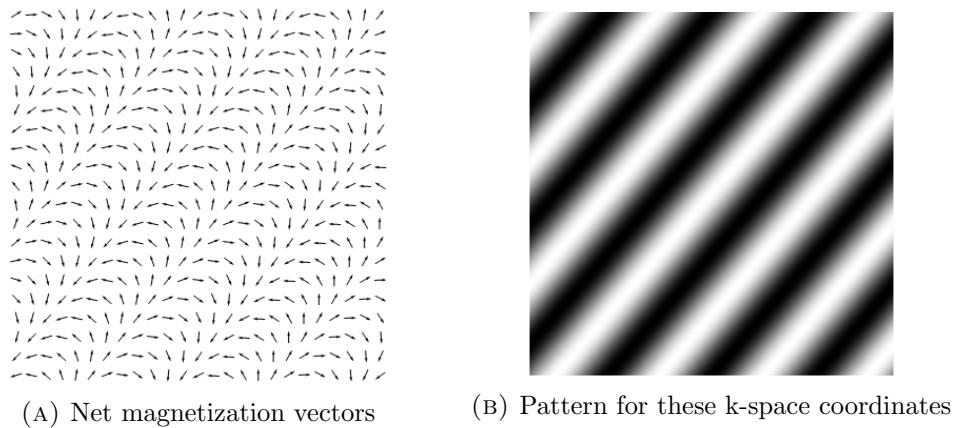


FIGURE 1.13: 2 dimensional pattern of spins in two gradients after some time.

Each different pattern represents one point in k-space, with the most uniform patterns close to the center of k-space and the highly structured patterns towards the edges of k-space.

Once again all of these patterns are combined, scaled with their respective coefficients, in order to obtain the final image. This is realized by obtaining the 2D Fourier transform of the k-space data obtained.

One possible trajectory in k-space, which is used extensively in clinical sequences, is called 2DFT. This can be a bit misleading because basically all reconstructions are based on 2D Fourier transforms. 2DFT k-space sampling is based upon sampling one line of k-space in the

first direction at a time, called the frequency encoding direction. The measurement is repeated for each line in the second direction in k-space, the phase encoding direction.

But many different trajectories can be taken through k-space in order to obtain the necessary data for reconstructing an image.[20]

Sequences with slice selection and a 2 dimensional trajectory through k-space are called 2D sequences, those with a 3 dimensional trajectory in k-space are referred to as 3D sequences.

1.1.4 Gradient Echo Sequence

Gradient echo sequences are based on using the gradient system to create a second signal, called an echo.

This works by first applying a gradient which dephases the spins. Inversion of this gradient is the next step. When the gradient is reversed the spins start to rephase again and ultimately produce a second signal as they are in phase again and dephase again.

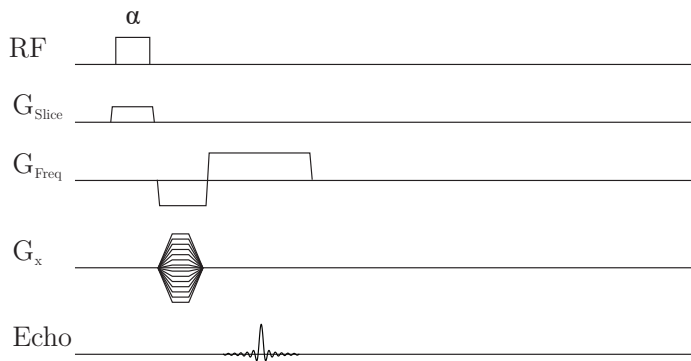


FIGURE 1.14: Sequence diagram for a gradient echo sequence.[6] Echo shape based on:[7]. The lines inside the gradients indicate that the measurement is repeated for each combination of different gradient strengths. The whole measurement is repeated for each of these gradient settings.

These gradient echo sequences usually don't employ 90° pulses but smaller flip angles α , this allows shorter repetition times.

1.2 Ultrashort TE Imaging

Although many different sequences are available for clinical applications, these sequences are mainly focused on measurements of tissues with long $T2^*$ times.[1]

Some parts of the human body like tendons, cortical bone, menisci, teeth and many more are mostly made up of components with short $T2^*$ times. This is also true for composite materials used in medicine and beyond.

Ultrashort TE (UTE) sequences have echo times about 10 to 20 times shorter than what is available on current clinical whole body mr scanners.[1]

These sequences face a special set of challenges. Usually the relaxation of the magnetization back to its equilibrium state during excitation can be ignored. This is not the case when these $T2^*$ times become ultra short. Therefore half echos are usually used for detection in UTE sequences.[1]

To enable ultra short echo times a special method of k-space sampling has to be employed. One possible k-space trajectory is radial sampling. In this sampling method slice selection is applied and the center of k-space is sampled first, with spokes reaching outwards.

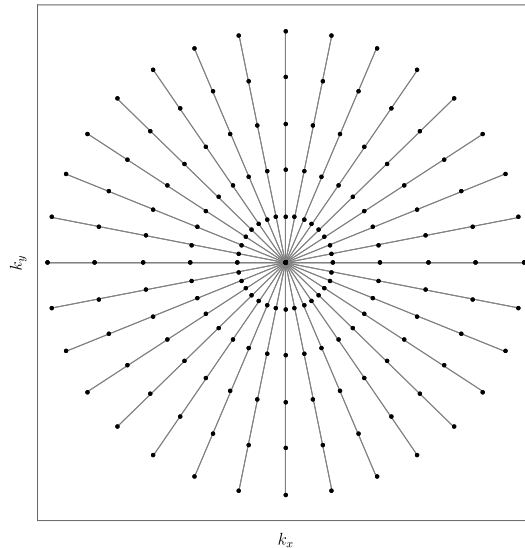


FIGURE 1.15: Radial k-space sampling at multiple points along each spoke. This image is based on the image of radial sampling by Robson M.[1].

One example of radial k-space trajectories is shown in figure 1.15. These radial k-space samples are then regridded onto a 2d matrix and Fourier transformation is used to obtain an image from the k-space data.

This radial k-space sampling is implemented by ramping up the gradients directly after each measurement, acquiring k-space points further from the center of k space with stronger gradients. An example for a UTE sequence is depicted in figure 1.16.

The usual rephasing after slice selective excitation is also skipped by obtaining the same data twice with the slice selection gradient in different directions and adding this information back up.[1]

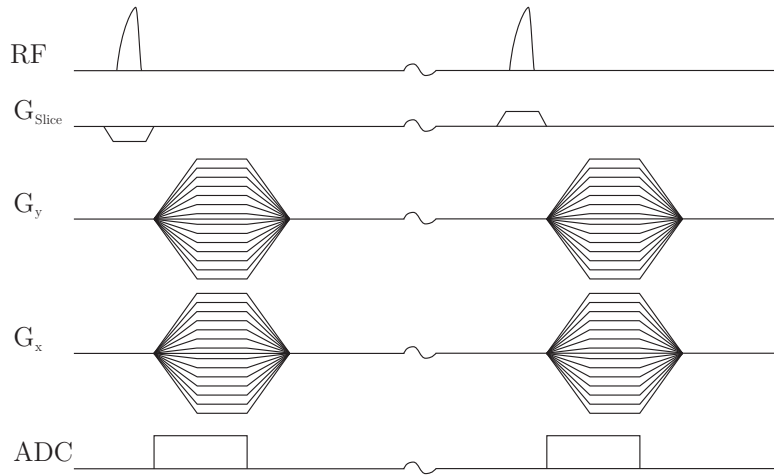


FIGURE 1.16: Sequence diagram for a UTE sequence as published by Robson M.[1] and Tyler D.[8]. This illustration is based on their sequence illustrations. A half rf excitation pulse is shown. The lines inside the gradients indicate that the measurement is repeated for each combination of different gradient strengths. The whole measurement is repeated for each gradient setting with the slice selection gradient pointing in the opposite direction.

All these measures allow the sequence to be run with ultra short TE settings. It should be noted that the word echo time is used even though the signal received is not a gradient echo.

Methods

2.1 Image Reconstruction from DICOM

All images printed are shown in full dynamic range if not otherwise denoted.

Images obtained using the Siemens 7T scanner for the CV UTE and XD VTE sequences were exported as DICOM data and these were used for the further analysis.

Each DICOM file contains a single slice. These DICOM images were imported using Mathematicas[21] `Import` function, using the setting ‘`Data`’, as a matrix with values from 0 to 4096.

DA-3DPR images were reconstructed as described in 8.2, the result of this reconstruction are also DICOM images which were processed in the same way as the CV UTE and XD VTE images.

Images from the Bruker system, chapter 9 IMBA 15.2T, were exported as Bruker 2dseq files. These don't contain any additional metadata and just provide the reconstructed image data as binary data. These were also imported using Mathematicas `Import` function in binary mode. These contain all slices within a single file. Therefore this list was split into the single slices and the result was a list of matrices of the single slices.

All slice images printed in this thesis were also imported using Mathematicas `Import` function and exported as PNG graphics, with full dynamic range and without any upscaling, to provide the closest representation to the original image data.

No additional filters were applied before analyzing the data.

2.2 Error Estimation

If not otherwise described the measurement value has been obtained by calculating the mean \bar{x} from a statistical sample.

The error shown is the standard error of the mean. As given by the standard deviation σ divided by the square root of the sample size n , equation 2.1.

$$\Delta x = \frac{\sigma}{\sqrt{n}} \quad (2.1)$$

In this thesis two significant error digits are used and are printed as $(\bar{x} \pm \Delta x)$.

Rounding up has been performed on the error Δx , normal mathematical rounding was applied to the mean value \bar{x} .

2.3 Signal to Noise Ratio

The signal to noise ratio, SNR, is defined as the ratio of the mean value of the image data μ_d to the standard deviation of the background noise σ_b . [22, 23]

$$\text{SNR} = \frac{\mu_d}{\sigma_b} \quad (2.2)$$

The standard deviation of the SNR is calculated based only on the standard deviation of the image data σ_d . Therefore the standard deviation of the SNR σ_{SNR} is given by equation 2.3.

$$\sigma_{\text{SNR}} = \frac{\sigma_d}{\sigma_b} \quad (2.3)$$

But for most measurements in this thesis multiple slices Sl_i were used to obtain the signal to noise ratio. Where Sl_i is the matrix containing the image data in this slice, and N_{Sl} the number of slices included in the analysis.

In this case the standard error of the SNR was obtained by the usual statistical measure as given in equation 2.4. With the signal to noise ratio in the i -th slice SNR_i and the standard deviation of all these signal to noise ratios σ_{SNR_i} . If not otherwise denoted this quantity is meant when referring to the error of the SNR.

$$\Delta\text{SNR} = \frac{1}{\sqrt{N_{SI}}} \sigma_{\text{SNR}_i} \quad (2.4)$$

2.3.1 Region of Interest Selection

Masks were created in Mathematica[21] and used to extract the image data and background noise pixels from the image matrix. This software package was then also used to calculate the relevant statistical values from the image data and noise data set.

2.3.2 Correction for Fourier Reconstruction

Noise is usually distributed around the zero value. In the case of MRI images this information is lost during the reconstruction of the image by taking the magnitude of the Fourier transform. Due to this, a correction factor of 0.655 has to be introduced.[23, 24] Therefore we define the corrected signal to noise ratio SNR_{corr} as given in equation 2.5.

$$\text{SNR}_{\text{corr}} = 0.655 \text{ SNR} \quad (2.5)$$

And the corrected estimated error for the signal to noise ratio, equation 2.6.

$$\Delta\text{SNR}_{\text{corr}} = 0.655 \Delta\text{SNR} \quad (2.6)$$

2.3.3 NEMA Difference Images Method

A second method for determining the signal to noise ratio can be defined by using a difference image obtained by subtracting two images.[4]

For this two images Im_1 and Im_2 are acquired. A difference image ΔIm is calculated, equation 2.7.[4]

$$\Delta Im = Im_1 - Im_2 \quad (2.7)$$

Inside the signal intense region of image Im_1 a region of interest is defined. Inside this area the mean signal μ_{Im_1} in Im_1 is calculated. The noise is obtained by calculating the standard deviation $\sigma_{\Delta Im}$ inside the region of interest of the difference image ΔIm . The signal to noise

ratio obtained using the difference images method SNR_{diff} is calculated as shown in equation 2.8.

A correction factor of $1/\sqrt{2}$ needs to be applied to the standard deviation in order to obtain the image noise, because the value was obtained from a subtraction operation.[4]

$$\text{SNR}_{\text{diff}} = \frac{\mu_{Im_1}}{\sigma_{\Delta Im} \cdot \frac{1}{\sqrt{2}}} \quad (2.8)$$

In order to obtain better statistics this process is repeated for multiple pairs of images. The error is estimated using the standard error, equation 2.1.

2.4 Resolution

Multiple methods were used to obtain resolution measurements. The primary and most robust method, which is used throughout this thesis, is using the edge spread function.

Using the point spread function for resolution analysis makes the result quite sensitive to noise and choice of the region of interest. [25]

Edge spread function based calculations were more reliable and can be performed for multiple lines along the edge yielding far better statistics.

The resolution limit was generally defined as the inverse of the value in frequency space where the modulation transfer function is equal to 0.5.

$$MTF\left(\frac{1}{r}\right) := 0.5 \quad (2.9)$$

Between these transfer functions there exist certain relationships which are shown in figure 2.1.[25]

2.4.1 Edge Spread Function

The edge spread function describes the characteristic response of the system to an edge input.

For measuring the ESF a part of the full slice containing the ESF device was extracted. This part was then rotated such that the line describing the change from high signal intensity area to low signal intensity area was parallel to the y axis.

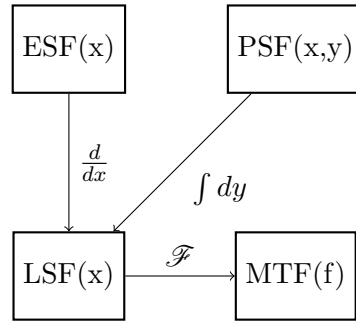


FIGURE 2.1: Relationship between different optical transfer functions

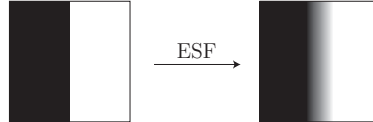


FIGURE 2.2: Illustration of the effect of the edge spread function

From this image a line profile was obtained for every second line. This was done to avoid having any correlations between the data of directly neighbouring lines. An example for the result of this operation is shown in figure 2.3.

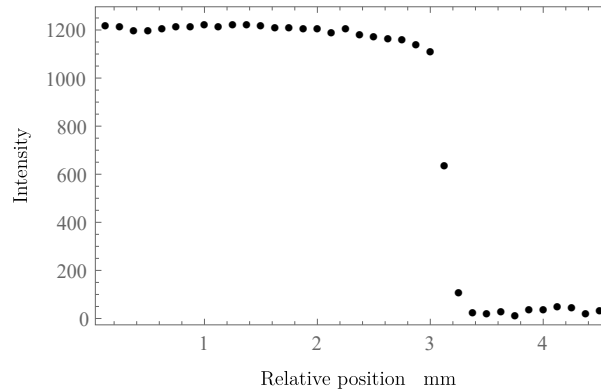


FIGURE 2.3: Line profile of an edge for determining the ESF

These line profiles were then numerically differentiated to obtain the line spread function. Equation 2.10, Figure 2.4.

$$LSF(x) = \frac{d}{dx}ESF(x) \quad (2.10)$$

This line spread function was then zero padded to a length of 65536 in order to obtain a more fine grained Fourier transformed data set which can be directly used to find the position where the resolution criterion, equation 2.9 is satisfied. It is always advisable to choose powers of 2 for the length, as this can vastly improve the performance of the DFFT calculations, depending on the implementation details.

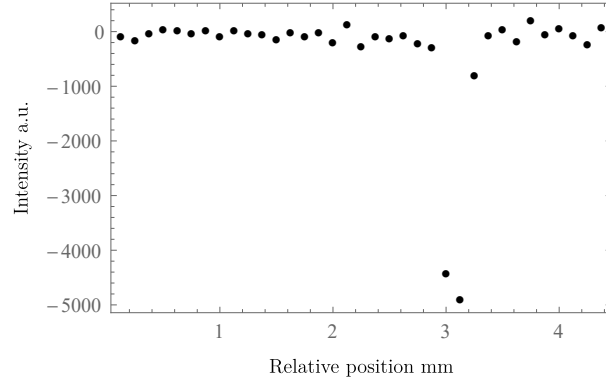


FIGURE 2.4: Line spread function for the ESF in figure 2.3. Scaled to the difference between minimum and maximum of the ESF and divided by the pixel size.

The absolute Fourier transform of this data was obtained. This gives the modulation transfer function of the edge spread function if the Fourier transform of the object can be neglected. Equation 2.11, Figure 2.5.

$$MTF(f) = \frac{\mathcal{F}(LSF(x))}{\mathcal{F}OBJ(x)} \quad (2.11)$$

In the case of a delta function shaped object the Fourier transform of this delta function is 1. Therefore equation 2.12 holds true.

$$\frac{\mathcal{F}(LSF(x))}{\mathcal{F}\delta(x)} = \mathcal{F}(LSF(x)) \quad (2.12)$$

For the ESF a perfect step function can be assumed for this phantom. The derivative of this step function is therefore a delta function and the object shape doesn't have to be considered any further. This assumption might no longer hold true when the phantom is placed at a significant angle to the imaging plane, this placement was therefore performed as precisely as possible and any deviation was corrected by rotating the acquisition area in the sequences which provided this option in the user interface (XD VTE and CV UTE).

Noise still causes a deviation from the actual LSF, but this noise might also be considered as a resolution limiting part of each measurement and be included in the MTF as is the case in this thesis.

The MTF was normalized by dividing the whole function by its first element, equation 2.13.

$$MTF_{norm}(f) = \frac{MTF(f)}{MTF(0)} \quad (2.13)$$

This normalization also makes the scaling of the original ESF and the LSF obtained by obtaining the derivative of this ESF irrelevant. This follows from the linearity of the Fourier transform. Let a be a constant scaling factor present in the spatial domain: $af(x)$, the Fourier transform of this function is therefore $a\mathcal{F}(f(x))(f)$, this factor is divided out by applying the normalization criterion shown in equation 2.13. The result is given in equation 2.14.

$$MTF_{norm}(f) = \frac{a \cdot MTF(f)}{a \cdot MTF(0)} = \frac{MTF(f)}{MTF(0)} \quad (2.14)$$

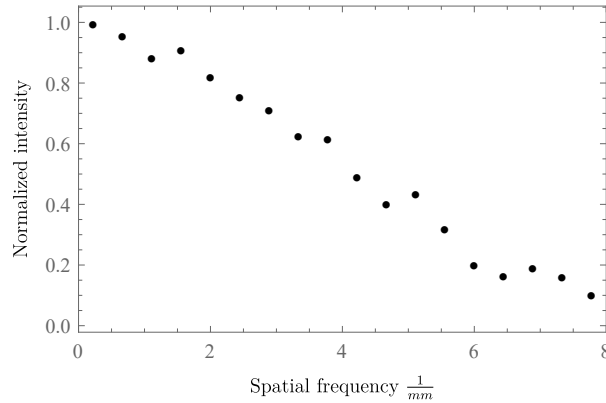


FIGURE 2.5: Modulation transfer function for the LSF in figure 2.4.

An iteration was run over this MTF containing 65536 elements. The spacial frequency of the first element which satisfies the resolution criterion, given in equation 2.9, is used. This is the x-axis position of the first drop to or below 0.5 in the MTF.

This process was repeated for each line profile, therefore the spatial frequency at which the MTF drops to or below 0.5 was obtained for each line profile.

Please note that this method is still susceptible to noise and the MTF obtained is not the pure MTF of the ESF of the sequence but the MTF of the ESF plus noise, depending on how strong the noise is this might lead to an underestimation of the actual resolution.

Analysis has also been performed using piecewise polynomial interpolation functions for interpolating the modulation transfer function. These were prone to convergence problems which lead to questionable results. Therefore zero filling was preferred for this analysis.

From all the line profiles obtained within a single slice, as explained before every second line inside the esf area is used, lines which do not lead to a computable result are dropped from the result set and further analysis. This is usually caused by excessive noise where the modulation transfer function never obtains values below 0.5. This was only necessary for very noise images and was not used regularly.

The mean value of all these spatial frequencies obtained from all the line profiles in this single slice was calculated and used as the resolution result for this slice.

This calculation was repeated over multiple slices. The mean of these intermediate results was obtained and the error was estimated using the standard error estimation for Gaussian sets, equation 2.1.

Please note that this thesis also contains MTF plots, these are only included for illustrative purposes and were not in any way used for obtaining the resolution results. All MTF resolutions obtained were calculated as described above.

It should also be noted that for the ESF all Fourier transforms are referred to as the modulation transfer function. This is usually a reasonable approximation, as explained above, but might not hold true for cases where a lot of noise is visible in the image.

2.4.2 Point Spread Function

The point spread function (PSF) describes the response of an imaging system to a point object input. If the point spread function is linear and isotropic the resulting image can be described as the convolution of the PSF with the object. This relationship is also shown in figure 2.6. [26]

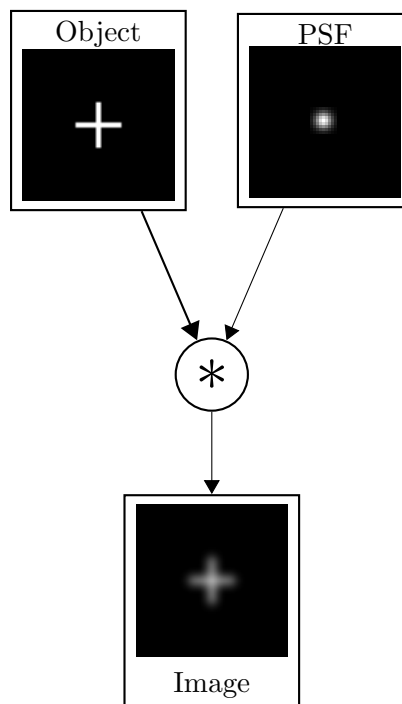


FIGURE 2.6: Effect of the point spread function explained by convolution.

This relationship is also expressed in equation 2.15. Where IMG is the image, PSF the point spread function and OBJ is the object to be imaged.[27]

$$IMG(x) = (OBJ * PSF)(x) = \mathcal{F}(OBJ(x)) \cdot \mathcal{F}(PSF(x)) \quad (2.15)$$

By integrating the point spread function along the x-direction we obtain the line spread function in y-direction.[25, 28] This is also illustrated in figure 2.1.

$$LSF(y) = \int PSF(x, y) dx \quad (2.16)$$

Using the relationship described above, and in equation 2.16, the line spread function was obtained by integrating the point spread function. This line spread function was then analyzed as described in section 2.4.1. Resulting in a resolution measurement based on the line spread function. It should be noted that the LSF is often used as an approximation of the PSF in one spatial direction but they are not necessarily identical.[28] They are equal for special shapes like Gaussian and rectangular functions.[28]

Analysis based on the PSF-LSF-FT method was chosen because of noise constraints and to provide direct comparability to the ESF-LSF-MTF method.

This was repeated for the x direction by rotating the image by 90 degrees and performing the analysis again, integrating in y direction and therefore obtaining the LSF in x direction.

Due to the signal to noise ratios in the UTE sequences and the negative contrast phantom it was mostly impossible to obtain meaningful results from the point spread function. The same is true for angles other than 90 degrees, or multiples thereof, as the interpolation necessary for the rotation disturbed the noise and point image itself sufficiently to make analysis impossible. As explained in section 3.2 UTE sequences often contain artefacts which are caused by k-space trajectory errors. These errors in the trajectory are larger for smaller k-space values.[2] This negative contrast phantom contains a large structure in the lower regions of k-space. The silicone material in the syringe itself. This structure and k-space part would not necessarily be present in a positive contrast phantom and k-space trajectory errors in this k-space region could therefore be avoided.

2.5 Ringing and Edge Overshoot Artefacts

To obtain a quantitative description of ringing phenomena the following method has been established.

A line profile is taken. Within this line profile a mean value for this line profile is calculated from a preset range. This range is printed in appendix A. The set of values used for the calculation of the mean has a size of about 100 elements.

For the same line profile the maximum value is obtained. This maximum value is then divided by the mean value.

The value obtained this way can not necessarily provide a comparison between sequences as a darkening in the center of the signal area can also be observed. But it remains highly useful for comparing performance of different settings and filters within a sequence.

This calculation is repeated for multiple line profiles within the same image. The mean of this single image result set is calculated.

The above process is then repeated again for multiple slices. This way a multiple image result set is obtained. Finally the mean and standard error for this multiple image result set are calculated and are used as the final result.

This has been implemented in Mathematica as described in section 2.8.

2.6 Geometric Accuracy

“The geometric accuracy test assesses the accuracy with which the image represents lengths in the imaged subject. This is also sometimes called the geometric error test. It consists of making length measurements on the images, between readily identified locations in the phantom, and comparing the results with the known values for those lengths.” [29]

Diameter analysis has been performed as follows. For a better understanding of this analysis method the key steps of the algorithm are illustrated in figure 2.7. Each slice has been split into line profiles along the y direction. For each of these line profiles the first position from $x = 0$ where the intensity I reaches a value of $\frac{1}{\sqrt{2}}$ or more of the mean intensity I_{mean} has been determined, let this quantity be x_{start} . In reverse the first position x_{end} where I reaches the value of $\frac{1}{\sqrt{2}}$ has been determined searching from the maximum x position down. Equation 2.17 gives the criterion used.

The mean intensity I_{mean} is calculated by taking the mean of the whole line profile. For images where the phantom has a significant empty area around it, this empty area is cropped away before the analysis. For validation tests have also been performed with calculating the mean only inside part of the line profile or using the maximum value instead of the mean value. When obtaining the mean value only from part of the line profile no significant change in the resulting profile length could be observed.

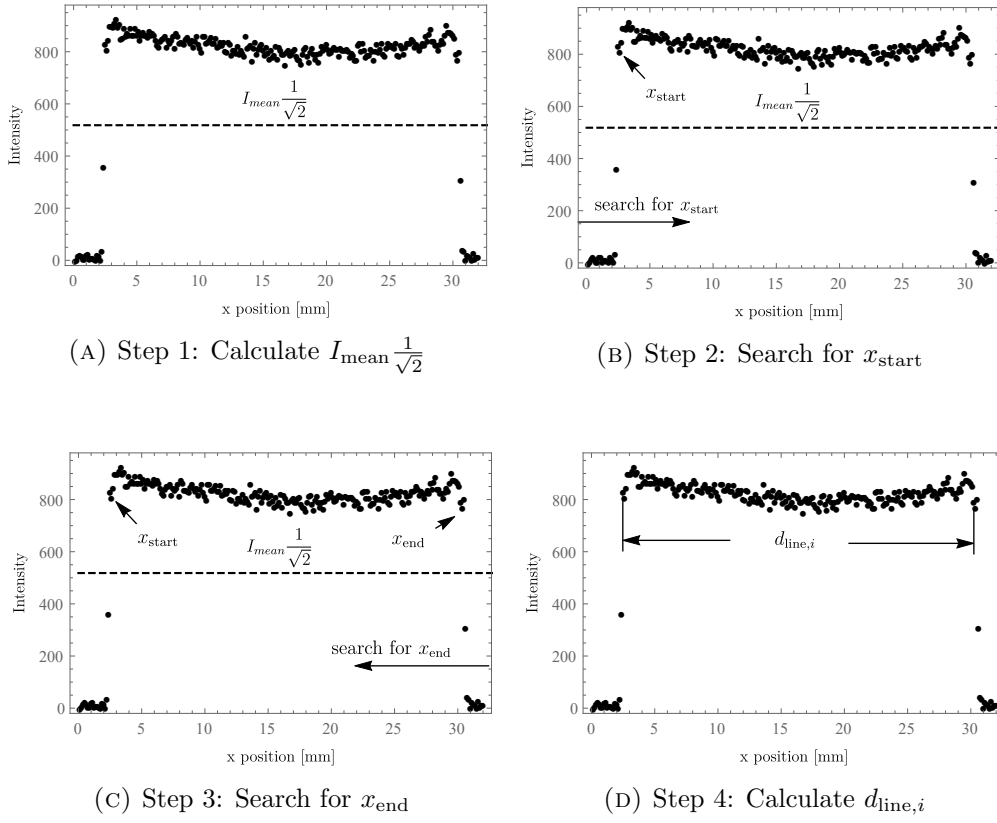


FIGURE 2.7: Algorithm for the analysis of the diameter.

$$I(x_{\text{start}}), I(x_{\text{end}}) \geq \frac{1}{\sqrt{2}} I_{\text{mean}} \quad (2.17)$$

From these values the length $d_{\text{line},i}$ for this line profile is calculated, equation 2.18.

$$d_{\text{line},i} = x_{\text{end}} - x_{\text{start}} \quad (2.18)$$

This process is repeated for each line profile in the slice, from this set the maximum length is chosen and this quantity will be the diameter for this slice d , equation 2.19. The first and last quarter of the line profiles are ignored to avoid outliers, due to parts outside the phantom structure. No systematic errors are introduced by this omission as the maximum radius will be found somewhere around the central line profile as the phantom structure was always placed inside the coil in a symmetrical manner.

The lines which ultimately contain the longest length and therefore diameter information do not have any other structures or artefacts inside them. Only the geometric accuracy quantity could be affected by this implementation. Further investigation of which impact this analysis method has on the geometric error seems unwarranted for these results as the geometric error was small

for all results. Additional validation has been performed by performing length measurements by hand.

$$d_{0^\circ} = \max(d_{\text{line},i}) \quad (2.19)$$

Figure 2.8 shows the result set of the analysis of the line diameters within a single slice.

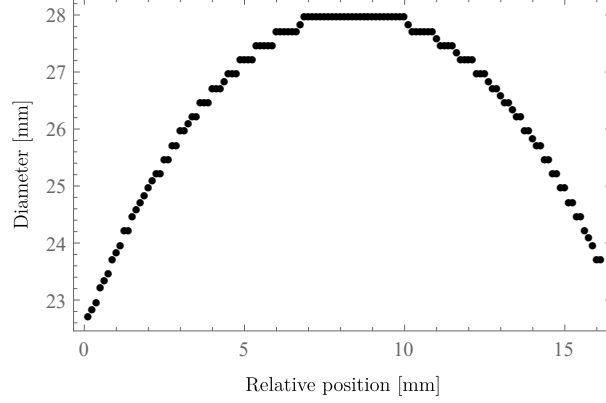


FIGURE 2.8: Line diameters inside a single slice.

Thus far we only determined the diameter in x direction. As any geometric inaccuracies can occur in all other directions this calculation is repeated by rotating the image, using quadratic spline interpolation, cropping the image to the original dimensions and then determining the diameter for that angle d_θ as described above. From this set a mean diameter d for this slice is calculated. Rotations are performed up to 180° in 10° steps.

Geometric distortion will be described by the standard deviation σ_d of the diameters at different angles. Ideally this value should be zero as the phantom structure is a circle and should be rotationally symmetric. To make this quantity more useful, a relative standard deviation $\sigma_{d,\text{rel}}$ is calculated, equation 2.20.

$$\sigma_{d,\text{rel}} = \frac{\sigma_d}{d} \quad (2.20)$$

Final results are obtained by repeating this calculation for multiple slices and taking the mean values and estimating the standard errors for the d and σ_d quantities.

2.7 Slice Thickness

Inside the phantom is a glass plate which is positioned at an angle γ to the transversal measurement plane.

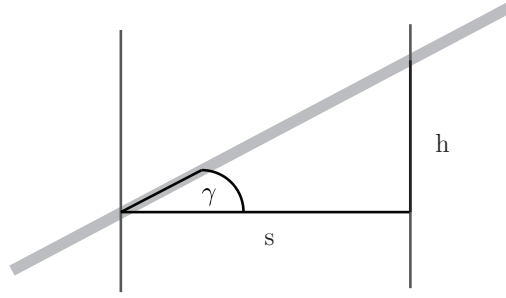


FIGURE 2.9: Geometric considerations for the analysis of slice thickness measurements.

When a transversal image of this plane is acquired part of the plate will create a signal, s , inside this transversal plane. The size of this signal intense area is correlated to the slice thickness h of this image.

Geometric considerations, figure 2.9, lead us to the solution in equation 2.21.

$$h = s \tan \gamma \quad (2.21)$$

The angle for the plate in the phantom used in this thesis is $\gamma = (28.5 \pm 0.2)^\circ$.

This has been implemented by acquiring a transversal slice through the phantom. Inside this image a line profile was placed along the slice thickness phantom and the distance between the points where the signal drops to 50% of the amplitude between the baseline and peak of the slice profile is used as the distance s .

An example line profile used for the slice thickness analysis is shown in figure 2.10.

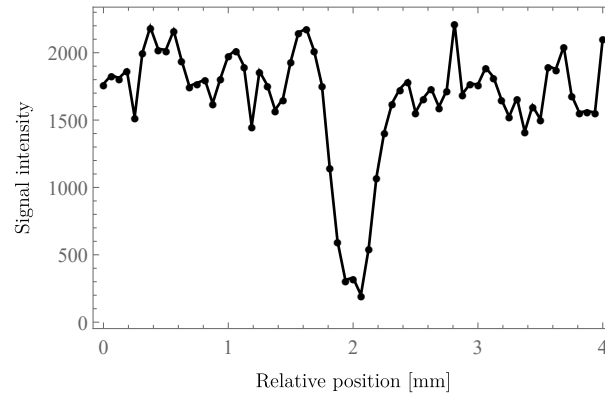


FIGURE 2.10: Line profile for the calculation of the slice thickness in the XD VTE sequence.

Error estimation was performed using Gaussian error propagation.

2.8 Mathematica Analysis Toolkit

A custom toolkit has been developed in the course of this thesis to enable the analysis of the various quality control parameters which have been investigated.

This toolkit is comprised of easily reusable Mathematica[21] modules which have been included in appendix A.

An extensive documentation of the used code, with the intention of enabling future reuse of the provided analysis routines, is provided in appendix A.2.

2.8.1 Settings

The following settings need to be changed in order to adjust the Mathematica[21] programs for analyzing a new measurement.

Signal to Noise Ratio

New masks need to be created. The program uses two mask images for the signal to noise ratio analysis. One mask is used for the noise area the other one for the signal area.

The easiest way to create this masks is to import one slice into Mathematica using the **Import** command, for an example on how to do this, see appendix A.9.

As soon as this data is loaded, it can be converted into an image using the command: `ImageAdjust[Image[dicomData[[1]]]]`. After creating this image from the slice data, the drawing tools can be used to draw the mask onto the image. Afterwards a mask can be created from the context menu under the point graphics editing, create mask.

For placement of the mask inside the program code see appendix A.4.

Ringings and Edge Overshoot

In the function `edgeAnalysis` the `xStart` and `xEnd` values have to be set to an area inside the line profile which will be used for calculating a signal average. Also inside this function the lines which are used for the edge analysis have to be set.

Edge Spread Function

The function `esf` requires the most complicated setup process. It is easiest to just copy the whole code of this function into another Mathematica notebook and display the submatrices created during the run of the function using the `MatrixPlot` command at each step.

In the first step the `xStart`, `xEnd`, `yStart` and `yEnd` values have to be adjusted. They should be chosen in such a way that the resulting sub matrix displays the whole ESF phantom including some surrounding data. This doesn't have to be cut very tight, as further submatrix processing will take place on this data.

Secondly this matrix has to be rotated in such a way that the edges of the edge spread function align with the y direction of the plot. This is achieved by changing the angle passed to the `rotatedImageRight=...` and `rotatedImageLeft=...` variables.

In the final step, just the edge with some ancillary data is extracted. This is performed when the `esfRight` and `esfLeft` variables are set. Care should be taken that this resulting submatrix only contains one edge and doesn't contain any unnecessary data at the top or bottom. The edge should now be going parallel to the y direction. And each line which is extracted along the x direction should have a single step inside of it.

Point Spread Function

For setting up the point spread function only one setting is required. Changing the `psfCenter` value. This value is the center of the point spread function which will be analyzed.

It is also possible to adjust the radius of data which is used for the point spread function analysis. This is done by changing the `radius` variables in both the `psf` and `psfAngle` functions.

Geometric Accuracy

The `diameter`, `lineDiameter` and `sliceDiameter` functions require no adjustments. These automatically cut off the bottom and top quarter of the matrix data to avoid erroneous results from areas where the phantom is not visible. Should the ratio by which the phantom fills the image area change dramatically adjusting this value might become necessary, this can be performed in the first line of the `sliceDiameter` function.

2.8.2 Validation of the LSF Analysis

The line spread function analysis method, based upon obtaining the modulation transfer function by taking the Fourier transform, has been validated using a simulated Gaussian function.

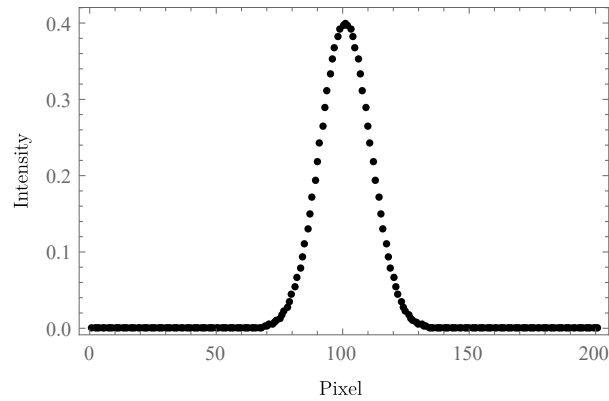


FIGURE 2.11: Gaussian function for validation of the LSF analysis method.

A discrete Gaussian function was created, as shown in figure 2.11, this function was analyzed using the `lsfSingleLine` function. The result of this analysis was 23.5913 pixels. The FWHM of the Gaussian was determined using `fityk[10]` and was found to be 23.5482 pixels.

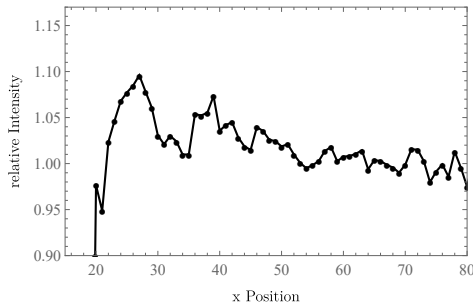
The results obtained are very close to each other, even down to a subpixel level and therefore validate the LSF analysis method used.

Artefacts

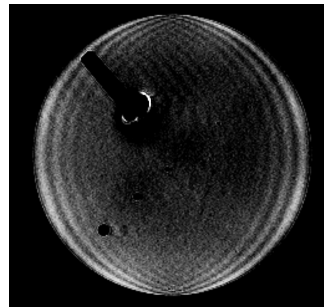
3.1 Gibbs Ringing

Gibbs ringing is an oscillating pattern which occurs where sharp edges are measured using insufficient resolution (at reduced k-space frequencies). The pattern is strongest along the measured edge. It can be described as a low pass filter in k-space.[30]

Two illustrations of the Gibbs phenomenon are shown in figures 3.1a and 3.1b.



(A) Line profile.



(B) 2D image with ringing in x direction.

FIGURE 3.1: Illustrations of the Gibbs phenomenon.

3.2 Edge Enhancement

As discussed in the introduction the image is created from k-space data which was sampled by following a specific k-space trajectory.

Edge enhancement is an artefact which is caused by a distortion of this trajectory. This distortion can, depending on the sequence used, have different strengths in different regions of k-space. Many sequences have a distortion around the central point of k-space. In this case the signal belonging to low spatial frequencies, or simple patterns as discussed in the introduction, are shifted to higher k-space values and therefore higher spatial frequencies.[2, 31]

For a homogeneous disk this distortion will be visible by the fact that the central region will have less signal and the outside edge of the structure will appear hyper intense.

Edge enhancement artifacts are caused by distortions in the k-space trajectory. For half-echo UTE sequences this k-space distortion leads to very noticeable artifacts as this distortion is strongest in the central frequency region in that case.

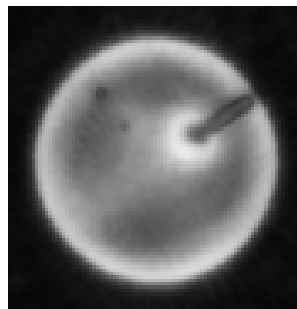


FIGURE 3.2: Illustration of an edge enhancement artefact. Digitally altered.

The primary cause of k-space trajectory errors is a difference between real and ideal gradient performance. The actual applied magnetic field is therefore different from that assumed for calculations therefore the mapping of a specific frequency to a point in k-space is distorted.

A major cause for this non ideal gradient performance are eddy currents in the gradients.[2]

In the case of UTE sequences a contributor to strong edge enhancement artefacts is the fact that the sequence begins data acquisition already while the gradient is still ramping up, as discussed in section 1.2.

There are some correction methods available, an attempt was made to implement one of these k-space trajectory corrections[2] but was not successful within the scope of this thesis. A prior work by Horn C.[3] has implemented such a correction for the CV UTE sequence in a different software version of the scanner system.

An example of such an artefact is shown in figure 3.2. Because these artefacts are caused by k-space errors they can look quite different while the same basic principle is causing them. More examples can be found in the paper “A Robust Ultrashort TE (UTE) Imaging Method With Corrected k-Space Trajectory by Using Parametric Multiple Function Model of Gradient Waveform” by Takizawa et al.[2].

3.2.1 Analysis Method

This artifact has been analyzed in the same manner as the Gibbs phenomenon. For a description of this method see subsection 2.5.

3.3 Blurring

The blurring artefacts encountered can most likely be attributed to a combination of k-space trajectory errors, as described in section 3.2, and noise present in the measurement before reconstruction.

Blurring can also be caused by signal decay during acquisition, which is relevant for UTE sequences.[32]

It would not be expected that this kind of blurring plays a significant role as the echo times are still short compared to the $T2^*$ of the silicone material.

3.4 Zero Point Artefact

A zero point, or zero line artefact, is caused by noise in the system which contains no spatial encoding information and is therefore placed in the central point at zero frequency and along this line in frequency encoding direction.[33, 34]

An illustration of a zero point artefact is shown in figure 3.3.

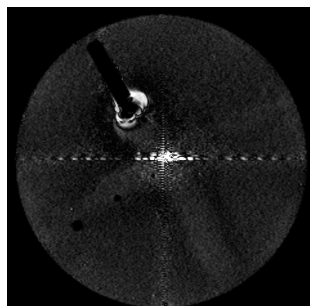


FIGURE 3.3: Illustration of a zero point artefact. Digitally altered based on multiple images of the XD VTE sequence.

This can appear as either a point, line, or lines in both directions, showing the side lobes of the sinc function of this pixel.[33]

3.5 Susceptibility

Magnetic susceptibility is a material constant which describes how strongly a material is magnetized when placed inside an external magnetic field.

This leads to artefacts in MR imaging because different parts of the sample no longer experience the same magnetic field. For a homogeneous sample, with no additional gradients or rf fields applied, every part would experience the static field B_0 . When materials with different magnetic susceptibility are present inside the sample, this assumption no longer holds true.

Differences in the magnetic field inside the sample lead to additional shifts in frequency and therefore the assumptions taken when mapping frequencies back to points in k-space are no longer true. Additionally this change in frequencies causes a faster transversal relaxation, as described in section 1.1.1.2.

Pixel shifts, Δr , depend on the magnetic susceptibility difference, $\Delta\chi$, the field strength B_0 , the shape of the object expressed by an object constant, c_{shape} , and the gradient strength G . The relationship given by Elster A., is shown in equation 3.1.[35]

$$\Delta r = \frac{\Delta\chi B_0 c_{\text{shape}}}{G} \quad (3.1)$$

These susceptibility artefacts are especially visible in gradient echo sequences.[36]

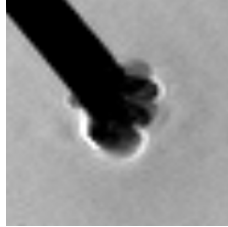


FIGURE 3.4: Artefacts most likely caused by susceptibility differences between the phantom silicone and air bubbles.

Air bubbles can cause these artefacts. This has been demonstrated experimentally.[37] The artefacts encountered during the course of this thesis seem comparable in appearance to the published images of susceptibility artefacts caused by air bubbles.

An example of such an artefact, as encountered throughout this study, is shown in figure 3.4.

Phantom



FIGURE 4.1: Photo of the FV2 silicone filed UTE phantom constructed for this thesis.

4.1 Structure

4.1.1 Resolution

The phantom contains multiple structures for resolution measurements in the transversal plane using negative contrast. Multiple cylindrical objects were placed parallel to the main axis on a single line.

A cuboid is placed in the other main diagonal, this can be used for edge spread function resolution measurements, as described in section 2.4.1.

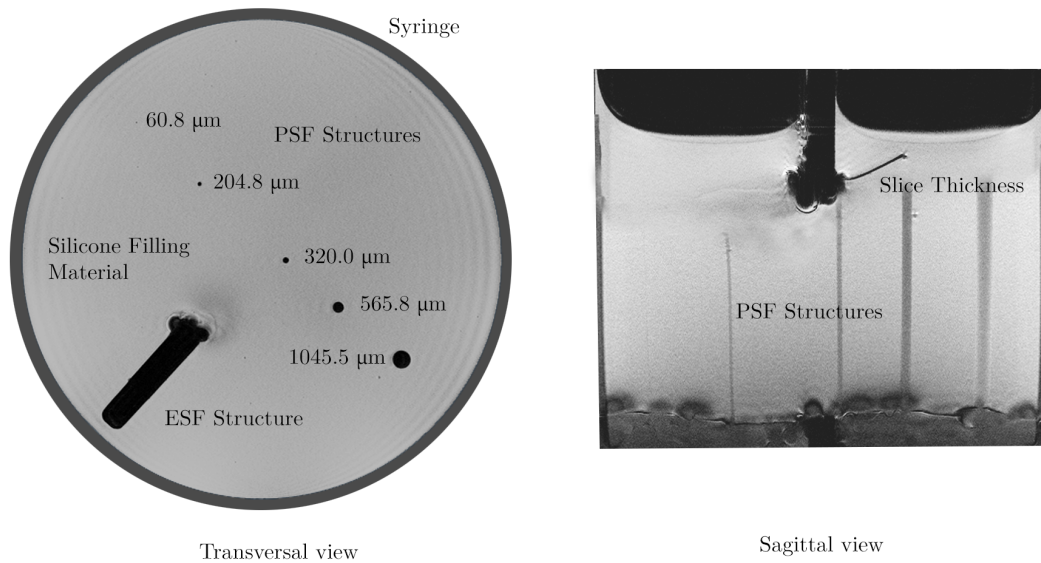


FIGURE 4.2: Structure of the phantom FV2 as used in this thesis. The views are based on MRI images but have been digitally altered.

Two views of the phantom are shown in figure 4.2. The diameter measurements of the PSF structures have been performed with a microscope, except for the largest structure. With respect to the microscope calibration the estimated error for each of these measurements is $0.2\mu m$ and $0.5\mu m$ for the largest structure.

The inner structures are constructed of different materials. The smallest two, are made of synthetic fibers. The remaining structures are glass capillaries which are hollow.

All these structures have been put into place and secured with a cyanoacrylate adhesive before the structure was filled with silicone as described in section 4.3.

4.1.2 Slice Thickness

The phantom contains a $100\mu m$ glass plate, angled at $(28.5 \pm 0.2)^\circ$ to the transversal plane, for measuring slice thickness. As shown in figure 4.2.

4.2 Uniformity Phantom

In addition to the complex resolution and slice thickness phantom a uniformity phantom has also been constructed.

This phantom consists of a hollow cylindrical structure filled with the same silicone material, prepared in the same way.

4.3 Material

The phantom is filled with a two component silicone, which was premixed and deaerated in vacuum.

The product “Silikon SF00” distributed by the company “Silikonfabrik.de” was used. This silicone is a room temperature vulcanization silicone, its vulcanization is based on a catalyst with base reaction, because of this it vulcanizes without contraction which allows for a more accurate casting of the phantoms structures.

According to the product datasheet the material has the following properties: mixture 1:1, RTV2 silicone, vulcanization time at $23^\circ C$ 1.5 hours, mixture viscosity 2000cP, Shore A hardness after vulcanization is 0ShA and Shore OO hardness is 55 ± 4 ShOO, density $1.06 \frac{g}{cm^3}$, vapor pressure $< 0.01 kPa$ at $20^\circ C$. [38]

Vulcanization has been performed by mixing both components in a 1:1 mass ratio, the ratio has been determined by using a high precision scale. Afterwards the mixture was stirred manually using a wooden rod. Deaeration was performed in vacuum until the material no longer boiled up. This treated mixture was then pured into the prepared phantom structure.

4.3.1 Spectrum

The spectrum of the material was measured using the uniformity phantom. By placing the shim area inside the silicone material. Beforehand a frequency adjustment was performed until it converged. A transmitter adjustment and four automatic shim adjustments were also performed.

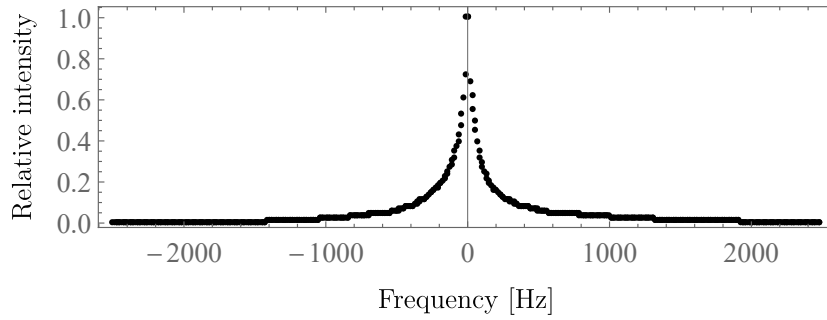


FIGURE 4.3: Spectrum of the silicone material used inside the phantom. Central frequency 297.222008 MHz. Acquired using the frequency adjustment in the 7T Magnetom MR scanner using the STEAM 10 Hz sequence.

For obtaining the spectrum itself a 10 Hz resolution STEAM frequency adjustment was used. The resulting screenshot was saved. Based on this screenshot the data was extracted by processing the image in Mathematica. The result of this calculation is shown in figure 4.3.

This spectrum should be a Lorentzian function, as this is the frequency domain representation of the exponential decay in the time domain. [39]

A fit employing `fityk`[10] using a Lorentzian function seemed not meaningful as the shape deviates from a Lorentzian considerably. The FWHM obtained from this fit was $(189.4 \pm 3.1) \text{ Hz}$, this result should be disregarded.

The FWHM was therefore determined using a piecewise polynomial interpolation function, with a search precision of $\frac{1}{1000}$.

This gives a FWHM for this spectral line of $\nu_{1/2} = (94 \pm 15) \text{ Hz}$. The error is based on the 10 Hz resolution of the frequency adjustment sequence itself and error propagation for subtractions $\Delta\nu_{1/2} = \sqrt{10^2 + 10^2} = 10\sqrt{2}$.

4.3.2 T1 of the Phantom Silicone Material

For some of the initial measurements T1 was estimated based upon flip angle optimization. These initial calculations were also used for setting the standard protocols.

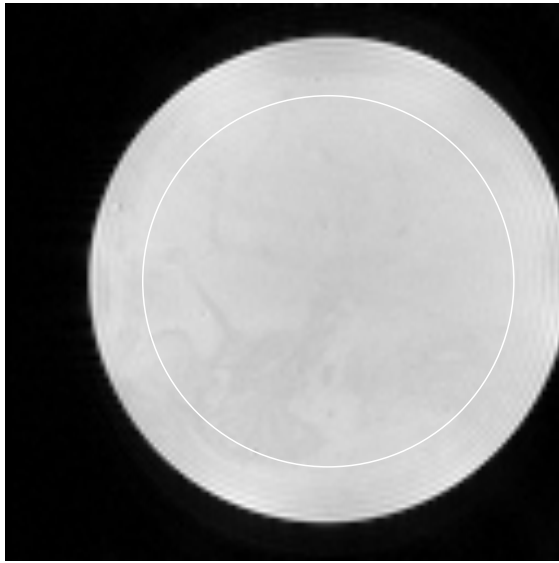
Further measurement were performed using an IR sequence, these also turned out to contain errors. Therefore the flip angle used in the standard protocols and other measurements is not exactly the Ernst angle. The same angle was used for further measurements as a considerable amount of measurements had already been performed with protocols based on these initial calculations. This was done to ensure that all the data remains comparable to each other. Therefore slightly better signal to noise ratios can be expected when using the correct flip angle.

In a later stage the choice was made to perform these measurements again using a partial saturation recovery measurement.

Repeated 90° pulses are applied to the sample with decreasing repetition times.[40] The expected behavior for this measurement is shown in equation 4.1.

$$M(TR) = M_0 \left(1 - e^{-\frac{TR}{T_1}}\right) \quad (4.1)$$

These measurements have been performed using a spin echo sequence starting at a repetition time of 4.5s down to the minimum repetition time which could be set in the sequence of 0.279s. The uniform phantom described in section 4.2 was used for this.



TE	8.5 ms
TR	4500 ms
Avg	1
FOV	(36. x 36.) mm ²
BW	195 $\frac{Hz}{Px}$
Slice	800. μm
α	90°
Matrix	128 x 128
Voxel	(281.2 x 281.2 x 800.) μm^3
TA	09:33
Seq	*se2d1

FIGURE 4.4: Spin echo sequence for the T1 measurement of the phantom silicone material. Also showing the region of interest used for the T1 fit. The resulting placement was slightly offset from the slice positions displayed on the localizer when setting up the measurement. Therefore the phantom is not directly in the center of the FOV.

A series of measurements with multiple slices has been obtained this way. The analysis was performed by placing a region of interest inside the slice to be analyzed, see figure 4.4. For this region of interest the mean value has been obtained. In addition a standard error of this mean value has been calculated by dividing the standard deviation inside this ROI by the square root of the number of pixels in the ROI.

This data was obtained for all the TR measurements. Afterwards the data was normalized by dividing all intensity values by the value associated with the longest TR in this list.

Based on these data a fit was performed using Mathematicas[21] `NonlinearModelFit` function. The function fit is given in equation 4.1.

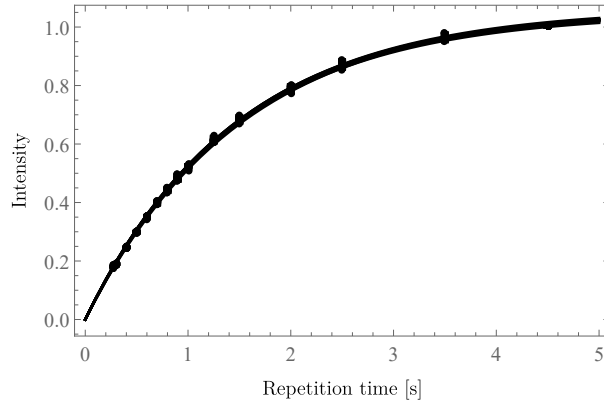


FIGURE 4.5: Fit of T1 using a partial saturation recovery using a spin echo sequence. This figure shows all 11 slices and their respective fits used in the final calculation of the T1 value of the silicone material.

In order to obtain better statistics this procedure has been repeated for 11 slices in the series. All of the data point and resulting fit functions are shown in figure 4.5.

Please note that figure 4.5 does contain error bars but these are smaller than any reasonably sized plot marker.

Mean values obtained from the 11 different T1 fits for each slice give a T1 value of $(1.4690 \pm 0.0068)s$. Using the standard error as described in equation 2.1.

For M_0 a value of $(1.0588 \pm 0.0017)s$ was obtained from the fit.

Initial investigations by the IMBA resulted in a T1 of about 1.4s in their system.

4.3.3 T2* of the Phantom Silicone Material

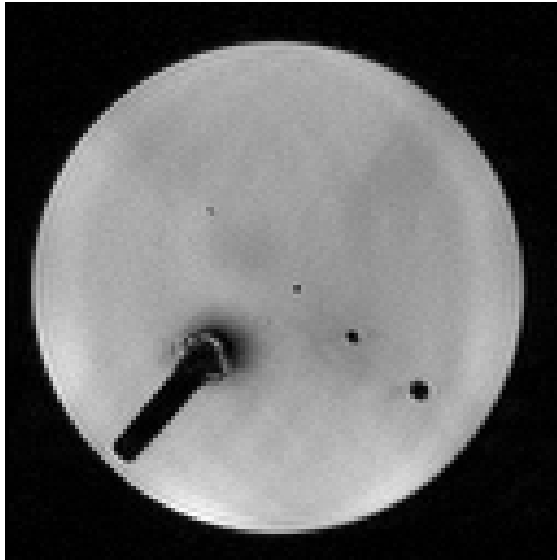
The T2* time of the material was determined using a measurement series measured using the XD VTE sequence.

Measurements were performed with the parameters shown in figure 4.6. The following TE times were measured and included in the fit: [0.8 1.0 1.5 2.0 2.5 3.5 4.0 8.0] ms.

The resulting T2* map is shown in figure 4.7.

Figure 4.7 also contains the ROIs which were used for calculating the T2* time of the silicone used in the phantom. The result was obtained by calculating a mean of all the ROI mean values weighted by their area. Standard deviation values were also weighted by the area.

This gives a T2* time of $(11.6 \pm 1.1)ms$ for the silicone used in this phantom. The standard error was obtained by dividing the standard deviation by the square root of the number of different areas.



TE	0.75 ms
TR	100 ms
Avg	1
FOV	(32. x 32.) mm^2
BW	488 $\frac{Hz}{Px}$
Slice	800. μm
α	13°
Matrix	128 x 128
Voxel	(250. x 250. x 800.) μm^3
TA	01:42
Seq	XD VTE

FIGURE 4.6: One of the slices used for the T2 mapping of the silicone filling material used in the phantom.

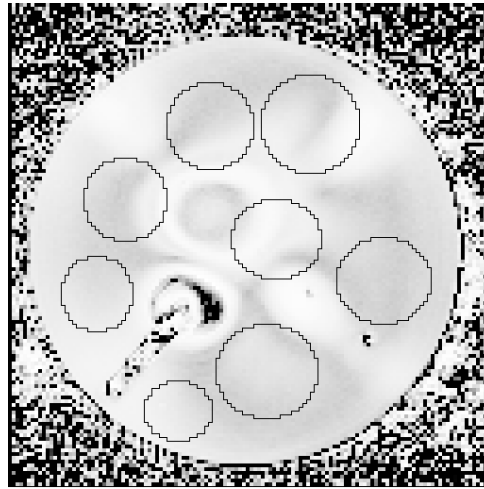
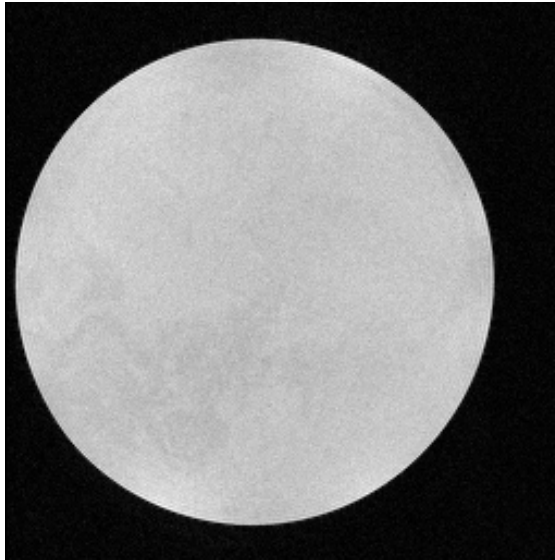


FIGURE 4.7: T2* map for the silicone used in the phantom. Also depicting the ROIs used for the analysis.

Due to the combined contribution of T1 and T2* in the gradient echo sequence this result should only be considered a rough approximation of the actual T2* time.

4.3.4 Uniformity of the Material

Investigation of the material inside the uniformity phantom, section 4.2, showed substructures inside the material which are identical between different measurements and are unlikely to be artefacts. See figure 4.8.



TE	8.5 ms
TR	1000 ms
Avg	3
FOV	(36. x 36.) mm^2
BW	501 $\frac{Hz}{Px}$
Slice	800. μm
α	90°
Matrix	256 x 256
Voxel	(140.6 x 140.6 x 800.) μm^3
TA	12:50
Seq	*se2d1

FIGURE 4.8: Uniform silicone phantom analyzed using a spin echo sequence.

These structures are probably differences caused by variations in the vulcanization process at different spots. The same structures are not visible in the other sequences used in this thesis. This can be explained by the strong artefacts and low resolutions in these sequences.

4.3.5 Air Bubbles

Even though the silicone was deaerated before filling the phantom some air bubbles are visible inside the phantom structure on high resolution MR images.

These are mostly indistinguishable from noise, especially at low spatial resolutions but could cause some small skew of the mean value in signal areas and thereby lower the signal to noise values obtained.

The bubbles visible inside the bulk of the material are estimated to be in the $100\mu m$ to $300\mu m$ range.

No semi opaqueness or visible air bubbles could be observed after pouring and vulcanization of the material.

Due to these air bubbles no uniformity measures have been analyzed as any such result would not be very reliable.

Larger air bubbles along some of the inside edges can cause susceptibility artefacts as described in section 3.5.

Measurements

5.1 MRI System

All measurements, except the ones in chapter 9, were performed at the MR center of Excellence at the Medical University of Vienna.

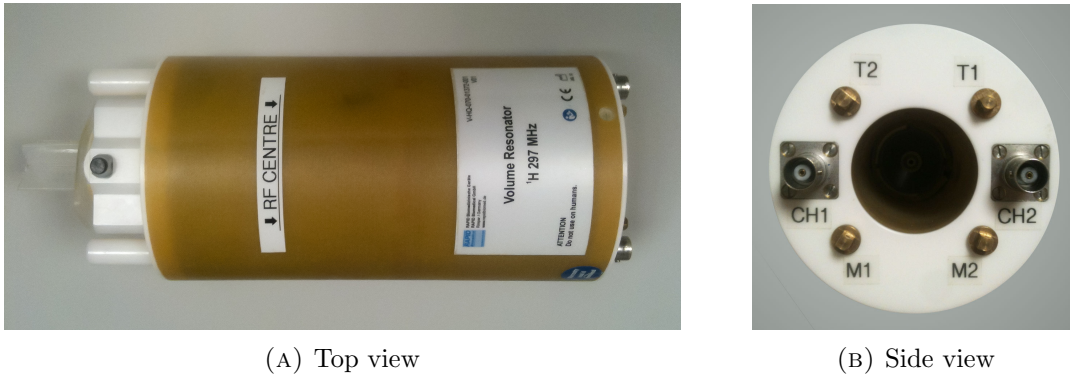


FIGURE 5.1: 39mm two channel RX/TX 1H resonator produced by RAPID Biomedical used for the XD VTE, CV UTE and DA-3DPR measurements.

A Siemens Magnetom 7T human scanner with a micro gradient insert and a 39mm, two channel, coil were used.

This micro imaging system is based upon ongoing research and is not commercially available.

5.2 Measurement Preparation

The procedure described as follows was used to prepare each measurement.

Micro imaging is separated, hardware wise, from the whole body functions of this 7T scanner installation. A separate console is available for the micro imaging system. Therefore the whole system has to be shut down. While shut down the connections are switched from the whole body system to the micro imaging system using a large switch (FSS) on top of the scanner. After performing this switching the system is started back up again and the micro imaging console is turned on manually.

Additionally the temperature measurement system, as described in section 5.5, is started up.

The phantom was placed inside the coil, figure 5.1, such that it could not move or vibrate freely. This was accomplished by wrapping paper around the phantom and later on by modifying the phantom by fixing foam on the outside of the phantom using double sided adhesive tape, streamlining phantom insertion and removal procedures. Placement was performed in such a way that the central part of the phantom, containing the silicone and structures, was placed slightly outwards of the coils RF center. This was done in order to allow measurements of this area without central point artefacts.

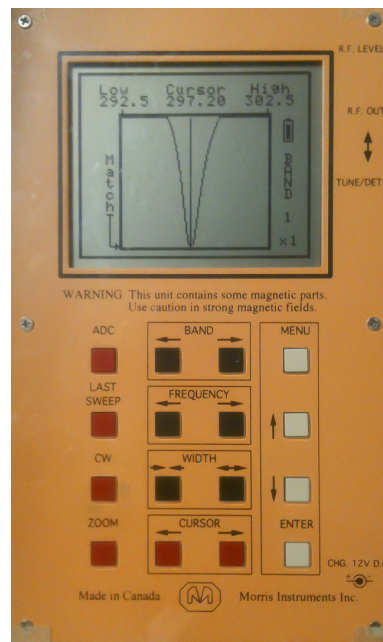


FIGURE 5.2: Tuning and matching of the coil with the phantom already inserted.

With the phantom inside the coil a frequency adjustment was performed on both channels. Both channels were tuned and matched. Crosschecking the first channel after completing adjustment on the second channel. See figure 5.2.

The micro gradient insert was placed on the scanners patient table. The coil inserted into the insert and connected to the adapter which was also connected to the scanner.

A patient was registered. This is necessary in order to enable the patient positioning mode. The gradient insert was positioned using the scanners positing function, placed inside the B_0 field isocenter and secured in place.

At this point the insertion of the phantom into the scanner is complete. The final part are the adjustments on the scanners Syngo console.

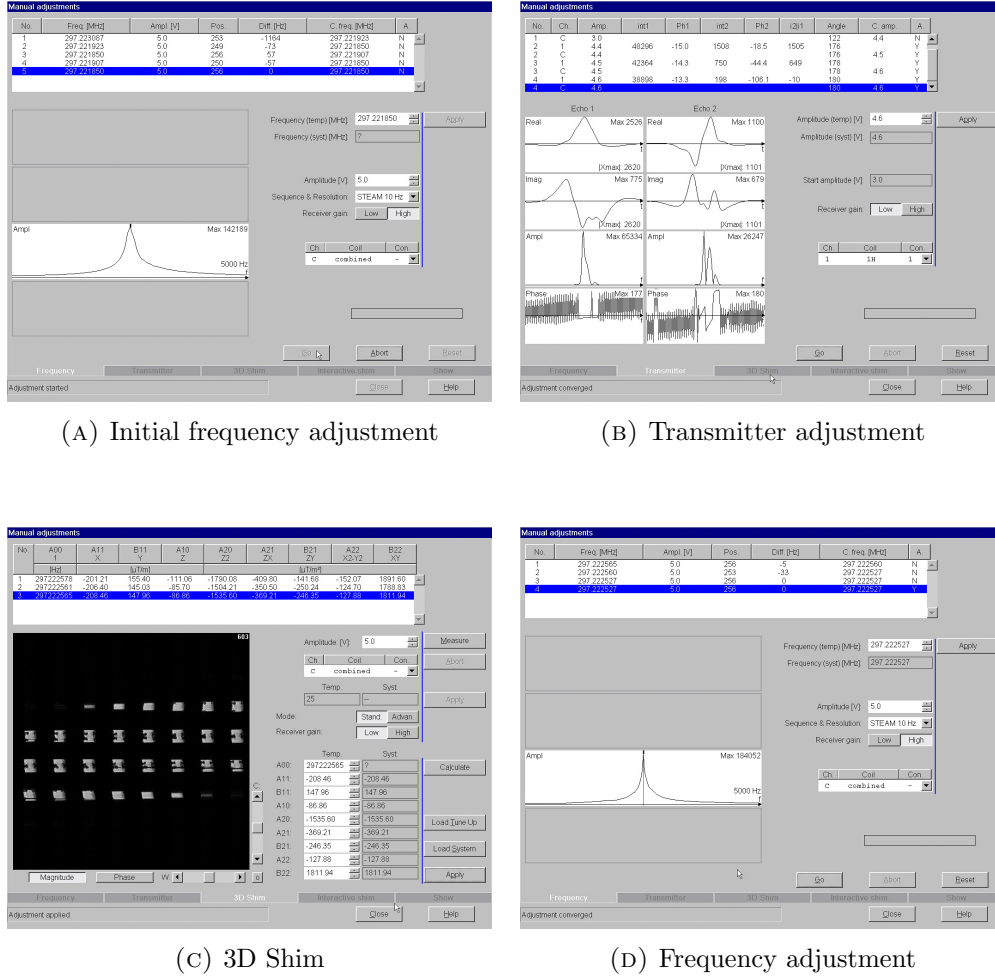


FIGURE 5.3: Adjustment procedure used for measurement preparation.

Adjustments on the scanner are only possible when a sequence is loaded and opened. For this purpose a localizer sequence was used.

Initially a frequency adjustment was performed. This was run by first performing an FID 400Hz adjustment, then FID 10Hz and STEAM 10Hz. The Steam 10Hz adjustment was repeated until the adjustment converged. It is important to not press the “Apply” button at this time, because it causes frequency adjustment warnings later on.

In the next step the transmitter was adjusted. This was also repeated until the adjustment converged.

Shimming was performed next. This was done using the built in 3D shim tab, “Measurment”, “Calculate” and “Apply”. Shimming was repeated multiple times until the calculated adjustment values did not vary too much between each step, usually about 3 shim steps were performed.

Finally another frequency adjustment, starting again with the FID 400Hz measurement going all the way down to the STEAM 10Hz sequence, was performed.

Screenshots of all these adjustment steps are shown in figure 5.3.

5.3 Standard Protocol

5.3.1 Goal

Standard protocols have been defined to provide a baseline for variation within each particular sequence. These have been developed with the goal of having a comparable settings set.

Rather conservative TR values were chosen to ensure that the sequences stay within a safe thermal operating range for all variations during overnight measurements for which the thermal behaviour could not be closely monitored.

5.3.2 Target Parameters

Total acquisition time was chosen to be around 20 minutes.

Echo times were determined by the lowest possible value for all sequences, limited by XD VTE, and TE was set to 0.67ms.

Repetition times were set to 200ms for all standard sequences, providing sufficient thermal leeway with a factor 5 safety.

A bandwidth of $300 \frac{Hz}{px}$ was used. Providing sufficient bandwidth for the line width of the phantom material, while still allowing safe thermal operations.

The resultant flip angle based on initial calculations of T1 for the material was set at 39° , resulting in a slight out of plane steady state free precession status. The optimal flip angle for this phantom and parameters would be 30° .

Field of view was chosen at $(32\text{ mm} \times 32\text{ mm})$, where applicable.

Parameter	Value
TA	20 min
TE	0.67 ms
TR	200 ms
α	39°
BW	$300 \frac{Hz}{px}$
FOV	(32 mm x 32 mm)
Matrix	256x256

TABLE 5.1: Standard sequence target parameters condensed overview.

Base matrix size was chosen at 256x256 pixels.

The remaining parameters were varied in such a way that a good performance within the TA of about 20 minutes was obtained.

A concise version for quick reference is given in table 5.1.

5.4 Parameter Variation

For each of the sequences the whole parameter space was explored by varying the standard sequences. Each variation was based on the standard sequence and only a single parameter has been changed. The images obtained this way were then analyzed using the Mathematica Analysis Toolkit described in section 2.8.

5.4.1 Overview of the Result Quantities

Table 5.2 gives an explanation of the quantities provided in the results table.

SNR	Signal to noise ratio. Calculated as explained in section 2.3 as well as equations 2.2 and 2.4.
SNR _{corr}	Signal to noise ratio, corrected for the magnitude Fourier transformation during reconstruction. As explained in section 2.3.2 and equations 2.5 and 2.6.
Resolution [μm]	Resolution obtained by evaluation of the edge spread function, as described in section 2.4.1.
PSF Y and X [μm]	Resolution obtained by evaluation of the point spread function, as described in section 2.4.2. This quantity is rarely shown as this calculation is very susceptible to noise and mostly led to non trustworthy results.
Ringings / Edge overshoot [%]	Measure for the overshoot along the left and right edges of the phantom, in percent of the average signal in the inner phantom area. For a more detailed explanation see section 2.5 and section 3.1.
Diameter [mm]	Diameter of the phantom as calculated from the image. Process described in section 2.6.
Geometric error [%]	The standard deviation of the diameter for different angles, divided by the mean diameter for this slice, in percent. Section 2.6 and equation 2.20.

TABLE 5.2: Overview of the evaluation parameters in quality control, also found in parameter variation result tables.

5.5 Thermal Behavior

The temperature of the microgradient system used requires close monitoring to ensure that no overheating occurs which could cause damage to the gradient system, and even the rf coil inside it.

For this purpose a special temperature measurement system is available. Based on multiple PT100 sensors inside the gradient system. These can be monitored from a dedicated workstation in the 7T console room, where these resistance measurements are converted to temperature measurements.

Within the scope of this thesis the description of the thermal behavior of the sequences is more qualitative, although some quantitative measurements have been performed.

For these measurements the monitoring workstation was used to record the temperature, whereas always the peak sensor temperature of all sensors is meant.

All these measurements have been performed by varying the repetition time of the standard protocols by the following values: 13ms, 25ms, 50ms, 100ms, 200ms. Where 13ms was the lowest possible for all sequences and 200ms is the repetition time of the standard protocols.

XD VTE

6.1 Sequence

The XD VTE Sequence is a special pulse sequence for short variable TE, made available within a research cooperation.[9] It is based on a 3D sequence spoiled gradient echo sequence (section 1.1.4).[9]

Variable TE means that the sequence has been written such that for each sampling point in k-space the shortest echo time possible is used. This means that the central points of k-space have the shortest echo times. According to the authors this minimum TE can be achieved for 30%-40% of the phase encoding steps.[9]

This sequence also employs an asymmetric read out gradient for the first echo.

For this sequence a minimum TE of 0.5ms can be set.

But this minimum TE is dependent on matrix size, for the matrix size used for the standard protocol, 256x256, the minimum TE is 0.67ms. For larger matrices of 384 the TE becomes 0.77ms and 0.87ms for a 512x512 matrix.

Special thanks to X. Deligianni for making this sequence available for this research project.

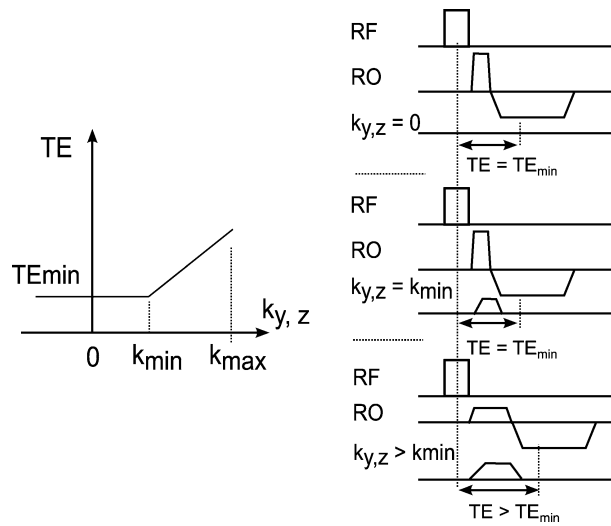


FIGURE 6.1: XD VTE sequence diagram and illustration of variable TE.
Image source: Deligianni, X.[9]

6.2 Standard Protocol

A standard protocol has been defined for the XD VTE sequence using the goals described in section 5.3. Defined in table 6.1.

Parameter	Value	Parameter	Value
TA	20 min 21 sec	BW	$300 \frac{\text{Hz}}{\text{px}}$
TE	0.67 ms	Slice Thickness	$400 \mu\text{m}$
TR	200 ms	Avg	3
α	39°	RF Spoiling	on
FOV	$(32 \text{ mm} \times 32 \text{ mm})$	Filters	none
Matrix	256x256		

TABLE 6.1: XD VTE standard protocol.

The flip angle was calculated based on an erroneous T1 value and is therefore not optimal, spoiling was ignored while calculating the flip angle in order to obtain results which are directly comparable between the different sequences investigated. For actual measurements improvements in SNR can therefore be expected.

A single slice of the images obtained using this standard protocol is shown in figure 6.10.

6.2.1 Signal to Noise Ratio using ROIs

The signal to noise ratio was obtained as described in section 2.3.

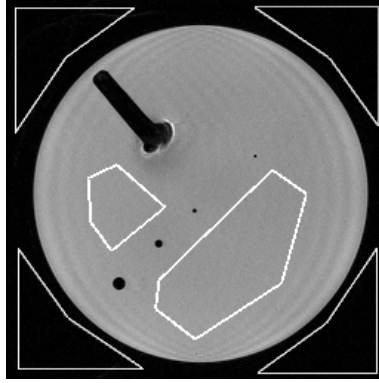


FIGURE 6.2: Regions of interest used for the SNR analysis in the XD VTE sequence.

Regions of interest used are depicted in figure 6.2.

All eight slices were used for the analysis. The signal values obtained are 1136.92, 1045.78, 920.69, 835.44, 838.81, 928.35, 1052.71, 1139.43 and the noise values are 14.38, 14.14, 13.61, 13.73, 13.1, 13.82, 14.55, 14.76. **This gives a signal to noise ratio, calculated using the mean values of all the slices, of $46. \pm 1.5$.**

6.2.2 Signal to Noise Ratio using Difference Images

Signal to noise ratio was also measured using difference images as described in the NEMA MS 1-2008 (R2014) standard[4]. Two consecutive measurements were acquired using the same settings and system calibration. Eight difference images were created by subtracting the same slices in the two different measurements. Based on these the mean value of the signal in the ROIs of the first image series were calculated and divided by the standard deviation of the data inside the same ROIs applied to the difference image. These were then also corrected with a factor of $1/\sqrt{2}$ This method is also described in more detail in section 2.3.3.

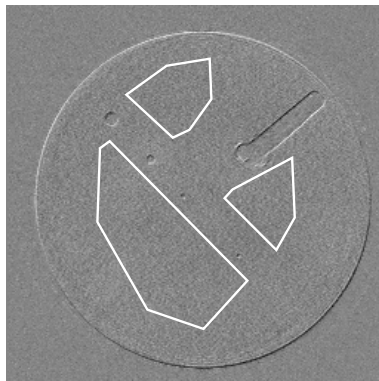


FIGURE 6.3: Difference image of two successive slices used for SNR calculation.

A difference image used for this analysis with the regions of interest marked is shown in figure 6.3.

The results for these 8 slices were 59.7781, 55.8883, 50.1421, 47.2369, 47.4557, 51.6906, 57.6151, 61.0942.

Based on these 8 slices a signal to noise ratio obtained from difference images SNR_{diff} of 53.9 ± 2.0 was obtained.

There is quite a large difference between these two methods of obtaining the signal to noise ratios. The difference in the results might be caused by the strong artefacts present in those images.

The analysis has been repeated on a second set of images to confirm the results and error margins. The resulting SNR_{diff} for the second set of images was 26.93 ± 0.97 , which is equal to the SNR_{diff} of the first image set within error margins.

6.2.3 Resolution

6.2.3.1 Edge Spread Function

The resolution was primarily analyzed using the edge spread function.

Edge spread function regions of interest used for this analysis and all parameter variations based upon the standard protocol are shown in figure 6.4. This figure also depicts the left and right hand side edge spread functions for the standard protocol of the XD VTE sequence.

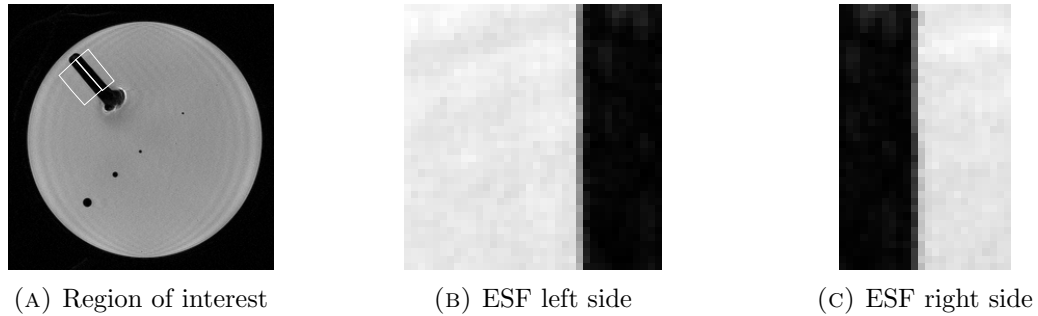


FIGURE 6.4: Edge spread function region of interest as well as left and right edge spread functions for the XD VTE standard protocol. Both edge spread function cut outs are scaled to maximum dynamic range inside the cut out.

For different matrix sizes the same ROIs were used scaled by the quotient of the new matrix size to the standard protocol matrix size.

A cluster plot and a density histogram of all the 304 Fourier transforms, from a total of 8 different slices are shown in figure 6.5. This also serves to illustrate that good statistics are vital

in obtaining meaningful results for the resolution, as the difference between single line profile results are quite substantial.

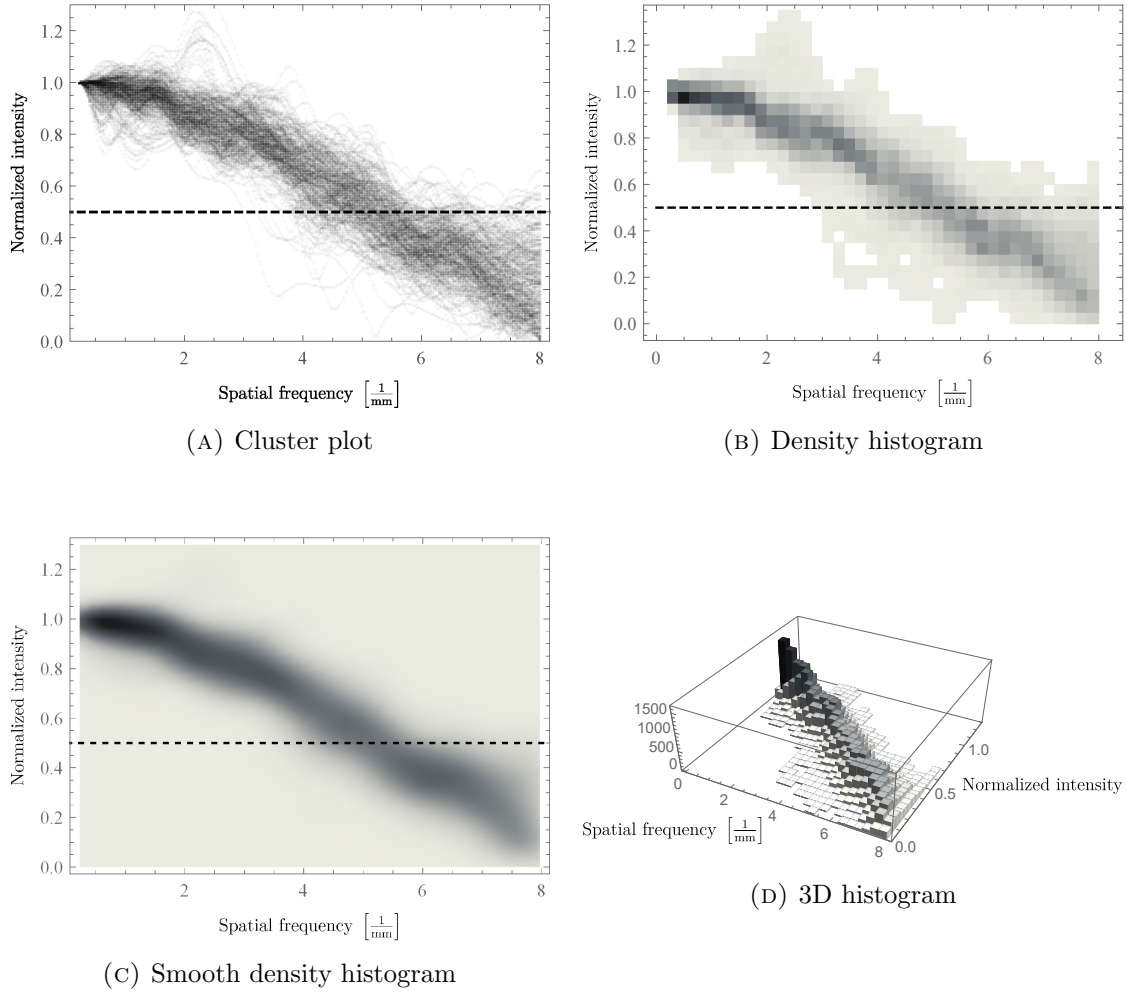


FIGURE 6.5: All 304 modulation transfer functions used for the analysis of the XD VTE standard protocol. The density histogram has a bin size of $0.2\frac{1}{mm}$ on the x-axis and 0.05 on the y-axis. The smooth density histogram was generated using Mathematicas `SmoothDensityHistogram` function. The 3D histogram shows the number of data points in each bin in its height, this includes more than 304 data points in total due to zero filling. Bin size for the 3D Histogram is $0.3\frac{1}{mm}$ on the x-axis and 0.05 on the y-axis. Please note that these graphs are only shown to illustrate the shape and were not used in any way to obtain the numerical results for the ESF based resolution.

Based on the modulation transfer functions, obtained by taking the numerical derivatives of the edge spread functions, the following mean resolutions have been obtained for the different slices: (0.19938, 0.204606, 0.199371, 0.213623, 0.207052, 0.20799, 0.209478, 0.202297) μm . Using the standard error estimation, equation 2.1, and the mean values of the slices we **obtain a resolution, based on the ESF, of $(205.5 \pm 1.8)\mu m$ for the XD VTE standard protocol** at a pixel size of $125\mu m$.

The density histogram provides a clearer picture of the mean value of the modulation transfer function and proves therefore more useful for further comparisons in this thesis.

Figure 6.5 contains all possible plot types for displaying the modulation transfer function data. As can be seen in this graph each of the visualization options provides slightly different information but they are each strongly correlated and can all be used to gain a basic understanding of the MTF shape and resolution limit. The `SmoothDensityHistogram` provides the clearest representation of the resolution limit.

It also becomes quite clear that a large statistical ensemble, 304 modulation transfer functions for each edge spread function analysis in this case, is very helpful in obtaining meaningful data as each modulation transfer function has a quite large standard deviation. The standard deviation expected for a resolution measurement obtained from only a single modulation transfer function would be $1.8\mu m * \sqrt{304} = 31.4\mu m$.

6.2.3.2 Edge Spread Function using LSF Fit

This analysis has only been performed for the XD VTE sequence and only in order to validate the results obtained from the Mathematica Analysis Toolkit.

The edge spread function was determined as described above. A discrete numerical derivative of this edge spread function was then calculated, yielding the line spread function.

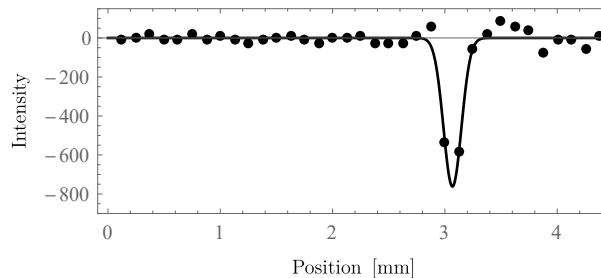


FIGURE 6.6: Line spread function obtained from the edge spread function and fitted using a Gaussian function in `fityk[10]`.

This line spread function was exported into `fityk[10]` and fitted using Gaussian fits. In total 9 different lines were used in the analysis. One example line is shown in figure 6.6.

The results of this analysis should be viewed very cautiously as a Gaussian fit is probably not the perfect match for this shape and sample size is rather small. In addition the FWHM of this Gaussian functions does not necessarily reflect the 50% modulation limit used as the primary definition of the resolution limit, as the shape of the LSF is not necessarily Gaussian.

The resulting resolution based on these 9 line spread functions obtained from the edge spread function is $(164 \pm 10)\mu m$. The error shown is the standard error as described in equation 2.1.

6.2.3.3 Point Spread Function using Fourier Transform

The point spread function was also used to attempt an analysis of the resolution integrating the PSF into the LSF and using the Fourier transform as an approximation of the actual modulation transfer function, ignoring the PSF phantom size and shape. This analysis was performed as described in section 2.4.2.

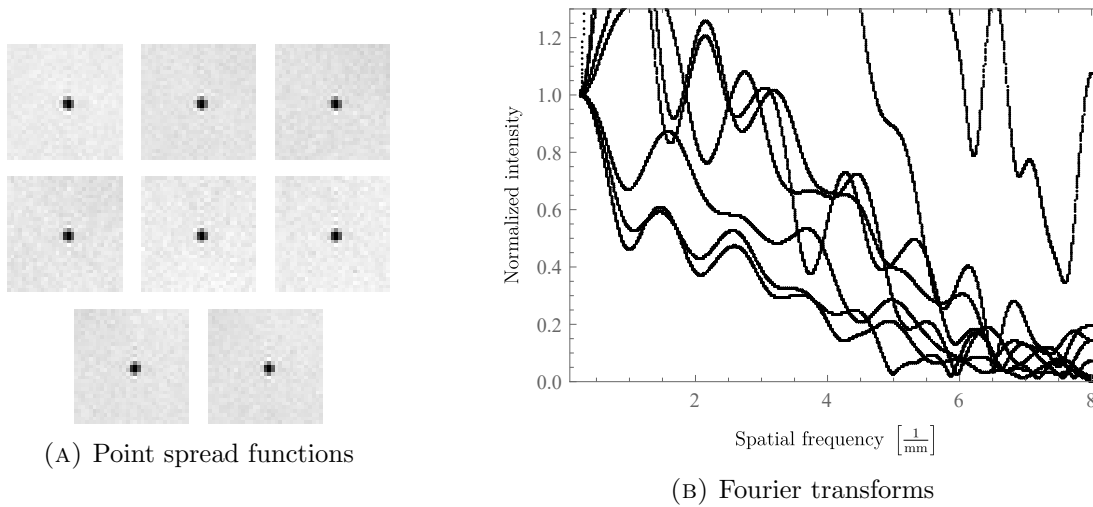


FIGURE 6.7: Fourier transforms obtained from the point spread functions for 8 different slices in the XD VTE standard protocol. Phantom size $(204.8 \pm 0.2)\mu m$.

The Fourier transforms, obtained from the point spread function of the $(204.8 \pm 0.2)\mu m$ PSF phantom structure, are shown in figure 6.7. As can be seen these are very erratic and do not provide a good measure of the actual resolution.

It should also be noted that the object size itself is very close to the expected resolution and any result obtained from this would still remain highly doubtful.

6.2.3.4 Point Spread Function using Gaussian Fits

In an alternative approach the point spread function has been analyzed by integrating it, as explained in section 2.4.2, and then performing a manual baseline correction and Gaussian fit.

The baseline correction was performed by placing a spline with multiple points along the baseline in `fityk`[10], then subtracting the baseline from the data points. Afterwards a Gaussian peak has

been placed in the correct area and a Levenberg-Marquardt fit has been run in fityk[10]. This has been repeated for all 8 slices.

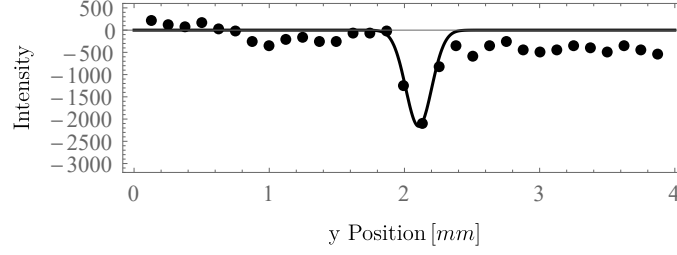


FIGURE 6.8: Point spread function analysis using Gaussian fits in XD VTE. Data points shown are without spline baseline subtraction but with constant baseline adjustment performed by subtracting the average of the data points left of the peak.

This method provided a full width half maximum (FWHM) for the 8 slices of $(0.1621 \pm 0.007, 0.1777 \pm 0.0068, 0.1842 \pm 0.0037, 0.238 \pm 0.011, 0.1685 \pm 0.0056, 0.2523 \pm 0.0062, 0.2165 \pm 0.0034, 0.2253 \pm 0.0041) \mu m$ giving a **mean resolution in y-direction obtained from the PSF using Gaussian fits of $(203 \pm 33) \mu m$** . The pixel size for this standard protocol is $125 \mu m$.

One important note to make is that the result is essentially the size of the phantom structure itself, this structure was chosen as the next smaller PSF phantom structure with a size of $(60.8 \pm 0.2) \mu m$ was not visible in the acquired image and could therefore not be used for the analysis. Therefore the $(204.8 \pm 0.2) \mu m$ phantom structure was used for this analysis.

Comparing this result of $(203 \pm 33) \mu m$ to the result obtained from the ESF, using the LSF, MTF analysis method, of 205.5 ± 1.8 these are equal within error margins.

The mean value and standard deviation have been obtained using a Monte Carlo simulation[41], which used the original input data as inputs to a random number generator, generating random numbers from a normal distribution with mean values of the FWHM and standard deviation the size of the standard error associated with that FWHM value. The ensemble size for this simulation was $16 \cdot 10^6$ elements. The size has been increased until the output mean and standard deviation remained constant up until the third error significant digit, in this case $203.09xx$ where x digits are non convergent.

6.2.4 Diameter

Analysis of the diameter is performed as described in section 2.6.

Figure 6.9 shows the length measurements obtained from the algorithm given in figure 2.7 in section 2.6. Based on these start and end points diameters are calculated and the maximal

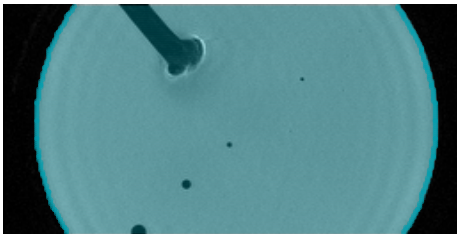
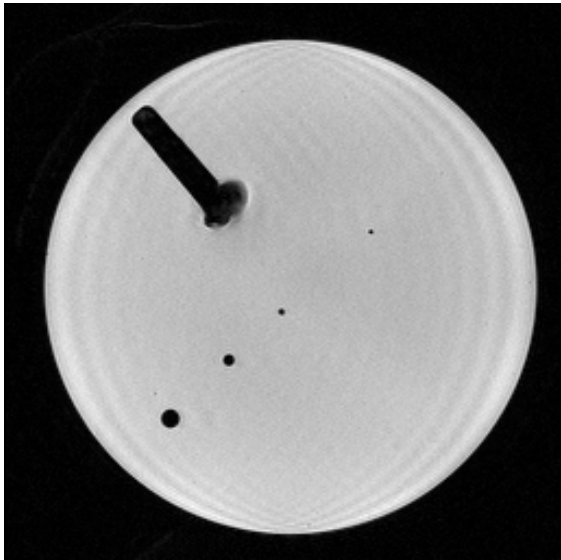


FIGURE 6.9: Lengths in a single slice of the XD VTE standard protocol used to determine the diameter.

length is used as the diameter. **This gives a diameter of $(28.1933 \pm 0.0013)mm$ for the XD VTE standard protocol.**

6.2.5 Results



TE	0.67 ms
TR	200 ms
Avg	3
FOV	(32. x 32.) mm ²
BW	300 $\frac{Hz}{Px}$
Slice	400 μm
α	39°
Matrix	256 x 256
Voxel	(125. x 125. x 400.) μm^3
TA	20:33
Seq	XD VTE

FIGURE 6.10: Standard protocol for the XD VTE sequence.

The results obtained for the standard protocol are printed in table 6.2. For an overview of how these quantities were calculated refer to table 5.2.

SNR	70.3 ± 2.3
SNR _{corr}	$46. \pm 1.5$
SNR _{diff}	53.9 ± 2.0
Resolution, ESF [μm]	205.5 ± 1.8
Resolution, LSF [μm]	164 ± 10
Resolution, PSF Y [μm]	203 ± 33
Ringling [%]	115.25 ± 0.76
Diameter [mm]	28.1933 ± 0.0013
Geometric error [%]	0.3494 ± 0.0052

TABLE 6.2: Measurement results for the XD VTE standard protocol.

6.3 Thermal Behavior

This sequence shows rather benign thermal behavior, especially in comparison to the CV UTE sequence, which can cause significant rises in the system temperature.

Within the measurements of this thesis no overheating or fast increase to critical values was observed for this sequence.

Measurements for the thermal behavior of the XD VTE sequence have been performed as described in section 5.5. The results of these measurements are shown in figure 6.11.

For the 13ms measurement additional averages were added to ensure that the system reaches a thermal homeostatic equilibrium.

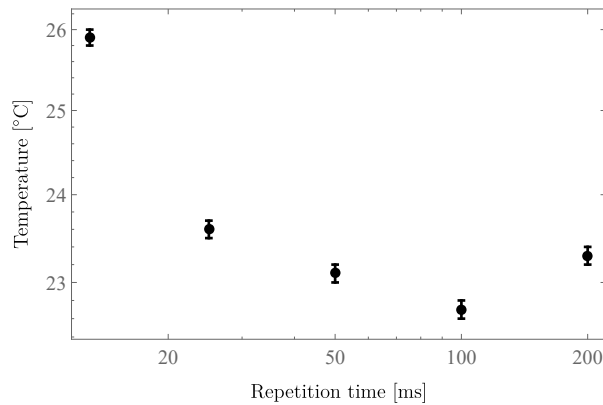


FIGURE 6.11: Thermal behavior of the XD VTE sequence as shown in a log-log plot. Temperature increase at TR 200 can be disregarded as a measurement artefact.

The sequence shows no actual temperature increase during the measurement with a TR of 200ms. This higher temperature is therefore probably caused by a minor fluctuation in the coolant temperature and can therefore be disregarded as an artefact.

6.4 Parameter Variation

Based on the standard sequence a single parameter has been varied each time and the complete analysis has been repeated for each acquisition.

6.4.1 Echo Time

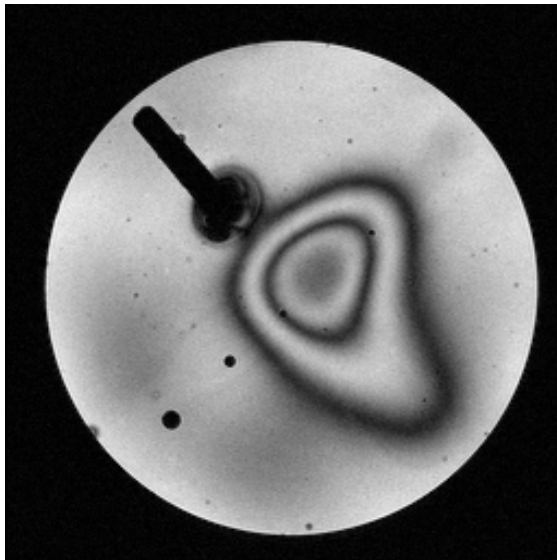
The echo time has been varied. Results of this are printed in table 6.3.

	Standard	TE 1ms	TE 2ms	TE 5ms	TE 10ms
SNR	70.3 ± 2.3	91.7 ± 3.4	98.7 ± 4.6	$72.6 \pm 3.$	44.5 ± 1.2
SNR _{corr}	$46. \pm 1.5$	60.1 ± 2.2	$64.7 \pm 3.$	$47.6 \pm 2.$	29.16 ± 0.75
Resolution [μm]	205.5 ± 1.8	205.6 ± 1.5	$212. \pm 2.9$	$232. \pm 14.$	$308. \pm 41.$
Ringing [%]	115.25 ± 0.76	115.8 ± 1.5	132.7 ± 5.5	171.8 ± 7.6	163.4 ± 7.8

TABLE 6.3: Echo time parameter variation, XD VTE sequence. Pixel size: $125\mu m$

Diameter and geometric error remained equal to the standard sequence within error margins.

It can be observed that the signal to noise ratio is initially improving and decreasing again for echo times above 2ms. The resolution also becomes worse with increasing echo time.



TE	10 ms
TR	200 ms
Avg	3
FOV	(32. x 32.) mm ²
BW	300 $\frac{Hz}{Px}$
Slice	400 μm
α	39°
Matrix	256 x 256
Voxel	(125. x 125. x 400.) μm^3
TA	20:33
Seq	XD VTE

FIGURE 6.12: Signal drop in XD VTE with echo time of 10ms.

At echo times longer than 1ms a significant signal drop can be observed inside the signal intense central area of the phantom, shown in figure 6.12. The probable cause for this phenomenon are inhomogeneities in the B0 field.

This signal drop is also the cause for the increase in the “Ringing” analysis measure. The ringing analysis measure is based on an average of a part of the line profile inside the signal region of this line profile. Due to drop inside this signal region the ringing measure is expected to be slightly overestimated.

6.4.2 Averages

A variation series for different averaging values is presented here.

	Avg 1	Avg 2	Standard 3	Avg 4	Avg 6
SNR	52.8 ± 2.1	$63. \pm 2.2$	70.3 ± 2.3	75.5 ± 2.4	78.2 ± 2.2
SNR _{corr}	34.6 ± 1.4	41.3 ± 1.5	$46. \pm 1.5$	49.4 ± 1.6	51.2 ± 1.4
Resolution [μm]	212.5 ± 2.4	206.4 ± 1.1	205.5 ± 1.8	202.1 ± 1.6	201.7 ± 1.5
Ringing [%]	117.5 ± 0.64	115.5 ± 0.79	115.25 ± 0.76	115.02 ± 0.82	115.02 ± 0.92

TABLE 6.4: Averages parameter variation, XD VTE sequence.

As expected an improvement in signal to noise ratio can be observed.

This measurement also indicates that the resolution is influenced by SNR, a slight improvement of the resolution can be observed with increasing averages and signal to noise ratio.

Even the ringing quantity improves, this could be associated with the fact that the location of the minima and maxima of the Gibbs phenomena are sensitive to small perturbations.

The diameter and geometric error remained constant throughout this series.

6.4.3 Matrix Size

Different matrix sizes were considered and measured. Starting from 128x128 pixels up to 512x512 pixels.

	Matrix 128	Matrix 192	Standard	Matrix 384	Matrix 512
SNR	95.3 ± 1.7	81.8 ± 2.5	70.3 ± 2.3	48.6 ± 1.9	37.1 ± 1.7
SNR _{corr}	62.4 ± 1.2	53.6 ± 1.7	$46. \pm 1.5$	31.8 ± 1.3	24.3 ± 1.1
Resolution [μm]	391.2 ± 1.4	$255. \pm 2.3$	205.5 ± 1.8	150.8 ± 1.8	140.7 ± 2.3
Pixel size [μm]	250.0	166.7	125.0	83.3	62.5
Ringing [%]	111.87 ± 0.97	113.89 ± 0.83	115.25 ± 0.76	119.04 ± 0.83	124.39 ± 0.98

TABLE 6.5: Matrix sizes parameter variation, XD VTE sequence.

With increasing matrix size the signal to noise ratio decreases. This is expected as each voxel becomes smaller and contains less nuclei to be measured.

Resolution also improves with improving matrix size, reaching up to $(140.7 \pm 2.3)\mu m$ for the 512x512 matrix. This compares to $(103.02 \pm 0.8)\mu m$ achieved in the high resolution overnight measurement, section 6.6.

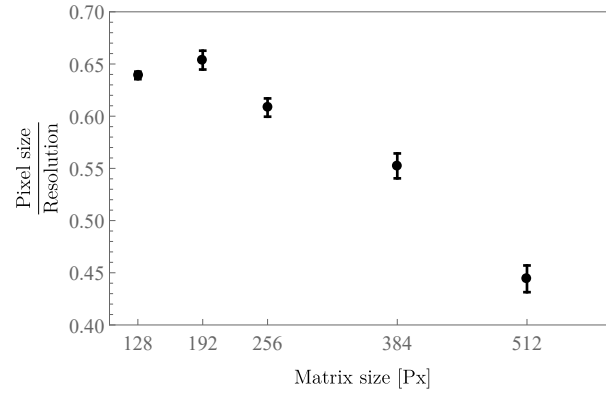


FIGURE 6.13: Comparison between pixel sizes and resolution achieved for the XD VTE sequence. Shows that the actual resolution does not remain constant with pixel size. Meaning that an increase in matrix size still provides an improvement of the actual resolution achieved but doubling the matrix size does not double the actual resolution.

A comparison has also been performed between the pixel size and actual resolution obtained. Figure 6.13 illustrates this comparison. As is visible in this graph there is a reduction of the ratio of pixel size to actual resolution, but absolute resolution is still improved for larger matrices. For the largest matrix size this ratio of pixel size to resolution is only 0.444 ± 0.013 . Meaning that the actual resolution is less than half the nominal resolution.

With increasing matrix sizes the ringing also increases in amplitude and frequency. This might be explained by an increase of the variable echo time difference as k-space size increases. A full explanation of the effect of the variable echo time on the ringing artefact is provided later on in section 6.5.1.

For brevity the diameter and geometric error have been omitted in table 6.5. The geometric error improves with larger matrix sizes, as the circle is actually sampled better, and reaches $(0.2584 \pm 0.0071)\%$ for the 512x512 matrix. Figure 6.15 shows the standard protocol with this matrix size.

Increasing the matrix size also has an effect on the minimum TE possible. For an increase to 384x384 the minimum TE becomes 0.77ms, for 512x512 the TE becomes even longer with 0.87ms. This would indicate that the TE set in the sequence is not the minimum TE at center k-space but rather the TE at the outside edges of k space. In this context the increase in the lower limit of the TE setting would make sense.

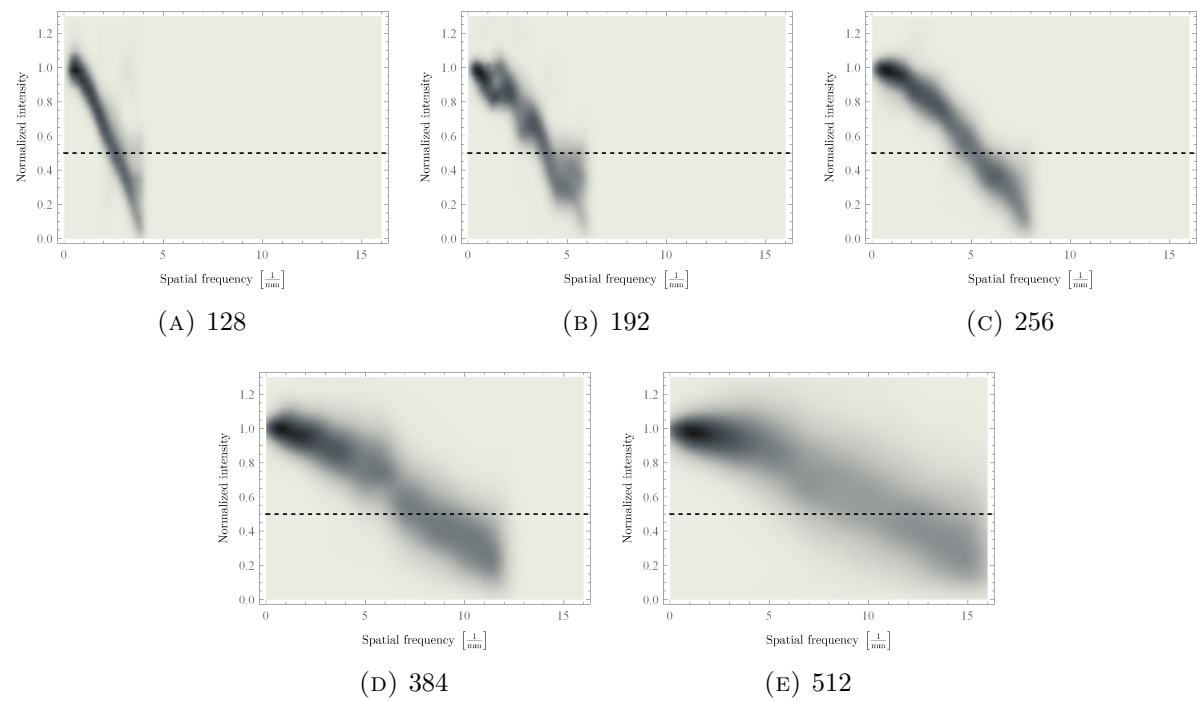


FIGURE 6.14: MTF for different matrix sizes in the XD VTE parameter variation. Rendered using Mathematicas SmoothDensityHistogram function, using identical axes ranges for easier comparison. Each plot contains 304 modulation transfer functions.

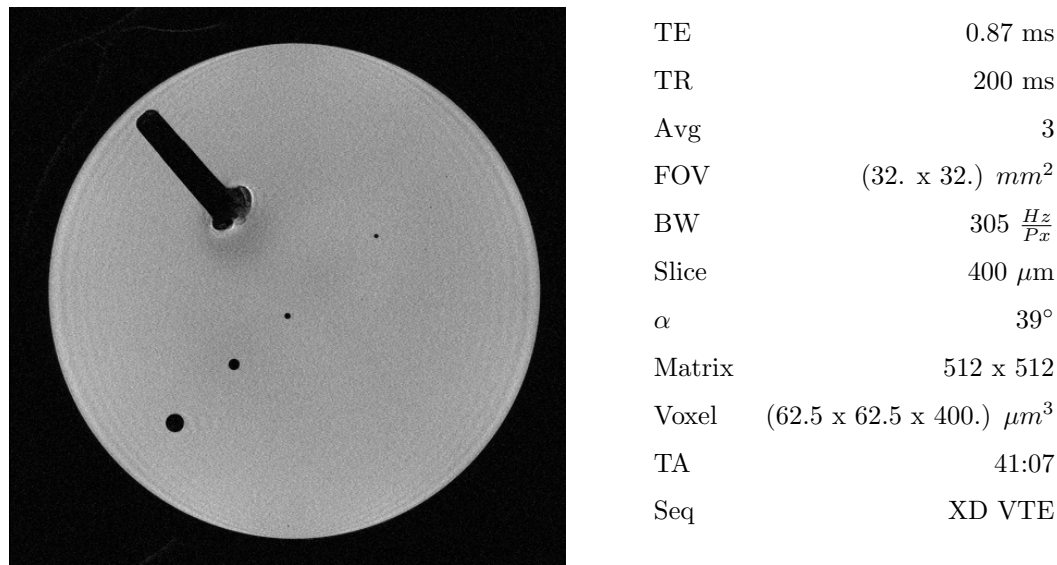


FIGURE 6.15: Standard protocol with 512x512 matrix, XD VTE sequence.

6.4.4 Bandwidth

In this measurement series the bandwidth has been varied.

The results of this series are shown in table 6.6.

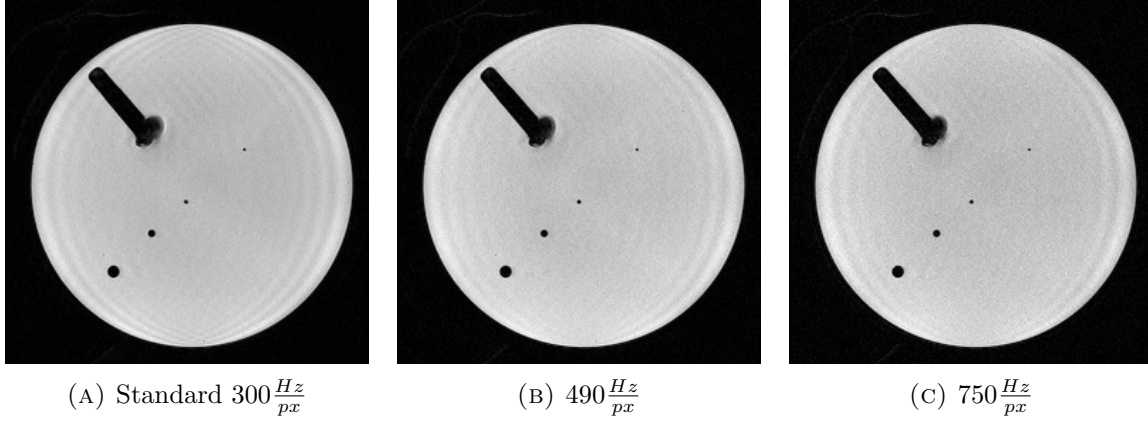


FIGURE 6.16: Comparison of different bandwidth settings for the XD VTE sequence.

	Standard $300 \frac{\text{Hz}}{\text{px}}$	$490 \frac{\text{Hz}}{\text{px}}$	$750 \frac{\text{Hz}}{\text{px}}$
SNR	70.3 ± 2.3	60.6 ± 2.1	54.1 ± 2.2
SNR _{corr}	$46. \pm 1.5$	39.7 ± 1.4	35.4 ± 1.5
Resolution [μm]	205.5 ± 1.8	205.4 ± 1.5	204.2 ± 1.7
Ringings [%]	115.25 ± 0.76	116.46 ± 0.86	120.36 ± 0.79
Diameter [mm]	28.1933 ± 0.0013	28.2039 ± 0.0013	28.2015 ± 0.0018
Geometric error [%]	0.3494 ± 0.0052	0.36797 ± 0.00076	0.3653 ± 0.0036

TABLE 6.6: Bandwidth parameter variation, XD VTE sequence.

It can be observed that with increasing bandwidth the signal to noise ratio becomes worse. This can be explained by increased noise due to the increased bandwidth. Assuming a white noise source it becomes clear that increasing the bandwidth increases the amount of noise being picked up.

Ringings also increases, also explained by stronger gradients and therefore stronger edge enhancement artefacts.

6.4.5 Filters

This section contains an analysis of all filters found in the “Resolution/Filters” tab of the sequence.

The sequence provides a wide variety of filters. These are poorly documented and the effect on the final image is not always very clear.

In order to evaluate the different filter options a full parameter variation has been performed for all filters. The results of these extensive measurements are shown in table 6.7.

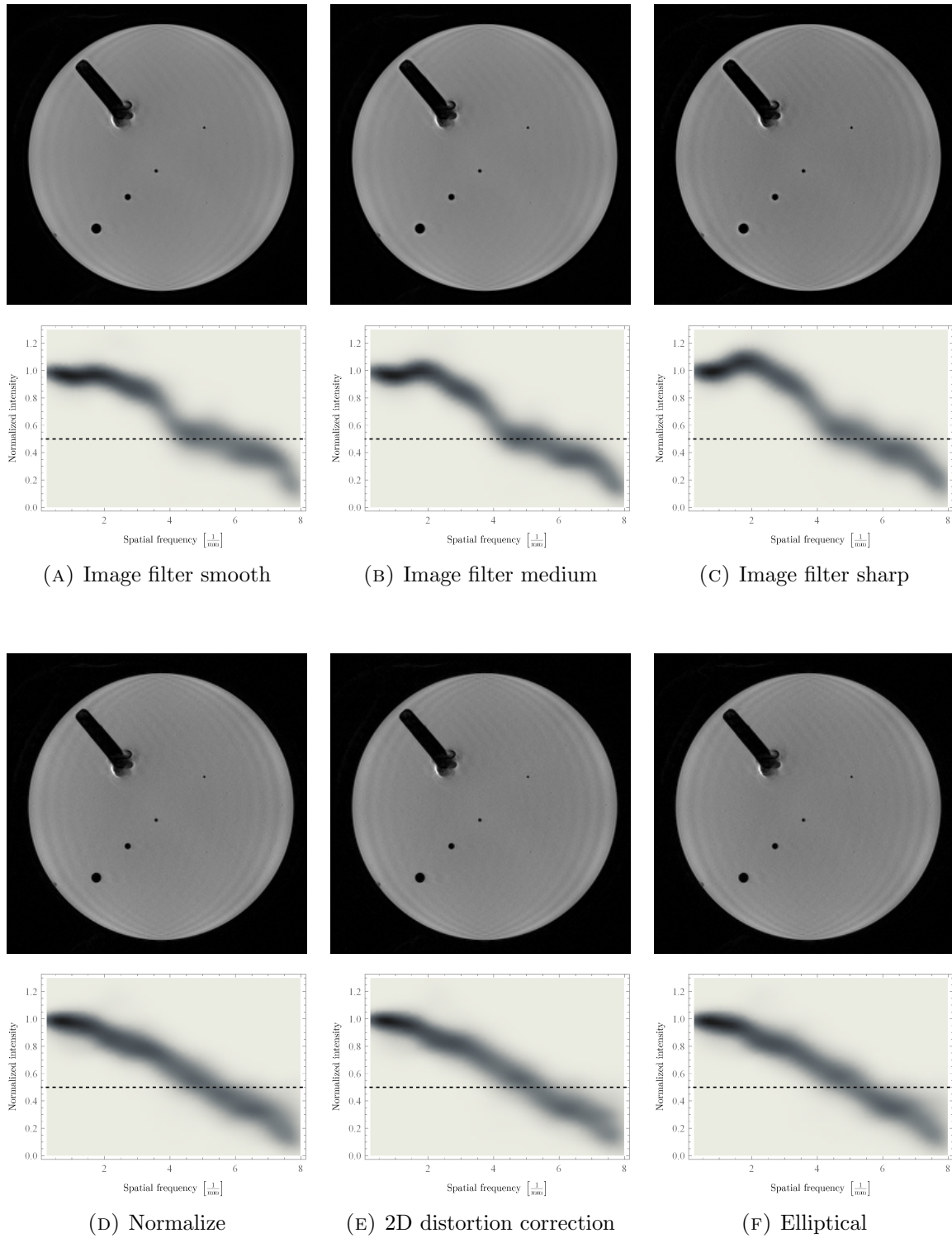


FIGURE 6.17: Comparison of different filter settings and their effects on the modulation transfer functions based on the edge spread functions.

Parameter	SNR	SNR _{corr}	Resolution [μm]	Ringing [%]	Diameter [mm]	Geometric error [%]
Standard	70.3 \pm 2.3	46. \pm 1.5	205.5 \pm 1.8	115.25 \pm 0.76	28.1933 \pm 0.0013	0.3494 \pm 0.0052
Image Filter Medium Edge=3, Smoothing=3	97.2 \pm 3.3	63.7 \pm 2.2	214.9 \pm 3.2	114.32 \pm 0.76	28.1826 \pm 0.0025	0.3407 \pm 0.0087
Image Filter Sharp Edge=5, Smoothing=5	78. \pm 2.8	51.1 \pm 1.8	198.7 \pm 3.7	115.73 \pm 0.84	28.1875 \pm 0.0028	0.3409 \pm 0.0087
Image Filter Smooth Edge=1, Smoothing=1	96.8 \pm 3.5	63.4 \pm 2.3	208.6 \pm 3.	114.09 \pm 0.73	28.1842 \pm 0.0018	0.3295 \pm 0.0064
Distortion Corr. 2D	78.9 \pm 2.5	51.7 \pm 1.7	204. \pm 1.3	115.62 \pm 0.7	28.1678 \pm 0.0025	0.3336 \pm 0.009
Distortion Corr. 3D	70.9 \pm 2.4	46.4 \pm 1.6	203.9 \pm 1.9	116.52 \pm 0.8	28.1883 \pm 0.0025	0.3491 \pm 0.008
Normalize Medium Cut- Off=20, Width=4	76.4 \pm 2.4	50. \pm 1.6	204.2 \pm 1.9	117.13 \pm 0.81	28.1793 \pm 0.0025	0.3238 \pm 0.0066
B1 Filter Medium	66.5 \pm 2.6	43.6 \pm 1.7	204.3 \pm 2.4	109.62 \pm 0.66	28.1834 \pm 0.002	0.3373 \pm 0.0075
Raw Filter	71.55 \pm 0.79	46.87 \pm 0.52	199.8 \pm 1.1	109.57 \pm 0.78	28.1702 \pm 0.0066	0.3467 \pm 0.0074
Elliptical Filter	72.4 \pm 2.4	47.4 \pm 1.6	203.2 \pm 1.3	116.5 \pm 0.83	28.1859 \pm 0.0025	0.3373 \pm 0.0075

TABLE 6.7: Parameter variation for the Resolution/Filters in the XD VTE sequence.

The image filter can lead to an improvement of the signal to noise ratio, depending in its settings. In these measurements the setting medium with edge=3 and smoothing=3 yielded the highest SNR improvement. The result of this filter is shown in figure 6.17b.

This filter also caused a slight drop in the resolution. This drop is significant as it exceeds the error margins between these two measurements. But is still only a drop by about 4 %.

In the smooth setting the SNR improvement is also there, and equal within error margin to the medium setting, but the resolution remains equal to the standard protocol, within confidence.

The 2D distortion correction also provided a slight boost in SNR, without any adverse effects.

3D distortion correction leads to a slight increase in mean ringing, but this remains within error margins.

With the normalize filter in setting medium, cut off 20 and width 4 a slight improvement in SNR is possible, while this also leads to a slight increase in ringing, significant with respect to the estimated errors.

Both the B1 filter, at its medium setting, and the raw filter lead to a slight decrease in ringing with a difference to the standard sequence of about 6%.

With the already very good geometric accuracy no significant change in diameter or geometric error could be observed with any of the filters.

6.4.5.1 Recommendations

If an improvement in signal to noise ratio is useful for the measurement, and post processing is to be avoided, several filters can be used to achieve this goal. The most promising option would be to use the image filter in its smooth setting with edge 1 and smoothing 1.

In cases where ringing is a problematic issue, the B1 filter in its medium setting or the raw filter could be used.

6.4.6 Other Settings

The effect of a multitude of other settings has also been investigated by parameter variation.

Results of these variations are provided in table 6.8.

Some effects could be observed for these other settings.

Parameter	SNR	SNR _{corr}	Resolution [μm]	Ringing [%]	Diameter [mm]	Geometric error [%]
Standard	70.3 \pm 2.3	46. \pm 1.5	205.5 \pm 1.8	115.25 \pm 0.76	28.1933 \pm 0.0013	0.3494 \pm 0.0052
Contrast/Common						
MTC	82.5 \pm 3.5	54. \pm 2.3	205.3 \pm 1.6	120.5 \pm 1.7	28.1883 \pm 0.0022	0.3493 \pm 0.0082
Contrast/Dynamic						
Averaging Mode Long Term	70.8 \pm 2.4	46.4 \pm 1.6	202.9 \pm 2.	115.65 \pm 0.75	28.1867 \pm 0.0028	0.357 \pm 0.0055
Reconstruction Magn/Phase	70.7 \pm 2.2	46.3 \pm 1.5	203.24 \pm 0.85	115.43 \pm 0.79	28.1891 \pm 0.0039	0.351 \pm 0.011
Resolution/Common						
Phase Partial Fourier 6/8	87.2 \pm 2.7	57.1 \pm 1.8	202.9 \pm 2.1	115.44 \pm 0.94	28.1875 \pm 0.0018	0.3381 \pm 0.0045
Slice Partial Fourier 6/8	74.1 \pm 2.4	48.5 \pm 1.6	202.8 \pm 1.3	115.24 \pm 0.8	28.1883 \pm 0.0028	0.3527 \pm 0.0084
Interpolation ON	74.5 \pm 2.3	48.8 \pm 1.5	138. \pm 2.9	114.43 \pm 0.81	28.2405 \pm 0.00042	0.2604 \pm 0.0019
System/Adjustments						
Assume Silicone	70.8 \pm 2.5	46.4 \pm 1.7	269.1 \pm 4.9	114.56 \pm 0.97	28.1974 \pm 0.0018	0.2781 \pm 0.0055
Inline/Composing						
Distortion Correction 2D	78.2 \pm 2.3	51.2 \pm 1.6	207.1 \pm 1.5	115.78 \pm 0.85	28.1694 \pm 0.0041	0.3213 \pm 0.0059
Distortion Correction 3D	70. \pm 2.4	45.8 \pm 1.6	203.8 \pm 1.3	115.09 \pm 0.84	28.1883 \pm 0.0025	0.3453 \pm 0.0072

Parameter	SNR	SNR _{corr}	Resolution [μm]	Ringings [%]	Diameter [mm]	Geometric error [%]
Sequence/Part1						
Elliptical Scanning	73.8 ± 2.4	48.3 ± 1.6	204.4 ± 1.4	114.92 ± 0.7	28.1875 ± 0.0022	0.3493 ± 0.0081
Phase Stabilization ON	$70. \pm 2.5$	45.9 ± 1.7	315.3 ± 2.9	116.61 ± 0.5	28.1891 ± 0.0037	0.3439 ± 0.0094
Multi Slice Mode Sequential	67.8 ± 2.3	44.4 ± 1.5	206.2 ± 1.3	113.15 ± 0.47	28.2056 ± 0.0039	0.349 ± 0.011
Asymmetric Echo OFF	$70. \pm 2.5$	45.9 ± 1.7	315.3 ± 2.9	116.61 ± 0.5	28.1891 ± 0.0037	0.3439 ± 0.0094
Allowed Delay 2s	$70. \pm 2.5$	45.9 ± 1.7	315.3 ± 2.9	116.61 ± 0.5	28.1891 ± 0.0037	0.3439 ± 0.0094

TABLE 6.8: Parameter variation of other settings in the XD VTE sequence.

Turning on the magnetization transfer contrast, MTC, in the contrast/common tab improves the signal to noise ratio and also increases the ringing artefact slightly. Usually a drop in signal intensity would be expected in this scenario. [42]

Setting phase partial Fourier 6/8 in the resolution/common tab leads to an increase in SNR. This is the opposite of what would be expected behavior.

The mean SNR also increases for slice partial Fourier 6/8 but this increase is not significant, within error margins.

Only 6/8, 7/8 and “off” partial Fourier settings are available. The 7/8 partial Fourier setting was not evaluated in the course of this thesis.

Both phase partial Fourier and slice partial Fourier reduce the TA to 15min 22sec.

An option “assume silicone” is available in the system adjustments tab. Which effect it has on the sequence execution remains unclear so far. It causes a reduced resolution when set to “on”. This option is intended for using a silicone oil phantom to tune up the sequence and perform subsequent measurements on water containing samples. Therefore a frequency shift is expected when not using a dedicated phantom and the phantom used in this is itself made of silicone.

Distortion correction is also available in the inline/composing tab. While setting the 2D correction to “on” causes a slight improvement in SNR, similar to the 2D correction filter, the 3D correction doesn’t seem to have any effect.

Sequence/part1 offers some more possibilities. In this tab the phase stabilization, asymmetric echo off and allowed delay to 2s all cause the resolution to become extensively worse. In elliptical scanning the SNR improves slightly, but not with significance. Multi slice mode sequential causes a non significant drop in mean SNR.

Elliptical scanning could be interesting because it also shortens the TA time to 15min 19sec, while slightly improving SNR in this scenario.

Asymmetric echo off causes the minimum TE to increase to 2.11ms while providing no measurable benefit.

Interpolation in the resolution/common tab creates a 512x512 matrix based on the 256x256 measurement. This improves SNR, but not up to significance. The resolution is improved significantly by this setting.

6.4.7 Settings Which Cause Execution Errors

Setting the rf pulse to normal causes the sequence run to fail.

6.5 Artefacts

6.5.1 Ringing

A quite notable ringing artefact (section 3.1) is visible, with overshoot values of $(115.25 \pm 0.76)\%$ in the standard protocol. For details how this value is defined see section 2.5.

Some periodicity, as would be expected with Gibbs ringing, can be seen in the line profile, figure 6.18a.

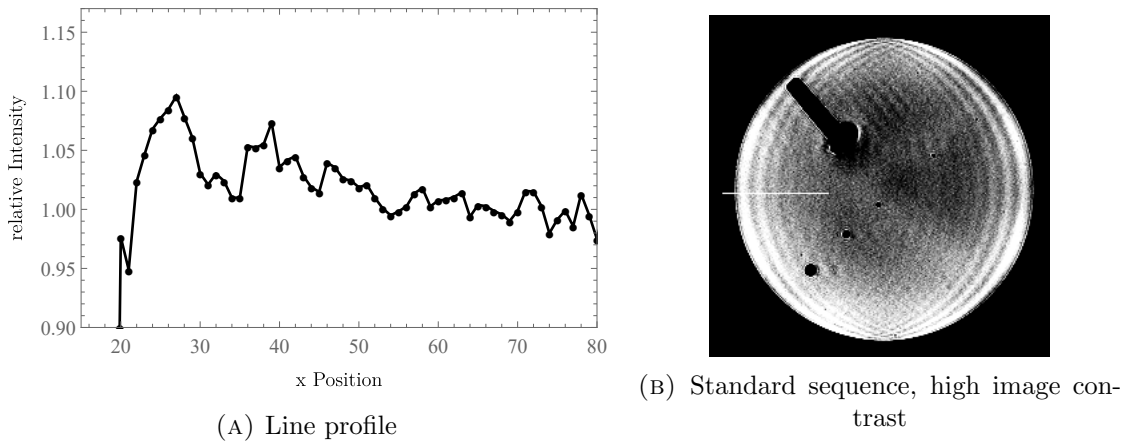


FIGURE 6.18: Ringing artefact in the XD VTE sequence. The sequence image has been enhanced by increasing the contrast in the brightness range of the ringing. The white line at the 9 o'clock position shows the source of the line profile. X position shown is in pixels and not length units. Pixel size is $125\mu m$ for this image.

These can be seen for example in figures 6.10 and 6.23.

This ringing artefact might be explained by a combination of edge enhancement and the variable echo time as shown in the sequence diagram at the start of this chapter in figure 7.1. According to this diagram the echo time remains constant for a certain part of k-space and is then increased. This increase also only happens in two spatial directions. While the y direction is most significant for explaining the appearance of this artefact in only one direction in the resulting images. The contribution of the variable echo time to this artefact is not necessarily very prominent, this still remains open to investigation.

6.5.1.1 K Space Distortion Simulation

In order to provide more evidence for the hypothesis that the variable TE contributes to this artefact a special case of k-space distortion a computer simulation has been developed.

A weighting function, equation 6.1, has been written to simulate the effect that the reduced echo time has on k-space sampling.

$$w(x) = \begin{cases} 1 & \text{if } x \leq x_0 \\ e^{-(x-x_0)/b} & \text{if } x > x_0 \end{cases} \quad (6.1)$$

This simulation has been run at a matrix size of 256×256 pixels, x_0 has been set to 35 pixels, b was set to 10, this produces weighting factors as shown in figure 6.19c. These parameters were chosen empirically based on the similarity of the output with the measurements.

A uniform disk with a radius of 220 pixels has been used as the input image to the simulation, figure 6.20a.

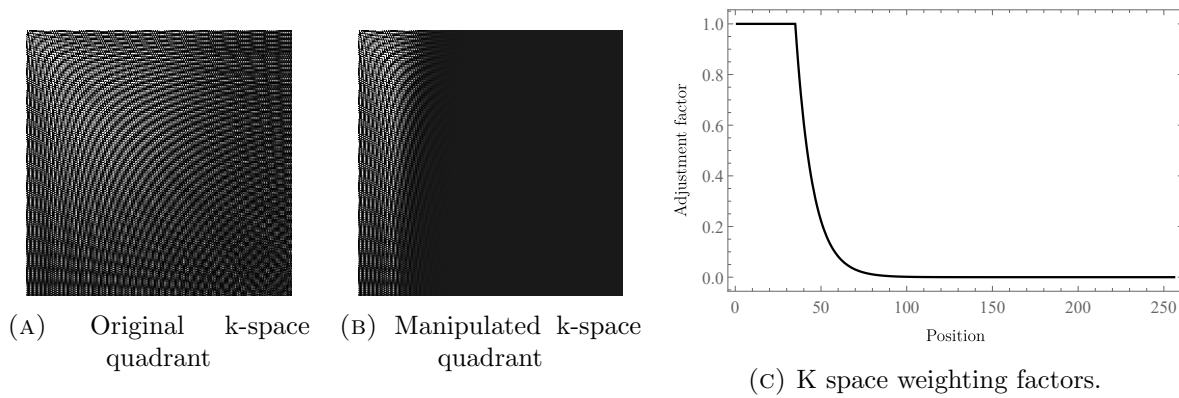


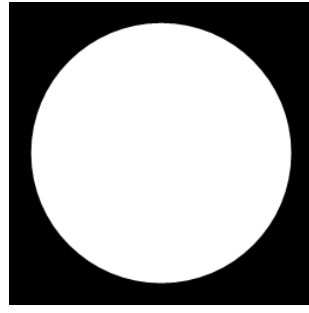
FIGURE 6.19: Original and manipulated k-space quadrant of the simulation and k-space weighting factors. The central frequency is in the top left corner of the k-space images. Positions are in pixels, the adjustment factor is dimensionless.

This function simulates a constant echo time with therefore constant signal in the center of k-space. According to the sequence diagram in figure 7.1, the change in echo time, after this initial constant echo time, is linear with respect to k-space coordinates. As this longer echo time results in a further exponential decay due to T_2^* the part after the cut off has been simulated using an exponential decay.

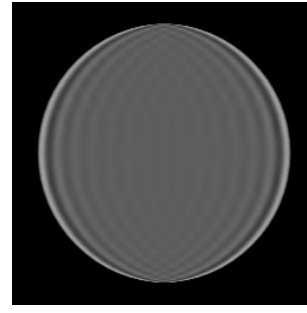
The transformation from and to frequency space has been realized using a discrete Fourier sine transform, type DM-I. This allowed easiest manipulation of the Fourier coefficients.

As can be seen from the simulation result, figure 6.20b, and the images of the XD VTE standard protocol a strong similarity exists between these artefacts. This strengthens the argument that the variable TE based k space attenuation might contribute to the ringing artefact.

A direct comparison between the simulation result and the measurement of the XD VTE standard protocol is provided in figure 6.22.



(A) Input



(B) Simulation result, contrast adjusted.

FIGURE 6.20: Simulation of the k-space distortion due to variable echo time in the XD VTE sequence.

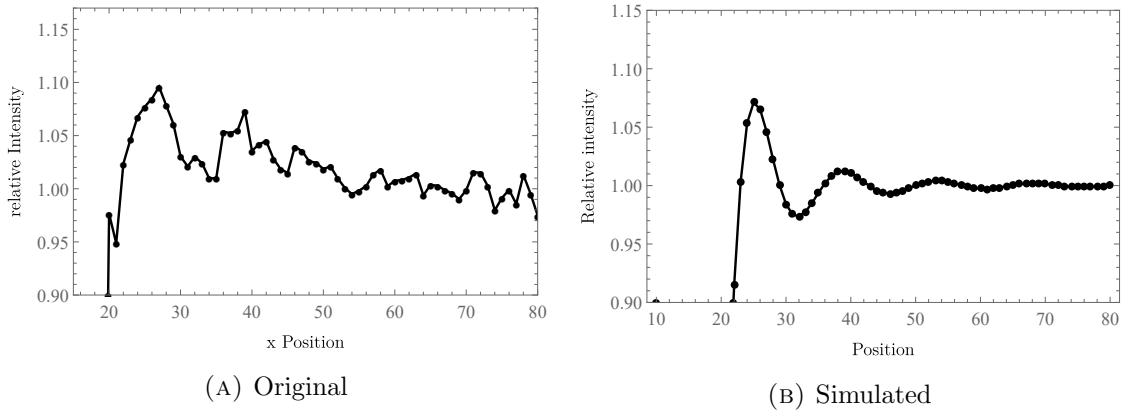


FIGURE 6.21: Comparison of the shapes between the line profiles of the simulation result and the line profile found in the XD VTE standard protocol image.

Comparing the k-space cut off to the resolution limit achieved in the actual measurement, shows that the standard protocol resolution of $(204.8 \pm 0.2)\mu m$ is somewhat better than would be expected from k-space cut off which happens at about $1.875 \frac{1}{mm}$ which would correspond to a resolution of $533.33\mu m$. The b factor, which controls how fast the exponential function approaches zero, has been chosen based on the shape and amplitude of the line profile.

So far this can only be viewed as a preliminary investigation but it provides valuable clues into some of the reasons for reduced resolution and the special ringing phenomena observed in the XD VTE sequence.

Another open question which remains is that based on the proposed explanation of reduced signal due to prolonged echo time for the outer parts of k-space a signal drop would be expected but by far not down to no signal at all, considering the $T2^*$ times of the phantom of $(11.6 \pm 1.1)ms$ and the TE of 0.67 ms. Therefore a far bigger b factor would be expected in the simulation but this doesn't agree well with the line profile comparison and visual comparison of the results. Therefore it becomes clear that these fit parameters are not realistic and this mechanism is probably not causing this artefact on its own, this effect might still provide a contribution to

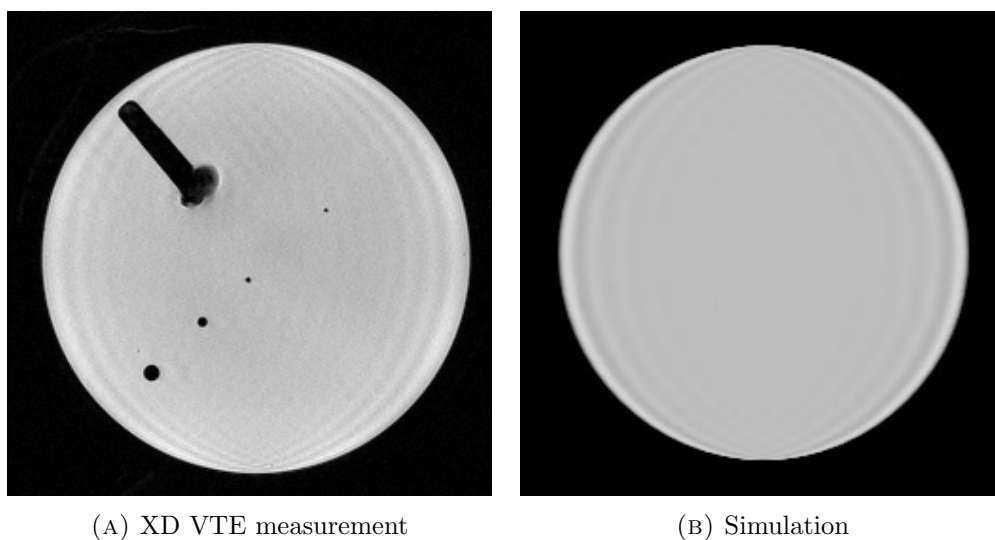
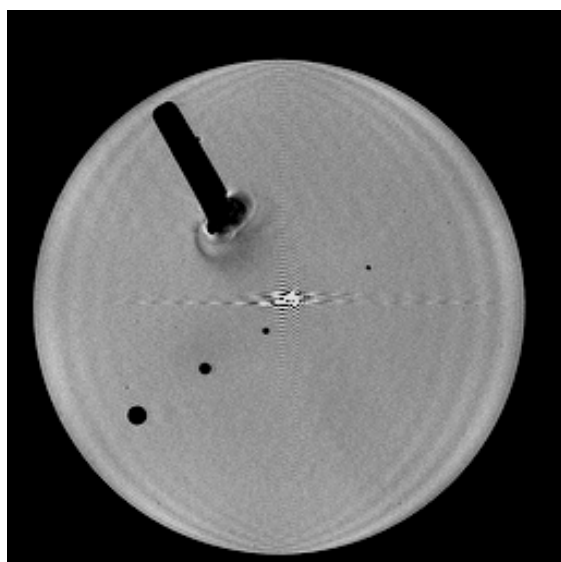


FIGURE 6.22: Comparison of the unadjusted simulation with the actual XD VTE standard protocol measurement.

the overall effect and can lead to an image which has a similar appearance to the one observed in the actual measurements.

6.5.2 Zero Point Artefact

The XD VTE sequence has a very prominent zero point artefact. This is shown in figure 6.23. The cause of this artefact is explained in section 3.4.



TE	0.67 ms
TR	200 ms
Avg	3
FOV	(32. x 32.) mm^2
BW	300 $\frac{Hz}{Px}$
Slice	400 μm
α	31°
Matrix	256 x 256
Voxel	(125. x 125. x 400.) μm^3
TA	20:33
Seq	XD VTE

FIGURE 6.23: Zero point artefact in the XD VTE sequence. This image does not contain the full dynamic range.

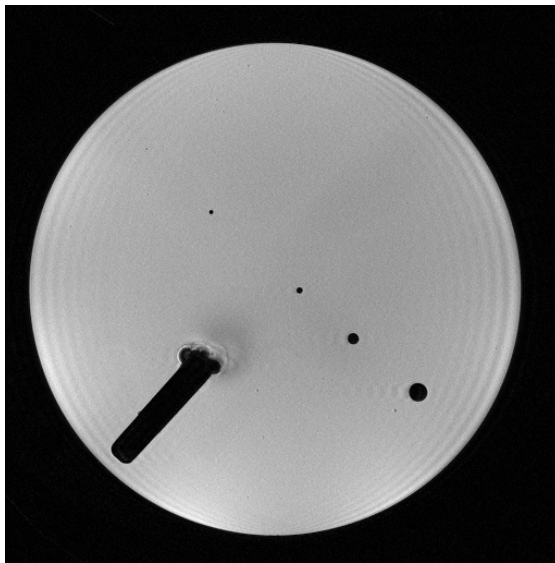
Lines or side lobes are visible in both directions.

The highest value inside the artefact reaches the clipping value of 4095.

6.6 High Resolution

A high resolution overnight measurement was performed to test the capabilities of the sequence at its limits.

As for the standard protocol the flip angle was based upon an erroneous initial fit of T1 and is therefore not optimal but the same T1 time has been used for all standard protocols and their parameter variations to calculate flip angles throughout this thesis in order to obtain consistent results.



TE	0.75 ms
TR	2600 ms
Avg	4
FOV	(32. x 32.) mm ²
BW	488 $\frac{Hz}{Px}$
Slice	400. μm
α	61°
Matrix	512 x 512
Voxel	(62.5 x 62.5 x 400.) μm^3
TA	11:52:46
Seq	XD VTE

FIGURE 6.24: Overnight high resolution measurement, XD VTE sequence.

The analysis was performed using the Mathematica Analysis Toolkit, which was also used for the other sequences and images.

6.6.1 Signal to Noise Ratio

Signal to noise ratio was measured for all 8 slices and in the regions of interest shown in figure 6.25.

The signal to noise ratios for all the slices are $\frac{2151.6}{33.6}$, $\frac{2083.5}{33.3}$, $\frac{2009.2}{33.1}$, $\frac{1975.6}{32.7}$, $\frac{2004}{32.7}$, $\frac{2074.5}{33.2}$, $\frac{2144.6}{33.7}$, $\frac{2176.1}{33.9}$ which gives a mean signal to noise ratio of 62.42 ± 0.54 and 40.88 ± 0.35 after applying the correction.

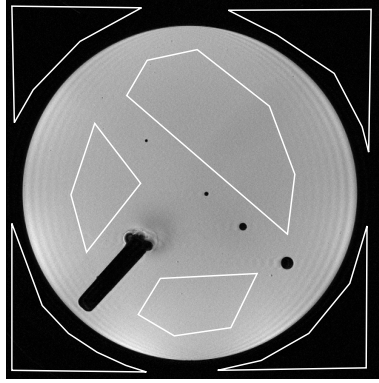


FIGURE 6.25: Regions of interest used for the SNR analysis in the high resolution overnight XD VTE measurement.

6.6.2 Resolution using ESF and MTF

The resolution was analyzed using the edge spread function to modulation transfer function methodology. The overnight high resolution measurement using the XD VTE sequence has a resolution of $(103.02 \pm 0.8) \mu m$. In comparison the standard protocol has a (205.5 ± 1.8) resolution with a 256 pixel matrix and $(140.7 \pm 2.3) \mu m$ with 512 pixels.

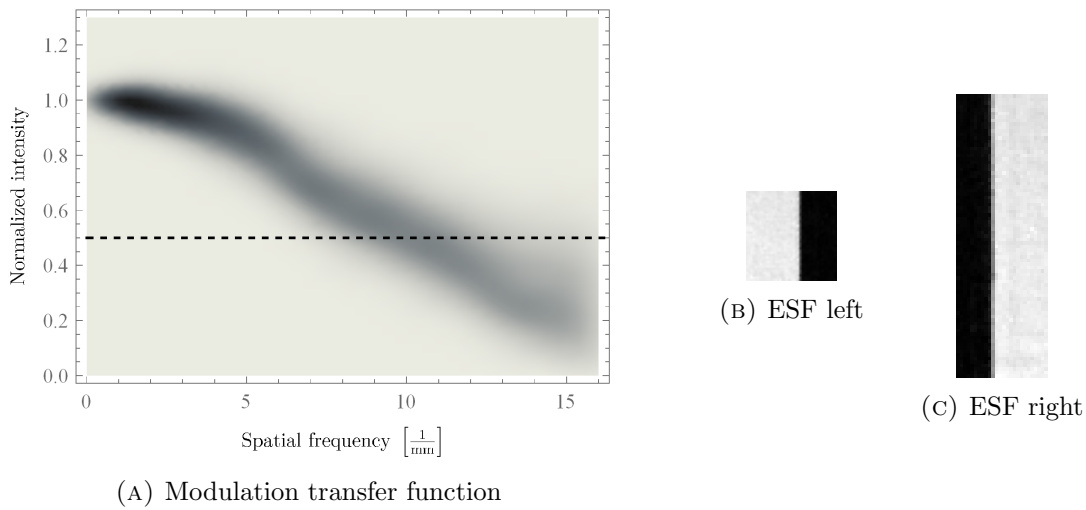


FIGURE 6.26: Modulation transfer function and the edge spread functions upon which this MTF is based for the XD VTE high resolution overnight measurement.

The edge spread functions and the modulation transfer function are shown in figure 6.26. The left ESF on the left side was chosen in a narrower region because of a small artefact which was visible in the center of this part and therefore only the top section was used.

An attempt was also made to determine the resolution using Gaussian fits on the smallest PSF structure of $(60.8 \pm 0.2) \mu m$. This object was not sufficiently well resolved in the line profiles to obtain a good fit from it. This object is somewhat visible (figure 6.27), but does not provide more contrast than surrounding noise and possibly air bubbles.

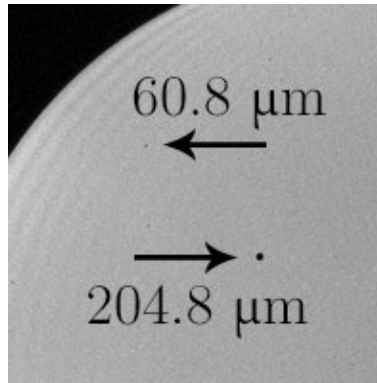


FIGURE 6.27: Cut out of the left upper quadrant of the XD VTE high resolution, overnight measurement, figure 6.24. Showing the two smallest PSF phantom structures and their diameters, estimated error of these diameters is $0.2\mu m$.

6.6.3 Results

The results for the overnight measurement are shown in table 6.9. A comparison to the standard protocol is also provided in this table.

	Standard 256 Matrix	Standard 512 Matrix	High resolution overnight
SNR	70.3 ± 2.3	37.1 ± 1.7	62.42 ± 0.54
SNR_{corr}	$46. \pm 1.5$	24.3 ± 1.1	40.88 ± 0.35
Resolution [μm]	205.5 ± 1.8	140.7 ± 2.3	103.02 ± 0.8
Pixel size [μm]	125.0	62.5	62.5
Ringing [%]	115.25 ± 0.76	124.39 ± 0.98	125.6 ± 0.42
Diameter [mm]	28.1933 ± 0.0013	28.2693 ± 0.0017	28.1928 ± 0.0034
Geometric error [%]	0.3494 ± 0.0052	0.2584 ± 0.0071	0.1015 ± 0.0056
TA	20:33	41:07	11:52:46

TABLE 6.9: Results for the XD VTE overnight high resolution measurement and comparison to the standard protocol.

It should be noted that the resolution of this overnight protocol of $(103.02 \pm 0.8)\mu m$ is the best one achieved throughout this thesis. The SNR is, as expected, also better than for the standard protocol at a 512 matrix size.

6.7 Slice Thickness

The slice thickness has been determined as described in section 2.7.

For the length measurement an error of $\pm 50\mu m$ has been estimated. Linear interpolation was applied between the pixels to find the FWHM. The pixel size for this measurement was $62.5\mu m$. A sub pixel estimation of this parameter seems reasonable in this case.

The slice thickness has been calculated, based on the line profile shown in figure 6.29. The result of this calculation is a slice thickness of $(167 \pm 67)\mu m$ which is well within the limits of the nominal slice thickness of $126\mu m$ for this measurement, figure 6.28.

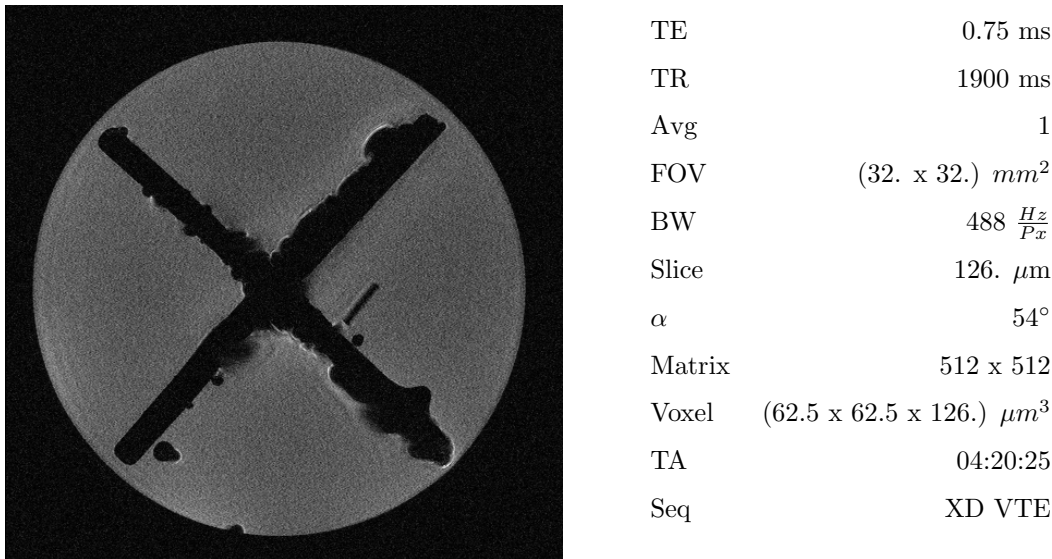


FIGURE 6.28: Slice for the thickness measurement of the XD VTE sequence.

The line profile used for this analysis is shown in figure 6.29.

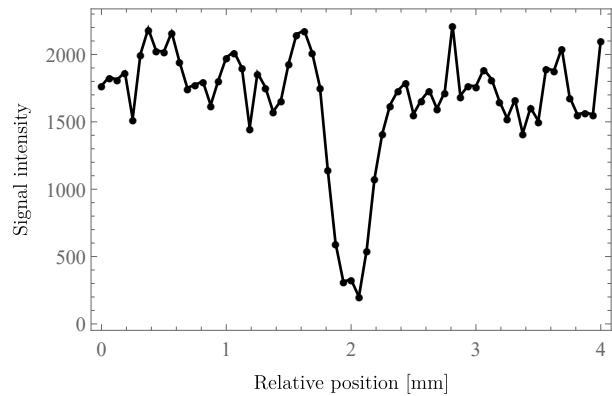


FIGURE 6.29: Line profile for the calculation of the slice thickness in the XD VTE sequence.

CV UTE

7.1 Sequence

This sequence is a “work in progress” (WIP) package from Siemens.

The following information was obtained from the documentation of the package: “This WIP package provides modified sequence executable with TrueFISP and GRE contrasts and Ultra-Short Echo Time (UTE) imaging.”[11]

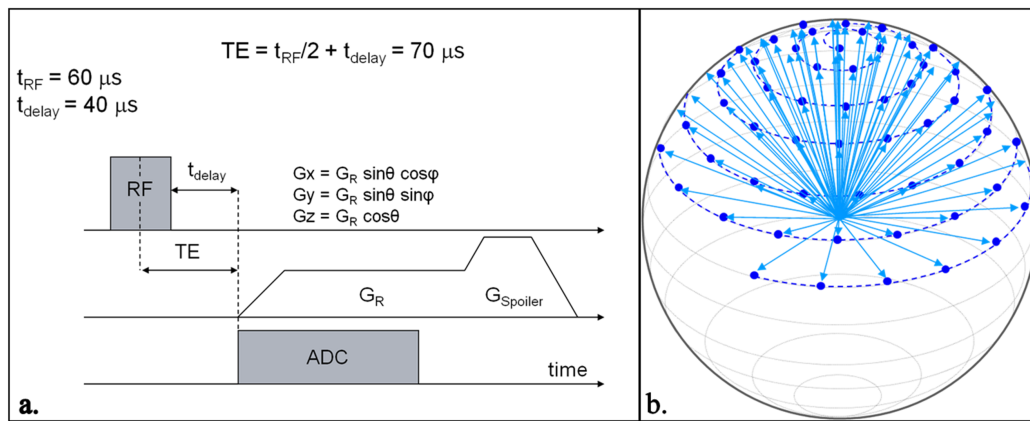


FIGURE 7.1: Sequence diagram and illustration of the k-space trajectory as provided in the CV UTE documentation.[11] This image was published by Chan, C.[12], no source is provided in the documentation and the image as shown and published by Chan, C. is available under open access and a permissive licence and was therefore used instead.

Image source: Chan, C.[12], published under a CC BY 2.0 licence.

According to the documentation the sequence has the following properties: CV UTE uses 3D radial sampling with a spiral path, from the center of a sphere to its surface. It provides echo times below 1 ms and uses a non selective (no slice selection) $60\mu s$ rf pulse. After this excitation a waiting time of $40\mu s$ is kept, this is in order to allow time for the switch from transmit to receive mode.[11]

As also discussed in the UTE sample sequence in section 1.2 signal acquisition starts immediately with gradient ramp up.

Minimum TE for this sequence, as configurable in the systems console, is 0.07ms.

It should be noted that objects should be close to the isocenter, because the sequence allows to move the FOV but this only happens in post processing and will therefore reduce image quality.[11]

7.2 Standard Protocol

A standard protocol has also been designed for the CV UTE sequence, using the goals described in section 5.3. Defined in table 7.1.

Parameter	Value	Parameter	Value
TA	21 min 40 sec	BW	$300 \frac{Hz}{px}$
TE	0.67 ms	Avg	2
TR	200 ms	Segments	4
α	39°	Filters	none
FOV	(32 mm x 32 mm)		
Base	256x256		
Radial	13000		

TABLE 7.1: CV UTE standard protocol.

The base in table 7.1 sets the matrix size of the regridding matrix.

This sequence breaks down the acquisition area into segments and thereby the acquisition time, which would be expected due to the other settings, is divided by the number of segments. The minimum amount of segments which can be set is “4”, a setting of “8” has also been evaluated during parameter variation as described later.

7.2.1 Signal to Noise Ratio using ROIs

The signal to noise ratio was obtained as described in section 2.3.

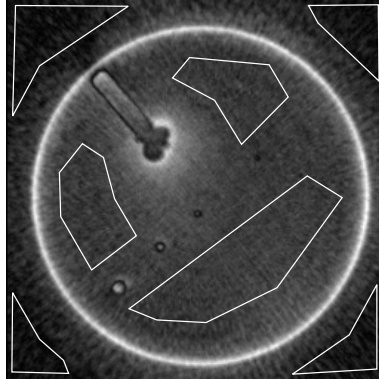


FIGURE 7.2: Regions of interest used for the SNR analysis in the CV UTE sequence.

Regions of interest used are depicted in figure 7.2.

The signal to noise analysis is based upon the signal and noise ratios of 13 slices. For all of the 13 signal to noise ratios of $\frac{207.}{35.3}, \frac{206.1}{35.7}, \frac{205.2}{36.}, \frac{204.9}{37.5}, \frac{205.2}{39.3}, \frac{208.}{38.1}, \frac{207.8}{36.1}, \frac{205.1}{35.9}, \frac{203.}{36.5}, \frac{201.7}{35.4}, \frac{201.2}{37.2}, \frac{200.5}{37.7}, \frac{199.8}{37.2}, \frac{200.4}{36.9}$.

Calculating the mean of all these results gives us a **total signal to noise ratio of 5.553 ± 0.053 and a corrected SNR of 3.637 ± 0.035 .**

7.2.2 Signal to Noise Ratio using Difference Images

Using the difference image method, described in section 2.3.3 and in the NEMA standards[4], a second analysis of the SNR has been performed.

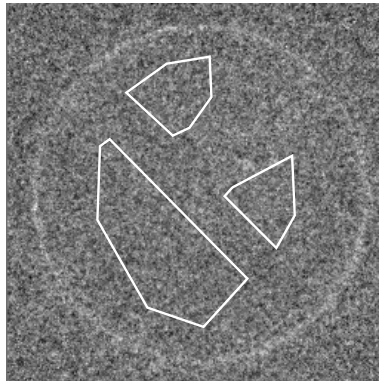


FIGURE 7.3: Difference image of two successive slices used for SNR calculation.

The resulting signal to noise ratio using difference images, SNR_{diff} , is 23.952 ± 0.088 .

There is a quite large difference between these two methods of obtaining the signal to noise ratio. The difference in the results might be caused by the strong artefacts present in those

images, and the different impact that these artefacts have on the noise measurement. In the ROI method some of the artefacts are added to the noise while this effect is mostly avoided in the difference images method.

7.2.3 Resolution

7.2.3.1 Edge Spread Function

Due to the extreme artefacts in these measurements, acquired with this sequence, a proper analysis of the resolution was not possible. These edge enhancement artefacts are most likely caused by k-space trajectory errors, caused by gradient delays which are not properly compensated for during reconstruction. This artefact and possible remedies will be discussed in more detail later on in section 7.6.1.

Resolution data is still provided based upon the ESF-MTF analysis method. This data should not be considered correct for comparison to the other sequences and might provide some insights into different settings of the CV UTE sequence itself, but even this remains highly doubtful.

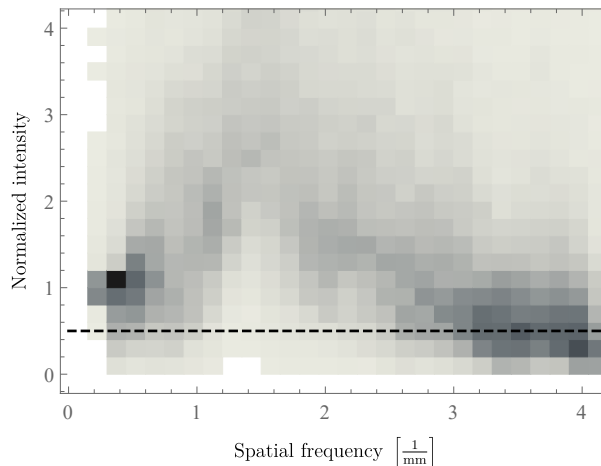


FIGURE 7.4: Modulation transfer function obtained from the ESF using numerical derivatives of the LSF for the CV UTE sequence. Showing a density histogram of 532 MTFs from 13 slices with bin widths of $0.15 \frac{1}{mm}$ in x direction and $0.2 \frac{1}{mm}$ in y direction.

This resolution analysis was performed by obtaining the modulation transfer function by obtaining the Fourier transform of the derivative of the edge spread function. 13 slices have been included in the analysis. For each slice two edges were used and every second line for each of these edges were used. The resolution modulation transfer functions are very erratic as shown in figure 7.4.

In order to further illustrate the point of how erratically this results are a histogram of all the single results has been produced. As shown in figure 7.5.

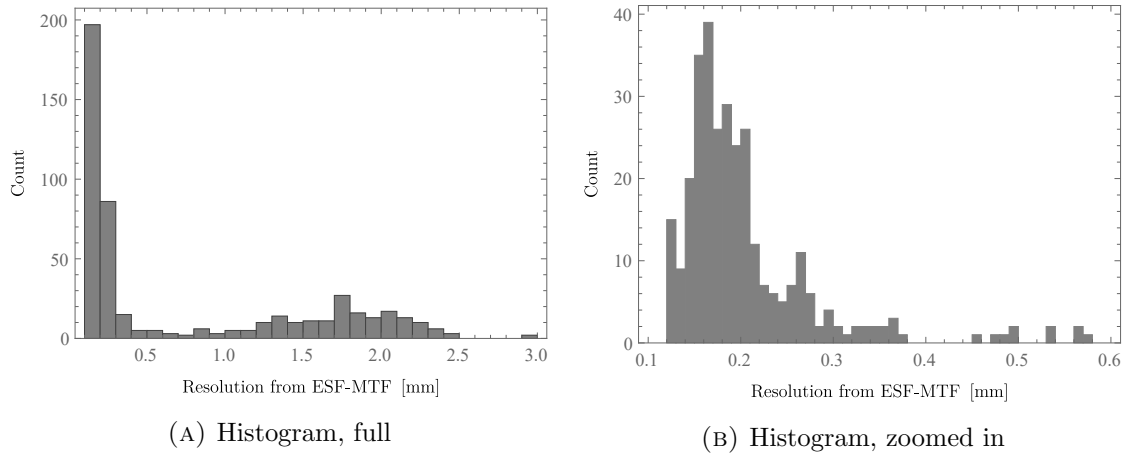


FIGURE 7.5: Histograms of the resolution results obtained for the CV UTE sequence from ESF-MTF analysis. The histogram on the left hand side has a bin width of 0.1. The one on the right hand side has a bin width of 0.01.

Based on this analysis a resolution of $(770. \pm 18.)\mu m$ was calculated. As said before this value should be considered rather unreliable.

7.2.3.2 Point Spread Function using Gaussian Fit

Resolution analysis was also performed by fitting a Gaussian function into the integrated Point Spread Function using `fityk`[10]. Integration was performed in x direction, this is therefore an investigation of the line spread function in y-direction, see section 2.4.2.

Only one slice could be found which was low enough in noise to perform this analysis. The error shown is therefore the fit error of this Gaussian function. This result also remains questionable because the LSF obtained from the PSF is non Gaussian, the edge enhancement artefacts a suspected cause of this.

The analysis has been performed using the $(204.8 \pm 0.2)\mu m$ phantom PSF structure.

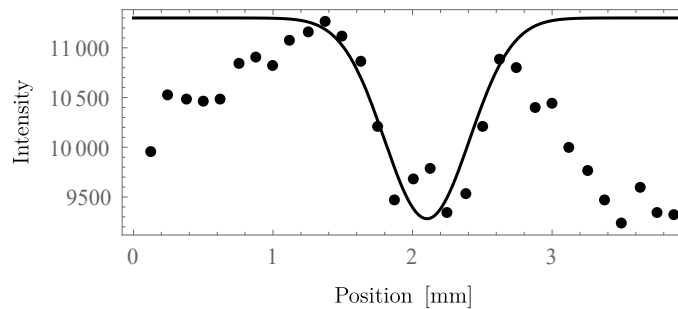


FIGURE 7.6: Point spread function analysis using Gaussian fits of the line spread function in CV UTE. Data points shown are without spline baseline subtraction but with constant baseline adjustment performed by subtracting the average of the data points left of the peak.

The data used for the fit and the fitted Gaussian function are shown in figure 7.6. **The FWHM, and therefore the resolution for this slice of the standard protocol of the CV UTE sequence is $(718. \pm 32.)\mu m$.** Within error margins this is very close to the resolution measure obtained using the ESF-MTF method of $(770. \pm 18.)\mu m$.

It should still be noted that the object size is close to the resolution obtained and might therefore skew the results towards lower resolution.

7.2.4 Edge Overshoot

This sequence shows very strong edge enhancement artefacts, see section 7.6.1 for more details of this artefact and section 3.2 for a theoretical background.

An analysis was performed using the Mathematica Analysis Toolkit as outlined in section 2.5.

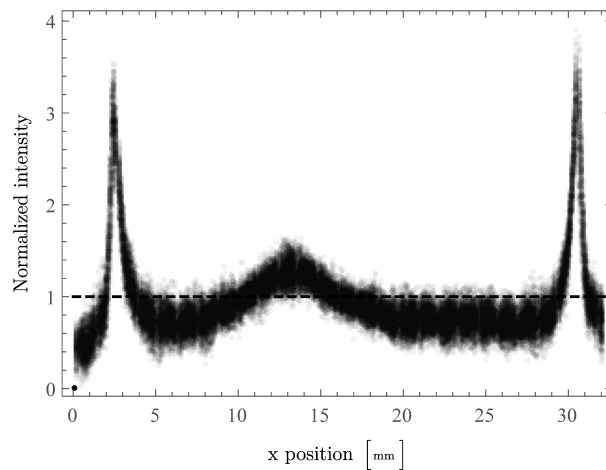


FIGURE 7.7: Line profiles of all lines used for the edge overshoot analysis in the CV UTE sequence. Normalized by dividing each line by the mean inside the edges.

Line profiles were used from lines 119 (pixel position, y-direction) up to line 136. For each line an average value was calculated for x positions from 88px to 170px. Each line was divided by its mean value and the mean value of the maximum in each line was used as the result for each slice. In total 252 line profiles were included in the analysis. All these line profiles are shown in figure 7.7.

The result for the edge overshoot analysis of the CV UTE standard protocol is $(309.8 \pm 5.3)\%$.

This is a very severe artefact which severely restricts the usefulness of images obtained with the sequence. There is a second artefact visible inside the line profiles where the center appears more signal intense than the regions between the edges and center.

7.2.5 Results

Results for the standard protocol are shown in figure 7.8 and table 7.2.

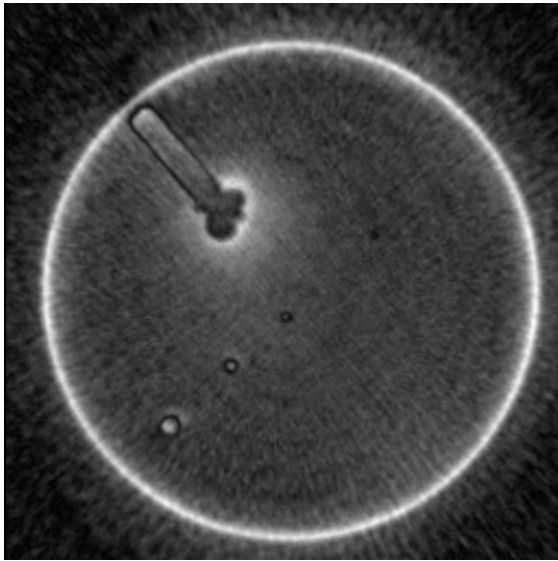
SNR	5.553 ± 0.053
SNR _{corr}	3.637 ± 0.035
SNR _{diff}	23.952 ± 0.088
Resolution, ESF [μm]	$770. \pm 18.$
Resolution, PSF Y [μm]	$718. \pm 32.$
Edge overshoot [%]	309.8 ± 5.3
Diameter [mm]	31.7467 ± 0.009
Geometric error [%]	0.628 ± 0.039

TABLE 7.2: Measurement results for the CV UTE standard protocol.

As can be seen the edge overshoot is quite high at $(309.8 \pm 5.3)\%$, SNR is rather low as well as resolution. The primary cause of these problems is edge enhancement and blurring, as discussed in section 3.2.

It can also be observed that the phantom diameter seems larger than it really is due to the artefacts in this sequence.

Several attempts have been made to correct these k-space trajectory problems. It is possible, in principle, to adjust the corrections for the gradient performance inside the sequence source code.[3]



TE	0.67 ms
TR	200 ms
Avg	2
FOV	$(32. \times 32.) \text{ mm}^2$
BW	$300 \frac{\text{Hz}}{\text{Px}}$
Slice	$125. \mu\text{m}$
α	39°
Base	256×256
Radial	13000
Voxel	$(125. \times 125. \times 125.) \mu\text{m}^3$
TA	21:45
Seq	CV UTE

FIGURE 7.8: Standard protocol for the CV UTE sequence.

Another option would be to perform a post processing correction.[2]

7.3 Thermal Behavior

The CV UTE sequence has the most critical thermal behavior. Requiring the closest attention when selecting sequence parameters and performing measurements.

Measurements for the thermal behavior of the CV UTE sequence have been performed as described in section 5.5. The results of these measurements are shown in figure 7.9.

The standard protocol with adjusted TR times was used for this measurement. For measurements with short TR times the averages were increased in order to allow the system to reach a thermodynamic equilibrium state.

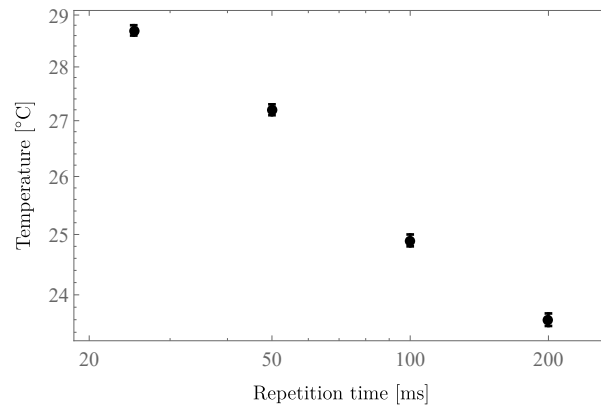


FIGURE 7.9: Thermal behavior of the CV UTE sequence as shown in a log-log plot.

During these measurements the sequence had to be stopped during the 25ms repetition time measurement because the temperature was quickly rising. This measurement is shown in figure 7.10.

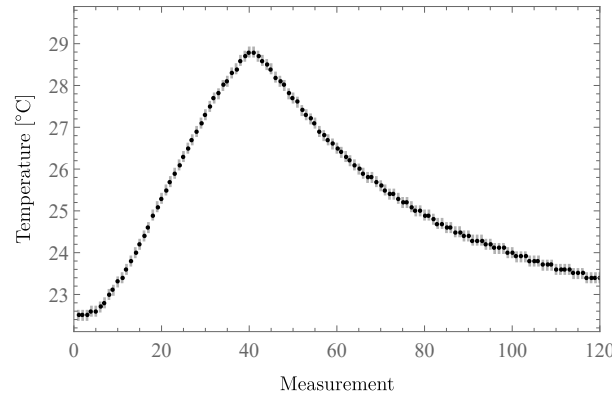


FIGURE 7.10: Temperature rise during the CV UTE 25ms measurement for the investigation of the sequences thermal behavior. The measurement was stopped at approximately the 30st temperature measurement.

7.4 Minimum TE

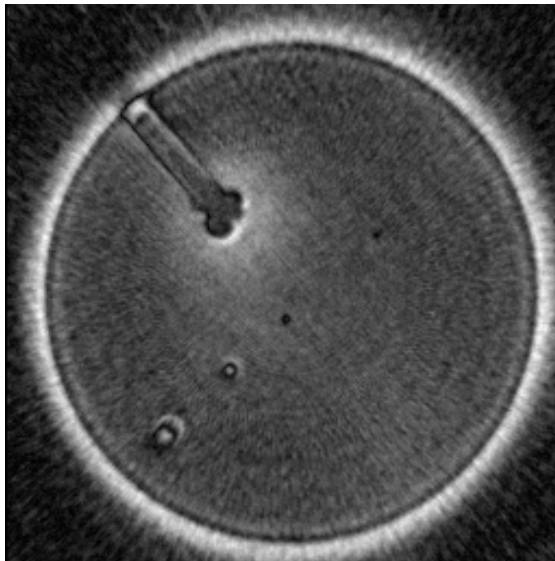
In this measurement the standard protocol was varied by setting the TE to its minimum setting of 0.07ms.

	Standard TE 0.67	TE 0.07
SNR	5.553 ± 0.053	5.516 ± 0.033
SNR _{corr}	3.637 ± 0.035	3.613 ± 0.022
Resolution [μm]	$770. \pm 18.$	$854. \pm 41.$
Edge overshoot [%]	309.8 ± 5.3	260.2 ± 3.2
Diameter [mm]	31.7467 ± 0.009	31.82 ± 0.0066
Geometric error [%]	0.628 ± 0.039	0.294 ± 0.027

TABLE 7.3: CV UTE at minimum TE of 0.07ms, otherwise using the standard protocol.

The results for this minimum TE measurement, table 7.3 and figure 7.11, are very similar to the standard protocol at a TE of 0.67ms.

In the image, figure 7.11, some change in the edge enhancement can be observed, the overshoot value is also reduced somewhat down to $(260.2 \pm 3.2)\%$ but this artefact is still quite pronounced.



TE	0.67 ms
TR	200 ms
Avg	2
FOV	$(32. \times 32.) \text{ mm}^2$
BW	$751 \frac{\text{Hz}}{\text{Px}}$
Slice	$125. \mu\text{m}$
α	39°
Base	256×256
Radial	13000
Voxel	$(125. \times 125. \times 125.) \mu\text{m}^3$
TA	21:45
Seq	CV UTE

FIGURE 7.11: CV UTE sequence at minimum TE and standard protocol otherwise.

7.5 Parameter Variation

Parameter variation as described in section 5.4 has also been performed for this sequence.

Parameter	SNR	SNR _{corr}	Resolution [μm]	Edge overshoot [%]	Diameter [mm]	Geometric error [%]
TE 0.07ms	5.516 ± 0.033	3.613 ± 0.022	$854. \pm 41.$	260.2 ± 3.2	31.82 ± 0.0066	0.294 ± 0.027
TE 0.3ms	4.017 ± 0.029	2.631 ± 0.019	$659. \pm 16.$	477.8 ± 9.1	31.859 ± 0.0017	0.1385 ± 0.0089
Standard	5.553 ± 0.053	3.637 ± 0.035	$770. \pm 18.$	309.8 ± 5.3	31.7467 ± 0.009	0.628 ± 0.039
TE 1ms	6.57 ± 0.053	4.304 ± 0.035	$893. \pm 53.$	249.8 ± 3.4	31.493 ± 0.027	1.238 ± 0.066
TE 2ms	9.172 ± 0.057	6.008 ± 0.037	$608. \pm 40.$	$194. \pm 2.4$	30.391 ± 0.039	1.987 ± 0.078
TE 5ms	11.84 ± 0.069	7.755 ± 0.046	$497. \pm 16.$	141.13 ± 0.46	28.671 ± 0.021	0.86 ± 0.15
TE 10ms	10.099 ± 0.094	6.615 ± 0.061	$439.1 \pm 9.$	152.5 ± 2.7	28.789 ± 0.044	1.83 ± 0.16

TABLE 7.4: Echo time parameter variation for the CV UTE sequence.

7.5.1 Echo Time

TE has been varied quite extensively to find a relationship between echo time and severity of the artefacts.

The results of these variations are shown in table 7.4.

It can be observed that signal to noise ratios improve with increased TE. Interestingly there is also a small improvement from TEs about 5 to 10 times larger than minimum TE.

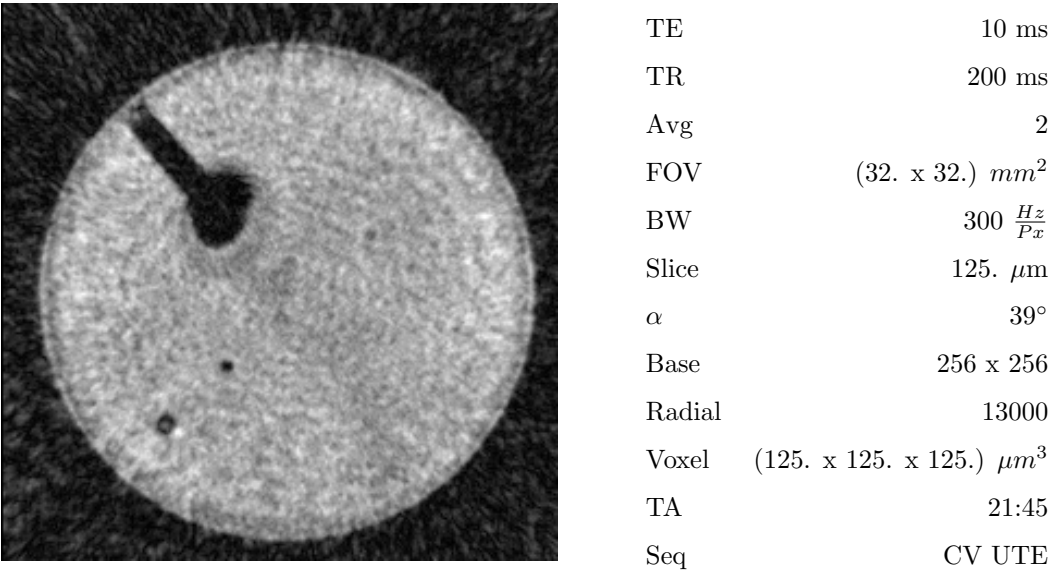


FIGURE 7.12: CV UTE standard protocol with TE changed to 10ms.

Resolution and edge enhancement also improve with longer echo times. This is expected as the switching part at the beginning of the detection makes less of a contribution in the total acquisition window and k-space trajectory errors are therefore reduced for longer echo times.

Overall artefacts are greatly improved at these long echo times. On the other hand at these long echo times, sequences with far better performance are available. As using a UTE sequence at such long echo times seems pointless, the choice was made to not increase the TE for the remaining evaluations of the CV UTE sequence.

7.5.2 Averages

In this series the amount of averages has been varied.

The results of the averages variation are shown in table 7.5.

	Avg 1	Standard	Avg 4	Avg 6
SNR	5.387 ± 0.052	5.553 ± 0.053	5.476 ± 0.049	5.531 ± 0.055
SNR _{corr}	3.529 ± 0.034	3.637 ± 0.035	3.587 ± 0.032	3.623 ± 0.036
Resolution [μm]	$802. \pm 20.$	$770. \pm 18.$	$777. \pm 19.$	$752. \pm 21.$
Edge overshoot [%]	309.5 ± 5.4	309.8 ± 5.3	$308.6 \pm 5.$	308.5 ± 5.3
Diameter [mm]	31.771 ± 0.011	31.7467 ± 0.009	31.767 ± 0.012	31.754 ± 0.012
Geometric error [%]	0.537 ± 0.038	0.628 ± 0.039	0.513 ± 0.046	0.594 ± 0.041

TABLE 7.5: Averages parameter variation, CV UTE sequence.

There is no significant improvement for any of the quality control quantities. This is probably caused by the severe artefacts, where artefacts of this type see hardly any improvement with increased averaging.

7.5.3 Matrix Size

For all of these measurements the radial views have been increased to 60 000 and kept constant, to reduce the impact that the number of radial views have, and to examine only the impact the different matrix sizes have.

	Matrix 128	Matrix 192	Matrix 256
SNR	15.02 ± 0.12	6.334 ± 0.058	5.56 ± 0.025
SNR _{corr}	9.838 ± 0.074	4.149 ± 0.038	3.642 ± 0.017
Resolution [μm]	$781. \pm 31.$	$1078. \pm 21.$	$1071. \pm 20.$
Edge overshoot [%]	195.9 ± 3.4	325.7 ± 8.7	346.3 ± 5.8
Diameter [mm]	28.4117 ± 0.008	30.547 ± 0.047	31.776 ± 0.012
Geometric error [%]	0.539 ± 0.02	2.432 ± 0.073	0.444 ± 0.044

	Matrix 384	Matrix 512
SNR	4.948 ± 0.011	4.289 ± 0.015
SNR _{corr}	3.2406 ± 0.0069	2.8092 ± 0.0093
Resolution [μm]	$1252. \pm 26.$	$1116. \pm 12.$
Edge overshoot [%]	$353.8 \pm 3.$	311.3 ± 2.7
Diameter [mm]	31.9069 ± 0.00052	31.9309 ± 2.1
Geometric error [%]	0.0873 ± 0.0029	0.0617156 ± 2.2

TABLE 7.6: Matrix size variation, CV UTE sequence.

The interesting observation in these results (table 7.6) is, that with decreasing matrix size the artefacts also decrease and the resolution actually improves. The 128x128 matrix has the same resolution in the edge spread function as the 512x512 matrix.

This artefact is probably caused by the increase in gradient strength required for larger matrices and therefore the k-space trajectory errors become more prominent.

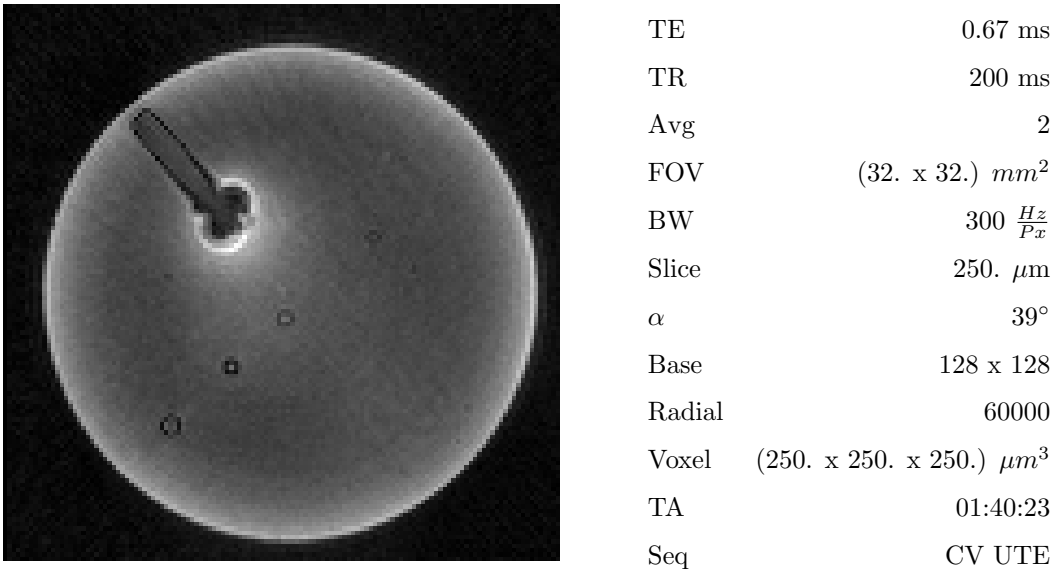


FIGURE 7.13: CV UTE at 128x128 matrix size and 60 000 radial views. Otherwise the standard protocol was used.

Edge overshoot is also less severe at smaller matrix sizes.

Signal to noise ratio decreases with increasing matrix sizes. This is to be expected as voxel sizes decrease.

Visually these two can also be compared, the smallest matrix size of 128x128 in figure 7.13 and the 512x512 matrix in figure 7.14.

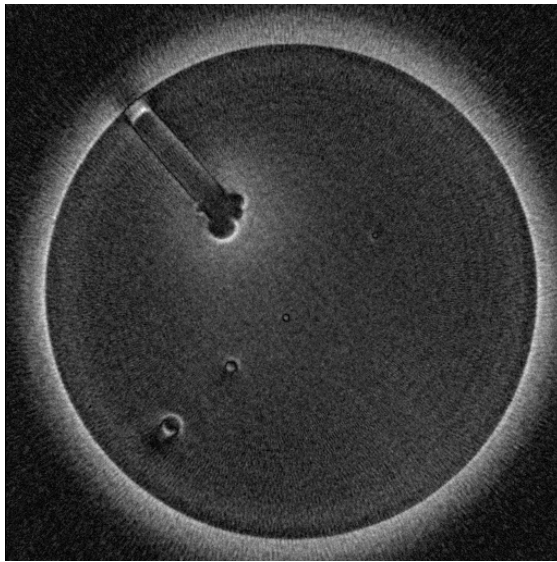
7.5.4 Radial Views

For the variation of radial views the standard protocol and standard matrix size of 256x256 was used.

Radial views can be set to values up to 100 000.

Table 7.7 contains the results of the radial views variations. Diameter and geometric error remained within error margins of the standard protocol.

It is notable that with increasing the number of radial views the SNR slightly increases. But resolution decreases first before improving again. With the strong artefacts found in these



TE	0.67 ms
TR	200 ms
Avg	2
FOV	(32. x 32.) mm ²
BW	296 $\frac{Hz}{Px}$
Slice	62.5 μ m
α	39°
Base	512 x 512
Radial	60000
Voxel	(62.5 x 62.5 x 62.5) μ m ³
TA	01:40:23
Seq	CV UTE

FIGURE 7.14: Base size of 512x512 with 60 000 radial views in the CV UTE sequence during parameter variation.

Radial views	6000	Standard 13 000	20 000
SNR	5.437 ± 0.063	5.553 ± 0.053	5.617 ± 0.042
SNR _{corr}	3.561 ± 0.041	3.637 ± 0.035	3.679 ± 0.028
Resolution [μ m]	$632. \pm 29.$	$770. \pm 18.$	$964. \pm 27.$
Edge overshoot [%]	282.7 ± 4.7	309.8 ± 5.3	320.7 ± 5.8

Radial views	40 000	60 000	100 000
SNR	5.707 ± 0.02	5.56 ± 0.025	6.144 ± 0.016
SNR _{corr}	3.738 ± 0.013	3.642 ± 0.017	4.024 ± 0.011
Resolution [μ m]	$979. \pm 23.$	$1071. \pm 20.$	$749. \pm 24.$
Edge overshoot [%]	$336.7 \pm 6.$	346.3 ± 5.8	392.8 ± 6.5

TABLE 7.7: Radial views parameter variation with 256x256 matrices, CV UTE sequence.

measurements it remains open to question how reliable the MTF is as a measure of achievable resolution.

Slices from all different settings are shown in figure 7.15.

At the highest radial views setting possible, 100 000 radial views, some new artefacts are seen. Up to 60 000 the image quality seems to improve. Whereas nominal resolution according to the ESF modulation transfer evaluation worsens. It can also be noted that the four largest phantom structures are visible in this image. But the smaller ones don't obtain enough contrast to satisfy the MTF resolution criterion.

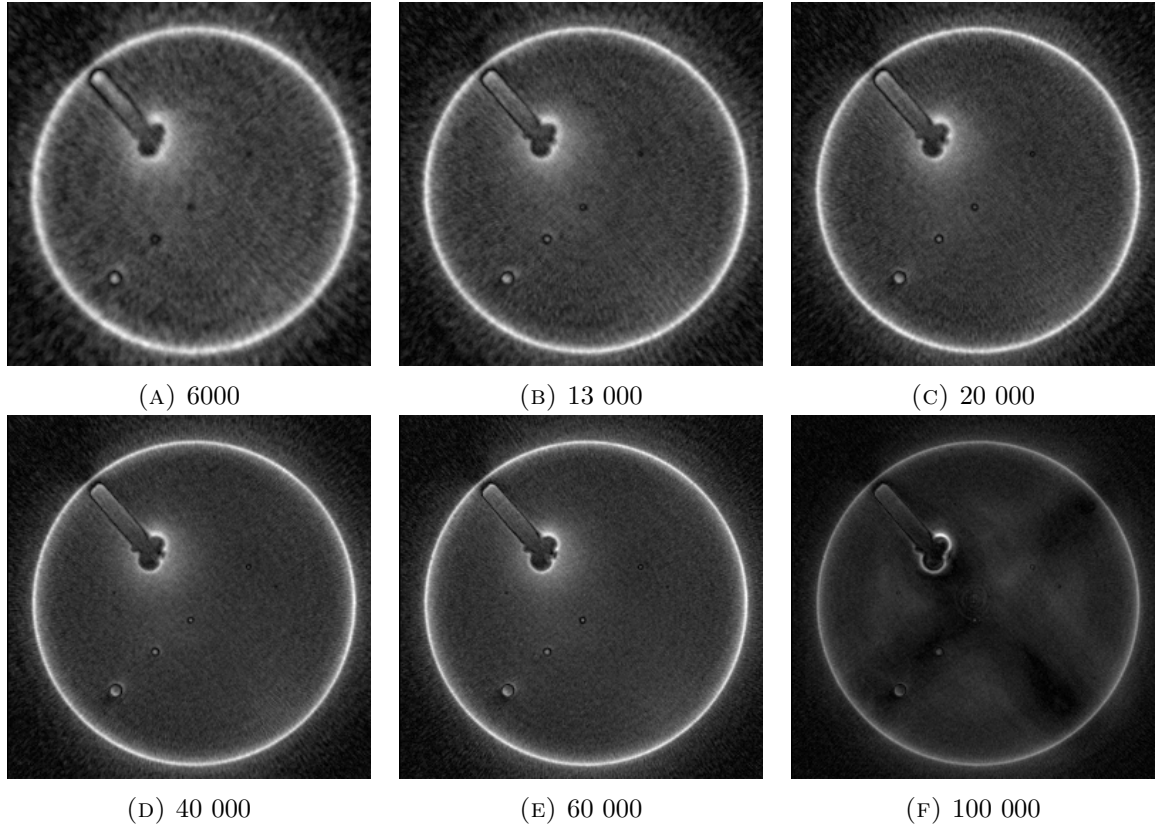


FIGURE 7.15: Comparison of different radial view settings.

7.5.5 Bandwidth

Bandwidth was varied while closely monitoring the temperature of the system.

	Standard $300 \frac{Hz}{px}$	$488 \frac{Hz}{px}$	$751 \frac{Hz}{px}$
SNR	5.553 ± 0.053	5.733 ± 0.054	5.499 ± 0.025
SNR _{corr}	3.637 ± 0.035	3.755 ± 0.036	3.602 ± 0.017
Resolution [μm]	$770. \pm 18.$	$754. \pm 23.$	$959. \pm 34.$
Edge overshoot [%]	309.8 ± 5.3	312.3 ± 5.1	263.3 ± 3.6
Diameter [mm]	31.7467 ± 0.009	31.728 ± 0.012	31.8299 ± 0.0059
Geometric error [%]	0.628 ± 0.039	0.576 ± 0.04	0.258 ± 0.027

TABLE 7.8: Bandwidth parameter variation, CV UTE sequence.

The results for the bandwidth variation, table 7.8, show little significant change to the results obtained using the standard protocol.

What is noteworthy is that the resolution becomes worse with increasing bandwidth. This was not observed with the XD VTE sequence. On the other hand the signal to noise ratio remains

constant, within error margins. This signal to noise ratio is very low due to very pronounced artefacts inside the image in the first place.

Geometric error and edge overshoot improve with increasing bandwidth. Whereas the geometric error is generally low for all measurements.

7.5.6 Filters

Parameter variation for the CV UTE filters has been performed as before and is printed in table 7.9.

Both elliptical filters produce a significantly different image.

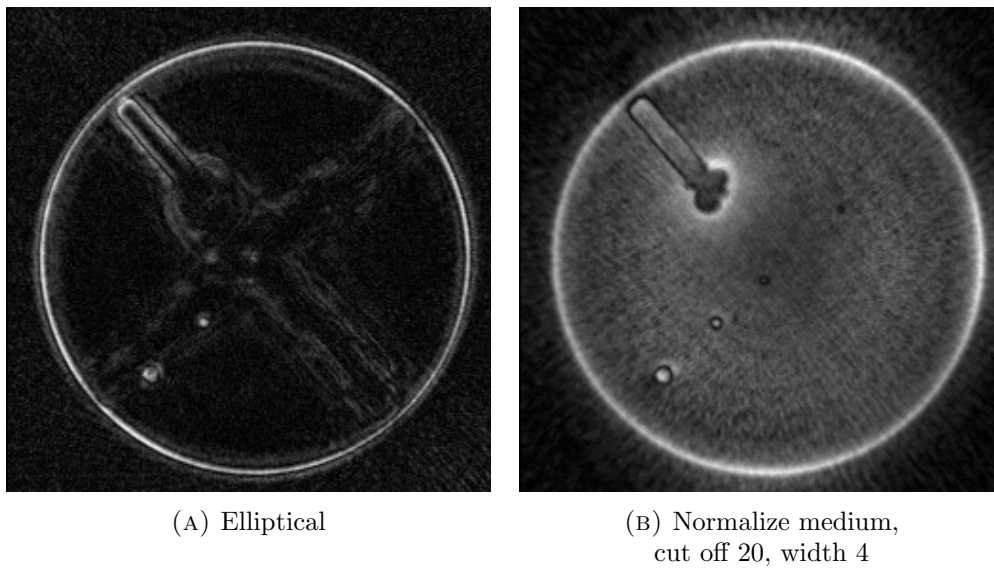


FIGURE 7.16: Filters for the CV UTE sequence, added to the standard protocol.

An elliptical filter, or also called Cauer filter, is a type of filter which has an even ripple in its frequency response.[43]

The elliptical filter is also a low band pass. The image also appears to be almost static throughout all slices, see figure 7.16a.

The effect of this filter is also remarkably different from the elliptical filter found in the XD VTE sequence.

Based on these results the normalize filter would be a candidate for image improvement, but most of this improvement can not be confirmed visually. The filter produces less noise signal in the corners which explains the better SNR result. An image processed with this filter in the CV UTE sequence is shown in figure 7.16b.

Parameter	SNR	SNR _{corr}	Resolution [μm]	Edge overshoot [%]	Diameter [mm]	Geometric error [%]
Standard	5.553 \pm 0.053	3.637 \pm 0.035	770. \pm 18.	309.8 \pm 5.3	31.7467 \pm 0.009	0.628 \pm 0.039
Inline/Composition						
Distortion correction 2D	5.459 \pm 0.053	3.575 \pm 0.035	776. \pm 16.	310.9 \pm 5.1	31.765 \pm 0.011	0.522 \pm 0.034
Distortion correction 3D	5.322 \pm 0.062	3.486 \pm 0.041	767. \pm 19.	317.9 \pm 5.1	31.7721 \pm 0.0094	0.516 \pm 0.033
Resolution/Filter						
Image filter medium, edge 3, smoothing 3	4.851 \pm 0.054	3.178 \pm 0.036	712. \pm 16.	334.5 \pm 5.3	31.7946 \pm 0.0089	0.421 \pm 0.041
Image filter sharp, edge 5, smoothing 5	5.444 \pm 0.061	3.566 \pm 0.04	794. \pm 16.	311.8 \pm 5.	31.7613 \pm 0.0089	0.548 \pm 0.036
Image filter smooth, edge 1, smoothing 1	5.714 \pm 0.052	3.743 \pm 0.035	772. \pm 27.	312. \pm 5.3	31.724 \pm 0.011	0.617 \pm 0.031
Distortion correction 2D	5.471 \pm 0.051	3.584 \pm 0.033	776. \pm 16.	308.8 \pm 5.1	31.7674 \pm 0.0098	0.532 \pm 0.036
Distortion correction 3D	5.58 \pm 0.046	3.655 \pm 0.031	788. \pm 20.	258.5 \pm 3.8	31.645 \pm 0.018	0.853 \pm 0.049

Parameter	SNR	SNR _{corr}	Resolution [μm]	Edge overshoot [%]	Diameter [mm]	Geometric error [%]
Normalize medium, cutoff 20, width 4	10.779 ± 0.083	7.06 ± 0.055	$809. \pm 25.$	313.7 ± 4.7	30.576 ± 0.021	2.911 ± 0.037
B1 filter medium	5.471 ± 0.046	3.583 ± 0.03	$789. \pm 24.$	307.5 ± 5.1	31.765 ± 0.0086	0.524 ± 0.035
Elliptical filter in- plane	1.5862 ± 0.0058	1.0389 ± 0.0038	$1332. \pm 18.$	887.2 ± 2.3	31.8614 ± 0.00047	0.1254 ± 0.0017
Elliptical filter vol- ume	1.5859 ± 0.0048	1.0388 ± 0.0032	$750. \pm 19.$	895.1 ± 2.6	31.8614 ± 0.00047	0.1254 ± 0.0017

TABLE 7.9: Parameter variation for the filters in the CV UTE sequence.

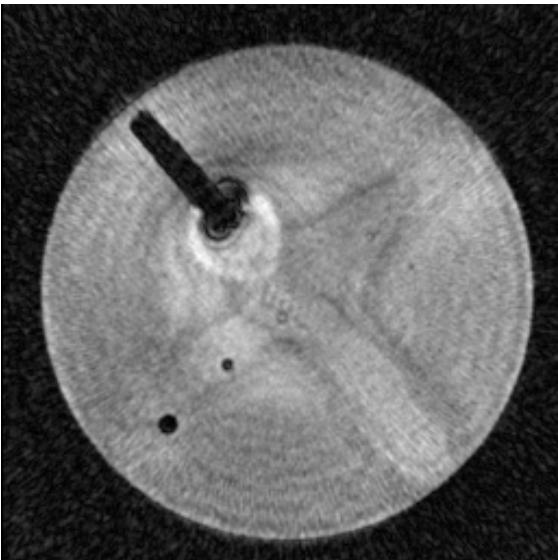
The filters don't improve image quality in this protocol in any significant way and therefore none of them can be recommended for use with this protocol or similar ones. Maybe some benefit can be seen after the pervasive artefacts have been eliminated or reduced.

Distortion correction in the inline/composing tab causes a slight, and significant with respect to error margins, improvement in the geometric error. Interestingly the 3D distortion correction in the resolution/filters tab seems to have the opposite effect.

7.5.7 Other Settings

Every remaining setting available for the CV UTE sequence was investigated using parameter variation. The results of this variation are presented in table 7.10.

The only one of these settings which causes a significant impact on image quality is turning the asymmetric echo off. This in turn causes a new minimum TE of 2.82ms, for the standard protocol.



TE	2.82 ms
TR	200 ms
Avg	2
FOV	(32. x 32.) mm ²
BW	300 $\frac{Hz}{Px}$
Slice	125. μ m
α	39°
Base	256 x 256
Radial	13000
Voxel	(125. x 125. x 125.) μ m ³
TA	21:45
Seq	CV UTE

FIGURE 7.17: CV UTE standard protocol with asymmetric echo set to off.

With this setting the SNR, resolution and edge overshoot improve by a factor of at least 2.

Although there is some improvement with increasing the TE, as demonstrated in section 7.5.1, the improvement in the SNR and resolution produced by setting the asymmetric echo to off exceeds this improvement by far. This is also readily visible in figure 7.17 showing the acquisition with this setting, used for this analysis.

Parameter	SNR	SNR _{corr}	Resolution [μm]	Edge overs. [%]	Diameter [mm]	Geometric error [%]
Standard	5.553 ± 0.053	3.637 ± 0.035	$770. \pm 18.$	309.8 ± 5.3	31.7467 ± 0.009	0.628 ± 0.039
Asymmetric echo weak	5.492 ± 0.053	3.597 ± 0.035	$750. \pm 19.$	306.8 ± 4.8	31.756 ± 0.012	0.57 ± 0.045
Asymmetric echo off	13.57 ± 0.17	8.89 ± 0.11	$302. \pm 5.2$	135.11 ± 0.43	28.2481 ± 0.0079	0.289 ± 0.02
Allowed delay 2s	5.442 ± 0.053	3.565 ± 0.035	$772. \pm 22.$	312.2 ± 5.1	31.761 ± 0.012	0.543 ± 0.045
Segments 8	4.84 ± 0.049	3.17 ± 0.032	$985. \pm 28.$	311.5 ± 5.6	31.8294 ± 0.0044	0.243 ± 0.016
RF pulse type fast	5.363 ± 0.05	3.513 ± 0.033	$781. \pm 16.$	313.6 ± 5.3	31.768 ± 0.012	0.502 ± 0.042
Gradient mode normal	5.056 ± 0.043	3.312 ± 0.028	$776. \pm 21.$	316.1 ± 5.6	31.8036 ± 0.0082	0.398 ± 0.038
Gradient mode whisper	4.986 ± 0.042	3.266 ± 0.028	$781. \pm 19.$	$315. \pm 5.5$	31.8073 ± 0.0086	0.361 ± 0.037
RF spoiling off	5.513 ± 0.05	3.611 ± 0.033	$779. \pm 19.$	$308.2 \pm 5.$	31.7552 ± 0.01	0.584 ± 0.039

TABLE 7.10: Parameter variation of the other settings of the CV UTE sequence.

The usefulness of this setting still remains questionable, as the XD VTE sequence can be used in this TE range and achieves far better performance at this echo time, for comparison to the XD VTE sequence at longer echo times refer to table 6.3.

7.5.8 Settings Which Cause Execution Errors

Setting the trajectory to “Cartesian” in the resolution/common tab causes the measurement to fail.

When any magnetic preparation is set in the contrast/common tab the SAR is increased to 400% as soon as the measurement is started. This can only be fixed by registering a new patient.

7.6 Artefacts

7.6.1 Blurring and Edge Enhancement

Artefacts based on k-space trajectory errors, the theoretical background for those is explained in section 3.2, are very prominent in the CV UTE sequence, as can be seen in the image of the standard protocol, figure 7.8.

These artefacts remain very strong, and none of the filters or other settings could reduce these sufficiently.

These strong artefacts made any analysis difficult and the obtained results less reliable.

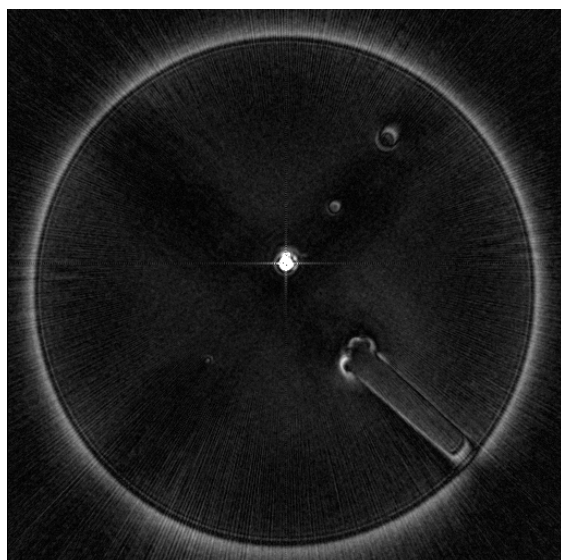
Without further correction these make the sequence less useful and it should only be considered for measurements which require very short echo times but at low spatial resolution.

7.6.2 Zero Point Artefact

The CV UTE sequence also displays a zero point artefact.

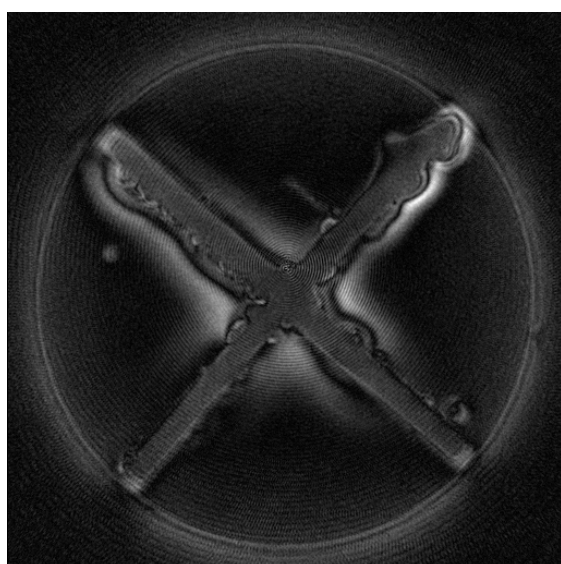
An example of this artefact in the CV UTE sequence can be seen in figure 7.18.

This artefact is explained in detail in section 3.4.



TE	0.07 ms
TR	780 ms
Avg	2
FOV	(32. x 32.) mm ²
BW	751 $\frac{Hz}{Px}$
Slice	62.5 μ m
α	36°
Base	512 x 512
Radial	100000
Voxel	(62.5 x 62.5 x 62.5) μ m ³
TA	10:52:35
Seq	CV UTE

FIGURE 7.18: Zero point artefact in the CV UTE sequence.



TE	0.07 ms
TR	780 ms
Avg	2
FOV	(32. x 32.) mm ²
BW	751 $\frac{Hz}{Px}$
Slice	62.5 μ m
α	36°
Base	512 x 512
Radial	100000
Voxel	(62.5 x 62.5 x 62.5) μ m ³
TA	10:52:35
Seq	CV UTE

FIGURE 7.19: Ringing artefact in the CV UTE sequence.

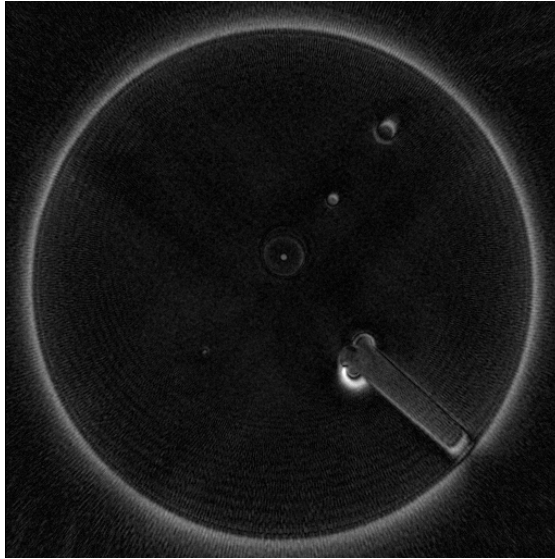
7.6.3 Ringing or Moire Artefact

Another artefact which can be observed mostly at large matrix sizes and in the slices further away from the isocenter is a kind of ringing artefact, as seen in figure 7.19.

This artefact doesn't look like Gibbs ringing, but could be caused by some kind of frequency undersampling. Caused by the fact that when the field of view is moved away from the isocenter this is done during reconstruction and not during measurement.[11]

7.7 Overnight Measurements

Two different over night measurements were performed with the goal of obtaining high resolution images. One was done at the minimum TE for the CV UTE of 0.07ms, figure 7.20, and the second one with an echo time of 0.8ms, figure 7.21, to make it comparable to the high resolution measurement employing the XD VTE sequence.



TE	0.07 ms
TR	780 ms
Avg	2
FOV	(32. x 32.) mm ²
BW	751 $\frac{Hz}{Px}$
Slice	62.5 μm
α	36°
Base	512 x 512
Radial	100000
Voxel	(62.5 x 62.5 x 62.5) μm^3
TA	10:52:35
Seq	CV UTE

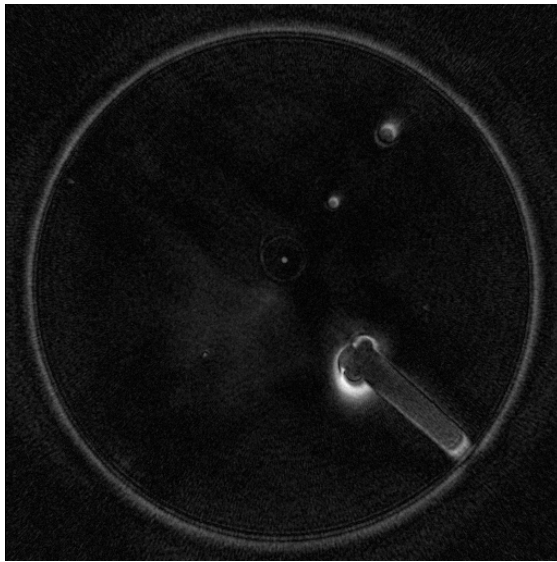
FIGURE 7.20: CV UTE over night, high resolution measurement at minimum TE.

Both images contain significant artefacts. Facts, which reduce SNR considerably down to $SNR = (2.57 \pm 0.012)$, for the minimum TE sequence and 2.547 ± 0.041 for the second sequence.

Due to these prominent artefacts the resolution obtained according to the ESF analysis is only $(742.3 \pm 9.4)\mu m$ for minimum echo time and $(756. \pm 23.)\mu m$ for TE 0.8ms.

Edge overshoot is also very strong in both of these images with overshoots of $(702.8 \pm 4.4)\%$ for minimum TE and $(579. \pm 12.)\%$ at the longer TE.

The strongest artefact in these images appears to be a shift in k-space to larger values. Which makes the very low k-space frequency central part of the phantom appear non signal intense.

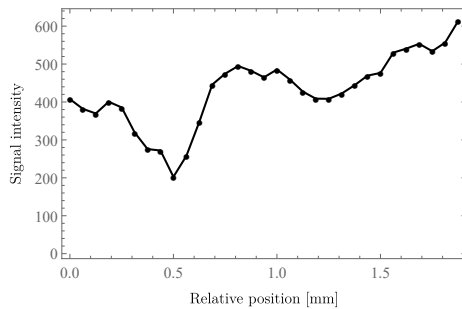


TE	0.75 ms
TR	780 ms
Avg	2
FOV	(32. x 32.) mm ²
BW	751 $\frac{Hz}{Px}$
Slice	62.5 μm
α	36°
Base	512 x 512
Radial	100000
Voxel	(62.5 x 62.5 x 62.5) μm^3
TA	10:52:35
Seq	CV UTE

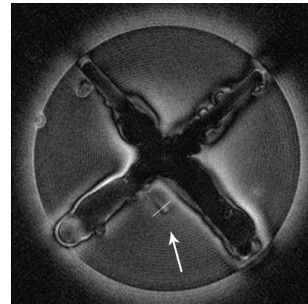
FIGURE 7.21: CV UTE high resolution measurement with a TE of 0.8ms.

7.8 Slice Thickness

Analysis of the slice thickness should not be considered very reliable with the strong artefacts present in these measurements.



(A) Line profile.



(B) Image used for the analysis.

FIGURE 7.22: CV UTE slice thickness analysis data.

For the CV UTE sequence a measurement was selected which had less artefacts but still remained relevant as far as echo times are concerned. The 512x512 matrix, 60 000 projections image obtained during parameter variation was chosen. For detailed settings on this image refer to figure 7.14.

Based on the line profile in figure 7.22a a slice thickness of $(168 \pm 74)\mu m$ was obtained. The nominal slice thickness for this image is $62.5\mu m$. Considering the artefacts present, a blur between slices but also within the slice is to be expected.

DA-3DPR

8.1 Sequence

The density-adapted three-dimensional radial projection reconstruction (DA-3DPR) pulse sequence is a 3D radial k-space sampling sequence which uses density adaptive k-space sampling such that the sampling density of k-space is kept constant, the only exception being the center of k-space which is still oversampled.[13]

This k-space sampling method increases SNR efficiency when compared to classical 3D k-space sampling methods. The theoretical improvement for density adaption is 25.5%. The actual improvement for the DA-3DPR sequence is less than this due to hardware performance restrictions.[13]

The sequence diagram for the DA-3DPR sequence is shown in figure 8.1. This diagram also shows a comparison of the gradient behavior between the DA-3DPR sequence and a classical 3DPR approach.

Gradient shape is trapezoidal initially and density adapted afterwards. The reason for this is that due to hardware restrictions it is impossible to sample the k-space center with the same density adaption. The shape of the gradient after the trapezoidal part is given by equation 8.1, where t_0 is the time, after which the change over occurs and k_0 is $k(t_0)$, $\bar{\gamma}_n$ is the gyromagnetic ratio divided by 2π . [13]

$$G(t) = k_0^2 G_0 (3\bar{\gamma}_n k_0^2 G_0 (t - t_0) + k_0^3)^{-\frac{2}{3}} \quad \forall t \geq t_0 \quad (8.1)$$

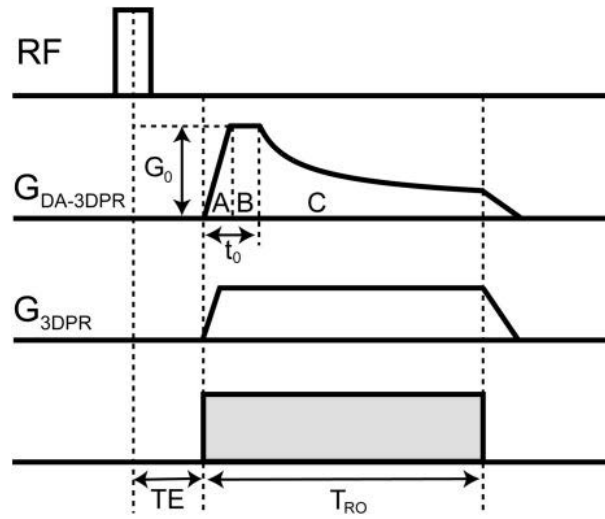


FIGURE 8.1: DA-3DPR sequence diagram.
Image source: Nagel, A. et al[13]

This sequence is the one in this thesis with the largest focus on research, not providing online reconstruction or the ability to change the measurement isocenter position when measuring.

8.2 Reconstruction

This sequence does not provide online ICE reconstruction on the MRI console.

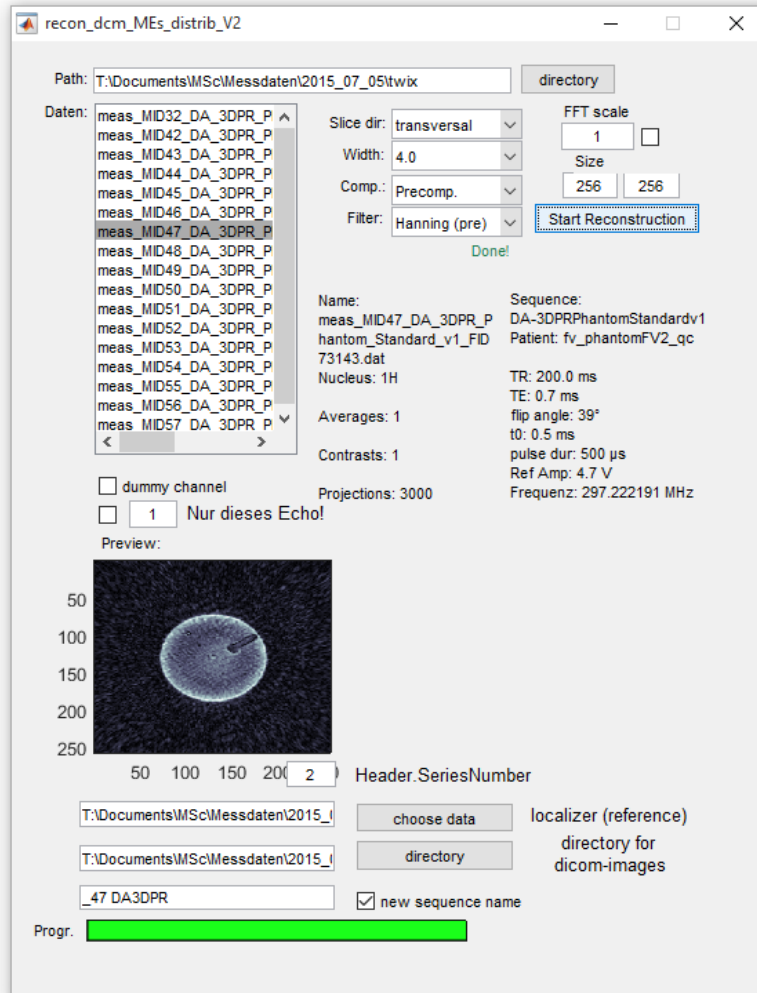


FIGURE 8.2: Screenshot of the custom software for reconstruction of data acquired with the DA-3DPR sequence.

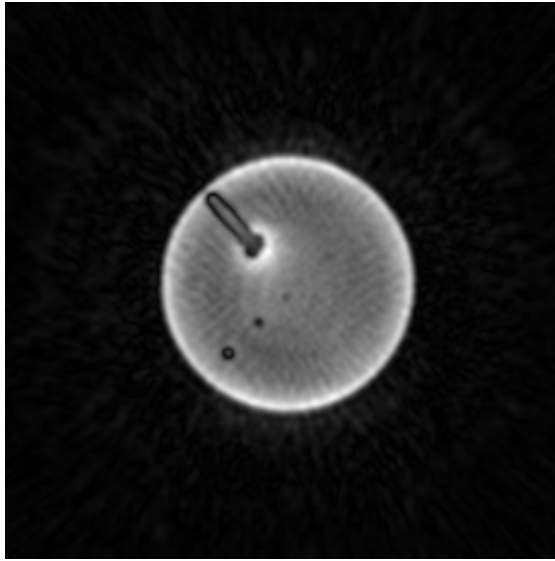
The acquisitions have to be exported via “twix” and are reconstructed using a custom Matlab program provided with the sequence. A screenshot of this software is shown in figure 8.2.[44]

Various options are available for reconstruction, the FFT scale can be used to rescale the data, according to the documentation if the tick is not set it will automatically select the maximum pixel value from the first echo.[44]

The “width” option changes the width of the Kaiser Bessel functions which are used for regridding.[44]

Comp allows to set the density compensation: “The density compensation can be performed before (“Precomp.”) or after the gridding process (“Postcomp.”).”[44]

Setting this option to “Postcomp” has the effect on the image produced of making it appear smoother but less sharp, an example is given in figure 8.3.



TE	0.67 ms
TR	200 ms
Avg	2
FOV	(62.7 x 62.7) mm ²
BW	343.643 $\frac{Hz}{Px}$
Slice	244.9 μm
α	39°
Matrix	256 x 256
Proj.	3000
Voxel	(244.9 x 244.9 x 244.9) μm^3
Seq	DA-3DPR

FIGURE 8.3: DA-3DPR with comp set to postcomp in reconstruction.

Filter allows to choose an FFT filter/window.

For these analysis the optimal settings found were to choose a width of 4, set “Comp” to “Precomp”, use a preprocessing Hanning filter and a matrix size of 256.

The second matrix input field is labeled as the zero filling size in the documentation[44] but not in the actual software used (figure 8.2).

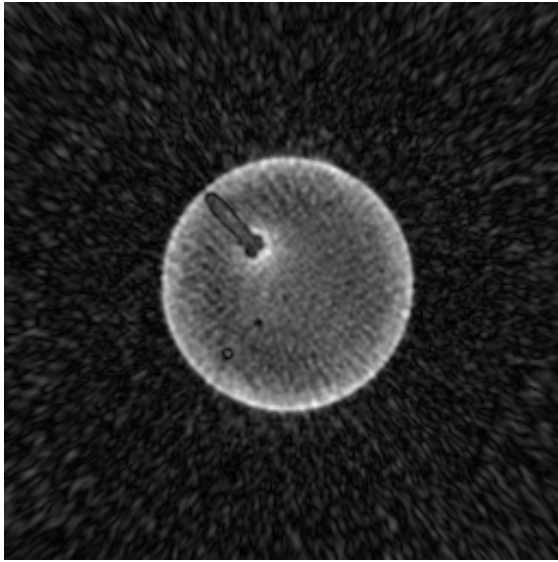
It should be noted that the software is very sensitive to incorrect user input, for example exporting to the same sequence name twice causes a crash and the program needs to be exited, all variables and functions cleared in Matlab and started over again. Special care should therefore be taken to ensure that all input is correct before starting the reconstruction.

One of the issues is that the software often fails to load a different folder after a reconstruction has already been performed. In this case a restart as described above is also required.

Pixel size seems to remain constant under reconstruction, which means that choosing a larger matrix size just causes the FOV to become larger. Even though the original matrix size has been set correctly. This behavior can be overcome by changing the t_0 parameter.

8.3 Standard Protocol

According to the goals of section 5.3 a standard protocol was defined.



TE	0.67 ms
TR	200 ms
Avg	2
FOV	(62.7 x 62.7) mm ²
BW	343.643 $\frac{Hz}{Px}$
Slice	244.9 μ m
α	39°
Matrix	256 x 256
Proj.	3000
Voxel	(244.9 x 244.9 x 244.9) μ m ³
Seq	DA-3DPR

FIGURE 8.4: Standard protocol for the DA-3DPR sequence. Using a 256 reconstruction matrix.

This protocol has a rather low number of radial projections with only 3000 projections, to remain within the set TA of 20 minutes. The long TR was chosen for thermal safety reasons as, among other things, overnight measurements were performed and the exact thermal behavior, and consequences which some settings have on this behavior remained open to investigation. Due to far stronger gradients in a narrower space the microgradient system needs close temperature monitoring in order to ensure that it remains within safe operation limits.

Parameter	Value	Parameter	Value
TE	0.67 ms	BW	300 $\frac{Hz}{px}$
TR	200 ms	Avg	2
α	39°	Filters	none
FOV	(32 mm x 32 mm)	Spoil me	on
Base	364		
Reco Matrix	256x256		
Projections	3000		

TABLE 8.1: DA-3DPR standard protocol.

For most measurements an increase in the number number of projections would be highly advisable.

8.3.1 Signal to Noise Ratio using ROIs

Signal to noise analysis is introduced in detail in section 2.3.

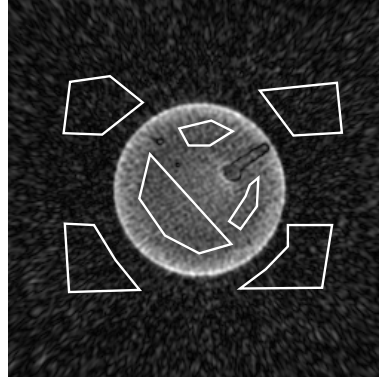


FIGURE 8.5: Regions of interest used for the SNR analysis in the DA-3DPR sequence.

The results for the signal to noise ratios obtained from these ROIs are: $\frac{154.9}{25.4}$, $\frac{155.5}{25.8}$, $\frac{155.8}{26.}$, $\frac{154.9}{25.6}$, $\frac{154.2}{25.7}$, $\frac{153.5}{25.6}$, $\frac{155.2}{25.6}$, $\frac{158.2}{25.4}$, $\frac{160.1}{26.6}$ yielding a **mean signal to noise ratio for the DA-3DPR standard protocol of 6.053 ± 0.025** , and the corrected SNR is **3.965 ± 0.016** .

8.3.2 Signal to Noise Ratio using Difference Images

SNR was also analyzed by obtaining two consecutive measurements and producing difference images for each of the slices of these two measurements. The whole procedure is described in section 2.3.3.

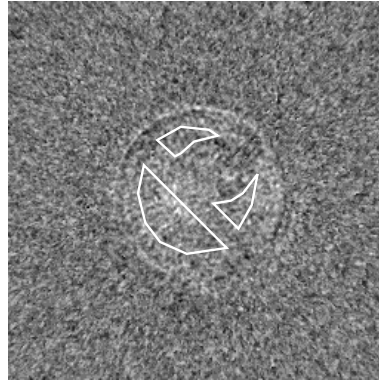


FIGURE 8.6: Difference image of two successive slices used for SNR calculation.

Figure 8.6 shows one of these difference images and the ROIs used for the analysis.

Based on this analysis a SNR_{diff} of 238.1 ± 2.7 was obtained.

This is a very high SNR but it has been confirmed using multiple different measurements, and by analyzing the code in detail. The noise levels remaining after subtraction are only between -2 and +2. The signals are in the order of 200-250. Artefacts are very dominant in these images, but these cancel out almost perfectly as can be seen from the difference image 8.6. Voxels are also very large at $(244.9 \times 244.9 \times 244.9) \mu\text{m}^3$.

A second analysis has been performed using consecutive slices in a single acquisition instead of two different measurements (as described in the NEMA standards[4]). This yields a SNR_{diff} of only 8.7 ± 0.049 , which seems more reasonable, but this method does not confirm to the published standards. Both values should be considered highly unreliable.

8.3.3 Resolution

8.3.3.1 Edge Spread Function using MTF

Analysis of the resolution has been performed by taking the derivative of the edge spread function in order to obtain the line spread function and the Fourier transform of the line spread function to obtain the modulation transfer function. For more details see section 2.4.1.

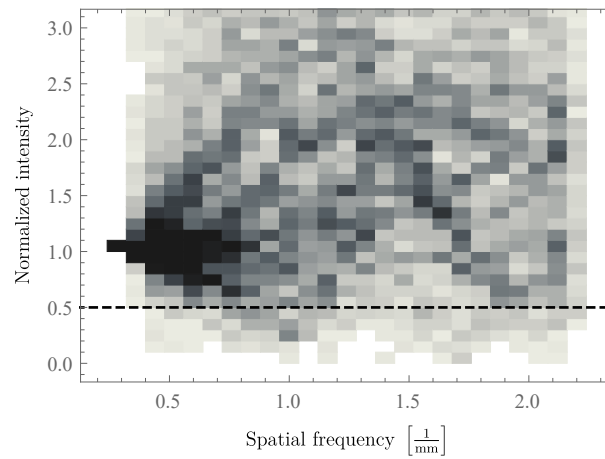


FIGURE 8.7: Modulation transfer function obtained from the ESF using numerical derivatives of the LSF for the DA-3DPR sequence. Showing a density histogram of 180 MTFs from 8 slices with bin widths of $0.08 \frac{1}{\text{mm}}$ in x direction and $0.1 \frac{1}{\text{mm}}$ in y direction.

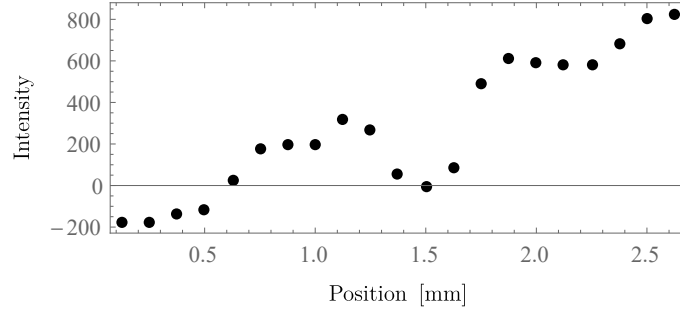
As with the CV UTE sequence the artefacts are very strong in the images of the DA-3DPR standard protocol and a reliable resolution analysis was therefore not possible for the DA-3DPR sequence. The modulation transfer function (figure 8.7) proves to be even more erratic than for the CV UTE sequence. Visually it also becomes quite clear that the edge depicted in these images is not usable for a good quality analysis. This resolution measure is still provided in order to obtain some information of the change with different parameters, but even this usage remains highly doubtful and any conclusions based on these results should be viewed with lots of caution.

8.3.3.2 Point Spread Function using Gaussian Fits

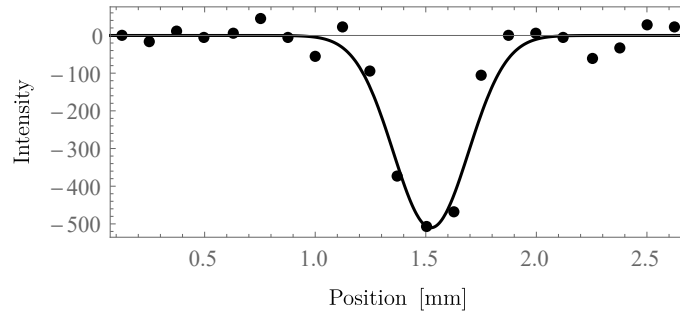
Resolution analysis was also performed by fitting a Gaussian function to the integrated Point Spread Function, the Line Spread Function, using `fityk`[10]. Integration was performed in x direction, the LSF is therefore obtained in y direction.

The analysis was performed based on the $(565.8 \pm 0.2)\mu m$ PSF phantom structure.

Gaussian functions were fitted in `fityk` after a cubic spline baseline correction has been applied.



(A) Without baseline correction



(B) With fit and baseline correction

FIGURE 8.8: Line spread function obtained by integrating the PSF in y direction for the DA-3DPR sequence. Also showing one of the Gaussian fits used for the resolution analysis.

In total 6 slices contained PSF which very usable for the analysis and therefore included. The following FWHM have been obtained from the Gaussian fits $\{400.6, 437.4, 345.2, 234.7, 869.9, 579.0\}\mu m$ which **results in a mean FWHM and therefore resolution of the DA-3DPR standard protocol of $(478 \pm 91)\mu m$.**

The result is smaller than the structure itself in the mean but just equal to the size of the phantom structure within error margins. This can be explained by the very strong artefacts which might actually cause structures to appear smaller than they really are.

8.3.4 Edge Overshoot

Like the CV UTE sequence, this sequence shows very strong edge enhancement artefacts, section 8.6.1 provides more details on this artefact and section 3.2 introduces a theoretical background.

The analysis of the edge overshoot was performed as described in section 2.5.

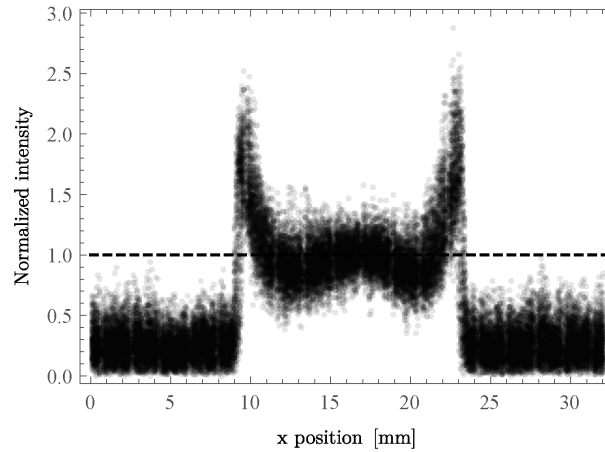


FIGURE 8.9: Line profiles of all lines used for the edge overshoot analysis in the DA-3DPR sequence. Normalized by dividing each line by the mean inside the edges.

Line profiles were used from lines 135 (pixel position, y-direction) up to line 153. For each line an average value was calculated for x positions from 120px to 140px. Each line was divided by its mean value and the mean value of the maximum in each line was used as the result for each slice. In total 171 line profiles were included in the analysis. All these line profiles are shown in figure 8.9.

The result for the edge overshoot analysis for the DA-3DPR sequence is $(210.5 \pm 4.2)\%$.

8.3.5 Results

SNR	6.053 ± 0.025
SNR _{corr}	3.965 ± 0.016
SNR _{diff}	238.1 ± 2.7
Resolution, ESF [μm]	565.8 ± 0.2
Resolution, PSF Y [μm]	478 ± 91
Edge overshoot [%]	210.5 ± 4.2
Diameter [mm]	33.22 ± 0.16
Geometric error [%]	3.73 ± 0.18

TABLE 8.2: Measurement results for the DA-3DPR standard protocol.

Complete quality control analysis has been performed for the standard protocol image. The results for these measurements are shown in table 8.2.

These settings have been chosen in accordance with the goal of comparability of all parameters and thermal safety, as explained above. In a real world setting it would be highly advisable to choose a shorter repetition time, which is not a problem with the uncritical thermal behavior of this sequence, and about 12 000 projections, as discussed in subsection 8.5.2.

8.4 Thermal Behavior

This sequence has the least critical thermal behavior. Even with repetition times of only 13ms no change in temperature could be observed.

Measurements for the thermal behavior have been performed as described in section 5.5. The results of these measurements are shown in figure 8.10.

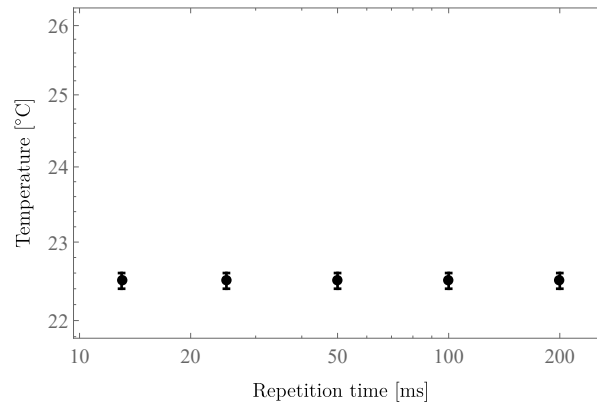


FIGURE 8.10: Thermal behavior of the DA-3DPR sequence as shown in a log-log plot.

8.5 Parameter Variation

8.5.1 Matrix Size in Reconstruction

As described before changing the size of the reconstruction matrix only affects the FOV and not the pixel size. This can be overcome by changing the “ t_0 ” setting, for more details see section 8.5.4.

To illustrate this effect the standard protocol image has been reconstructed with three different matrix sizes, the resulting images are shown in figure 8.11. This is the same acquisition each time, namely the standard protocol, figure 8.4.

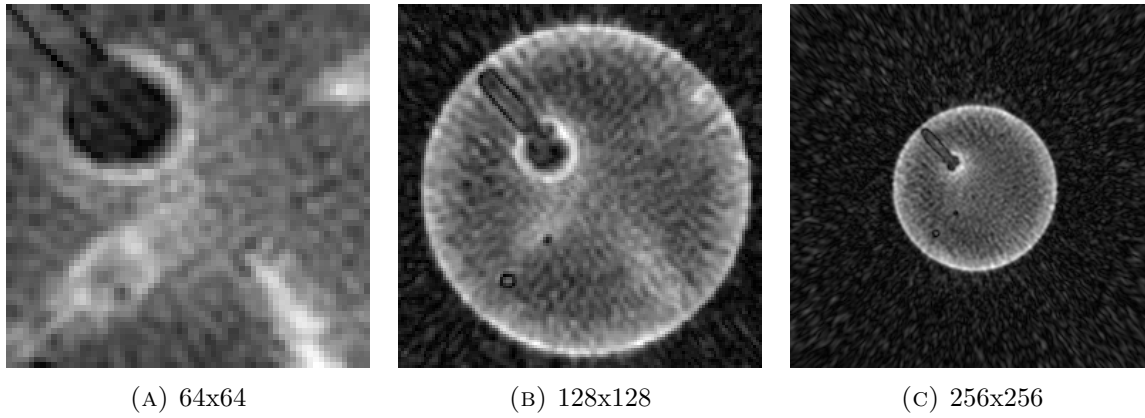


FIGURE 8.11: Different reconstruction matrix sizes in DA-3DPR.

8.5.2 Projections

Projections	Standard 3000	6000	12 000
SNR	6.053 ± 0.025	11.376 ± 0.08	17.86 ± 0.11
SNR _{corr}	3.965 ± 0.016	7.451 ± 0.053	11.701 ± 0.071
Resolution [μm]	$624. \pm 49.$	311.7 ± 6.6	281.1 ± 1.5
Edge overshoot [%]	210.5 ± 4.2	174.1 ± 3.4	$170.9 \pm 3.$
Diameter [mm]	33.22 ± 0.16	28.705 ± 0.016	28.61 ± 0.0052
Geometric error [%]	3.73 ± 0.18	1.19 ± 0.12	0.841 ± 0.012

Projections	30 000	50 000
SNR	18.759 ± 0.084	16.846 ± 0.058
SNR _{corr}	12.287 ± 0.055	11.034 ± 0.038
Resolution [μm]	284.7 ± 1.2	286.4 ± 1.1
Edge overshoot [%]	170.3 ± 3.1	197.8 ± 3.4
Diameter [mm]	28.5914 ± 0.0029	28.6387 ± 0.0023
Geometric error [%]	0.817 ± 0.015	0.85 ± 0.019

TABLE 8.3: DA-3DPR parameter variation with regard to projections.

The low number of projections in the standard protocol is a cause of many of the issues at hand.

Parameter variation measurements have been performed with more projections, the results of these measurements are shown in table 8.3.

It can be observed that all quality control parameters are increasing up to about 12 000 projections. After this point there is no further improvement or even a decline as for the signal to noise ratio in the 50 000 projections version.

This protocol with 12 000 projections is also the most comparable to the CV UTE sequence, as far as resolution parameters are concerned.

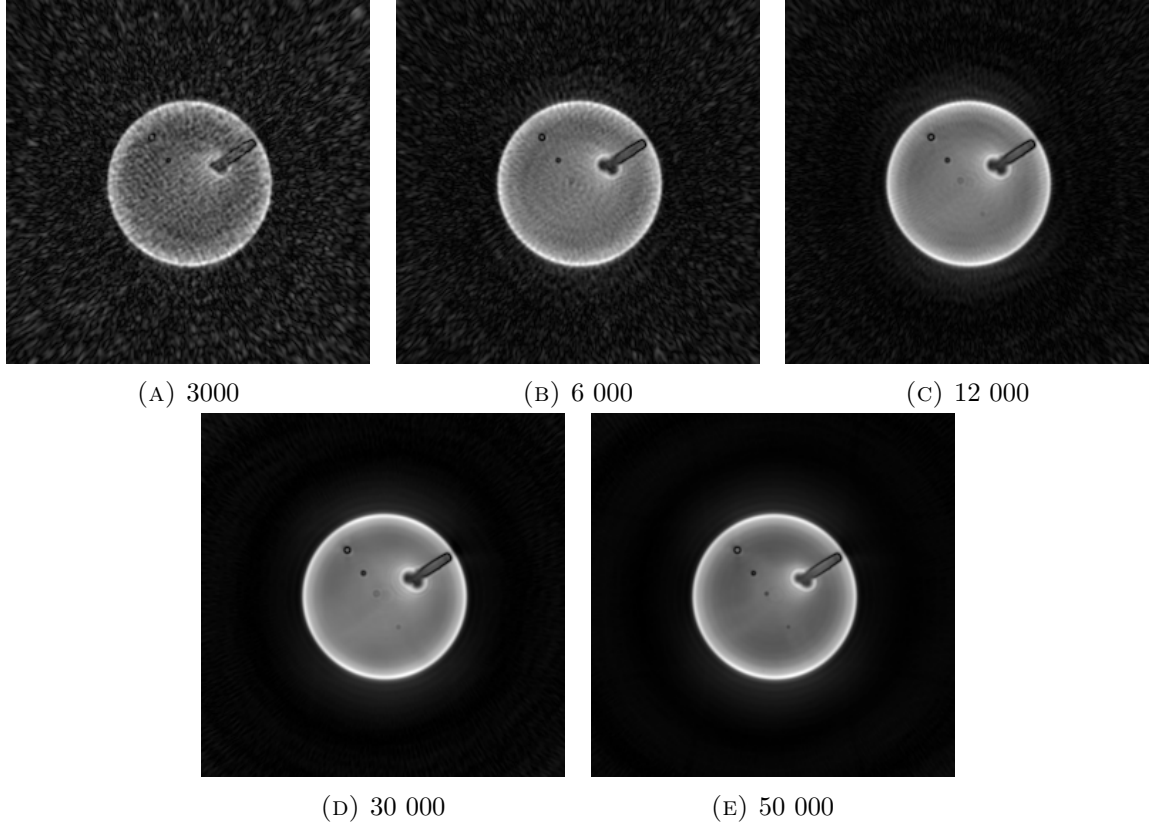


FIGURE 8.12: Comparison of different projection settings.

The images produced with the different projection settings, and the standard protocol, are shown in figure 8.12.

8.5.3 Pulse Duration

In this subsection the pulse duration setting[13, 44] which is available in this sequence has been varied.

Table 8.5 presents the results of this variations.

It can be observed that for both decreasing the pulse length to $250\mu s$ or increasing it to $750\mu s$ from the default value of $500\mu s$ a significant improvement can be achieved. With signal to noise ratios almost doubling and resolution also increasing.

When comparing the images acquired with these settings it becomes apparent that the k-space trajectory error based artefacts improve when changing this value. Figure 8.13 shows the resulting images side by side.

	250 μs	Standard 500 μs	750 μs
SNR	10.526 ± 0.056	6.053 ± 0.025	11.04 ± 0.058
SNR _{corr}	6.895 ± 0.037	3.965 ± 0.016	7.231 ± 0.038
Resolution [μm]	$523. \pm 22.$	$624. \pm 49.$	$490. \pm 17.$
Edge overshoot [%]	130.49 ± 0.82	210.5 ± 4.2	128.56 ± 0.95
Diameter [mm]	28.296 ± 0.044	33.22 ± 0.16	28.136 ± 0.043
Geometric error [%]	2.44 ± 0.33	3.73 ± 0.18	1.89 ± 0.36

TABLE 8.4: Parameter variation of the pulse duration.

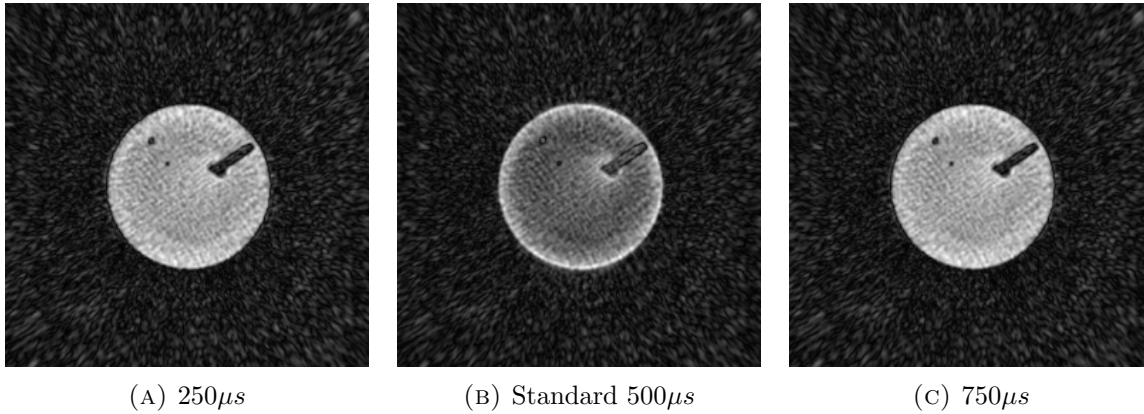


FIGURE 8.13: Comparison of different pulse duration settings.

The documentation provides the following information about this setting: “The pulse length of the excitation pulse can be adjusted according to the SAR requirements.” [44]

8.5.4 Pulse Sequence Timing - T_0

The t_0 setting is the time from gradient ramp up until the point where the gradient starts to ramp down again, including the plateau. [44]

This setting has been varied to two different settings from the default, as has been performed on the other settings.

It is this setting which achieves a change in pixel size and therefore field of view in the final image. Increasing this value decreases the pixel size and field of view in the reconstructed image, with the same reconstruction matrix size. This effect can be seen in figure 8.14.

	0.3ms	Standard	0.8ms
SNR	9.621 ± 0.082	6.053 ± 0.025	4.96 ± 0.023
SNR_{corr}	6.302 ± 0.054	3.965 ± 0.016	3.249 ± 0.016
Resolution [μm]	$501. \pm 16.$	$624. \pm 49.$	$775. \pm 48.$
Edge overshoot [%]	208.6 ± 1.8	210.5 ± 4.2	208.6 ± 3.1
Diameter [mm]	28.57 ± 0.017	33.22 ± 0.16	29.74 ± 0.022
Geometric error [%]	1.376 ± 0.042	3.73 ± 0.18	1.201 ± 0.074

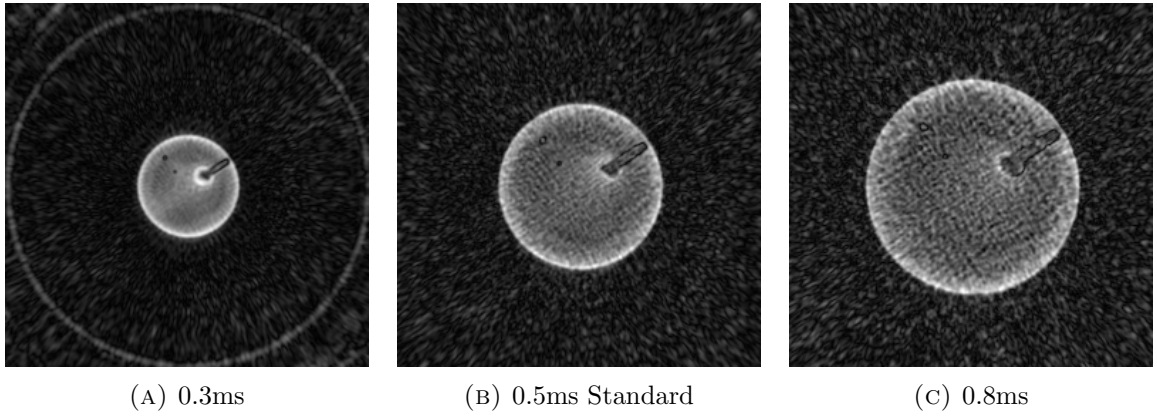
TABLE 8.5: Parameter variation of the T_0 pulse sequence timing setting.

FIGURE 8.14: Comparison of different pulse duration settings.

8.5.5 Settings Which Cause Execution Errors

Changing the gradient slew rate caused the sequence to fail to run. The same happens when changing other gradient settings.

8.6 Artefacts

Some of the artefacts can be explained by the low number of projections for the standard sequence. At higher projections there is some improvement while reaching an optimum at about 12 000 projections.

As this is the second sequence with radial k-space sampling it shows similar artefacts to the CV UTE sequence.

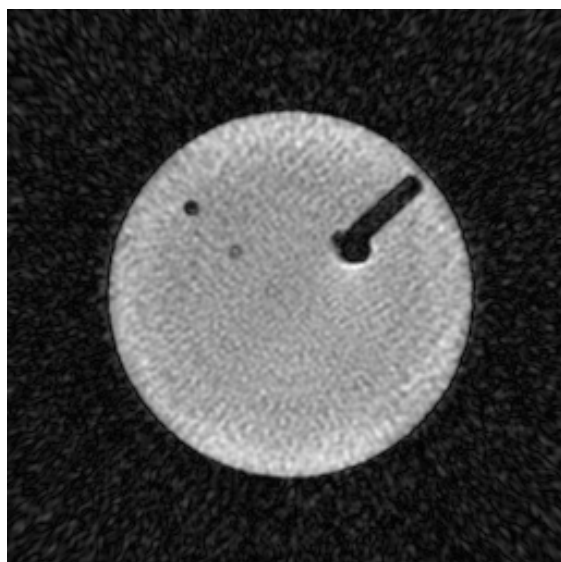
8.6.1 Blurring and Edge Enhancement

This sequence shows significant edge enhancement and blurring. The detailed mechanisms causing these phenomena are explained in section 3.2.

Some of this can be significantly reduced by choosing specific pulse durations, see subsection 8.5.3.

8.7 Improved Standard Protocol

Based on the findings discussed in the previous sections an improved standard protocol was defined. Flip angle and TR were still kept at less than optimal settings to allow direct comparison of these results with the ones from the other sequences.



TE	0.67 ms
TR	200 ms
Avg	1
FOV	(43.1 x 43.1) mm ²
BW	343.643 $\frac{Hz}{Px}$
Slice	168.5 μm
α	39°
Matrix	256 x 256
Proj.	6000
Voxel	(168.5 x 168.5 x 168.5) μm^3
Seq	DA-3DPR

FIGURE 8.15: Improved standard protocol for the DA-3DPR sequence.

The improved standard protocol is given in table 8.6.

Parameter	Value	Parameter	Value
TE	0.67 ms	BW	$343.643 \frac{Hz}{px}$
TR	200 ms	Avg	1
α	39°	Filters	none
FOV	(43.1 mm x 43.1 mm)	Voxel	(168x168x168) μm^3
Base	364	Spoil me	on
Reco Matrix	256x256	t_0	0.9 ms
Projections	6000	Pulse	750 μs

TABLE 8.6: DA-3DPR improved standard protocol.

Because of the non critical thermal behavior it would be highly advisable to use shorter TR times for this sequence in future measurements, allowing more projections and averages.

8.7.1 Signal to Noise Ratio using ROIs

Signal to noise ratio has been measured the same way as for the normal standard protocol.

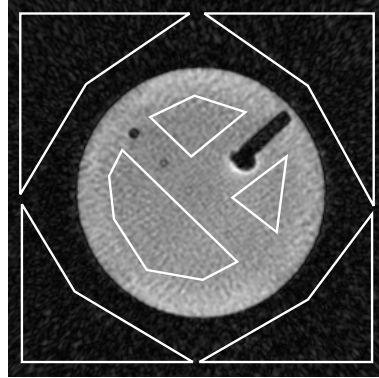


FIGURE 8.16: Regions of interest used for the SNR analysis in the DA-3DPR sequence improved standard protocol.

The signal to noise ratio measurement is based on 15 slices, the results for the single slices are $\{\frac{304.2}{21.9}, \frac{303.9}{22.}, \frac{304.}{22.5}, \frac{305.1}{21.7}, \frac{305.2}{21.9}, \frac{304.8}{21.9}, \frac{305.3}{21.8}, \frac{306.}{21.2}, \frac{306.1}{21.3}, \frac{306.3}{21.7}, \frac{307.}{22.}, \frac{307.8}{21.9}, \frac{308.6}{21.5}, \frac{309.5}{22.3}, \frac{310.2}{22.5}\}$ and the mean signal to noise ratio for the improved standard protocol is 14.008 ± 0.062 , with the corrected SNR being 9.175 ± 0.041 .

8.7.2 Signal to Noise Ratio using Difference Images

In this section the analysis of the signal to noise ratio using difference images, as defined in section 2.3.3, will be discussed.

This analysis has been performed on consecutive slices because only one measurement using the improved standard protocol was available. This is a deviation from the definition of this analysis in the NEMA standards[4].

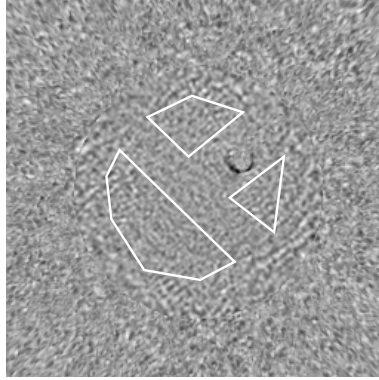


FIGURE 8.17: Difference image of two successive slices used for SNR calculation.

A difference image from this analysis and the ROIs used are shown in figure 8.17.

The result of this analysis was a SNR_{diff} of 20.79 ± 0.15 was obtained.

This results seams more reasonable than for the unmodified standard protocol.

8.7.3 Resolution

8.7.3.1 Edge Spread Function using MTF

Analysis of the resolution using the ESF-MTF method has been performed the same way as described for the normal standard protocol.

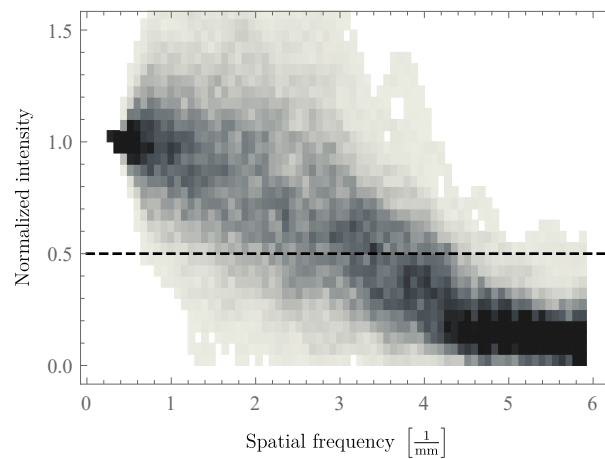


FIGURE 8.18: Modulation transfer function obtained from the ESF using numerical derivatives of the LSF for the DA-3DPR improved standard protocol. Showing a density histogram of 480 MTFs from 15 slices with bin widths of $0.08 \frac{1}{\text{mm}}$ in x direction and $0.05 \frac{1}{\text{mm}}$ in y direction.

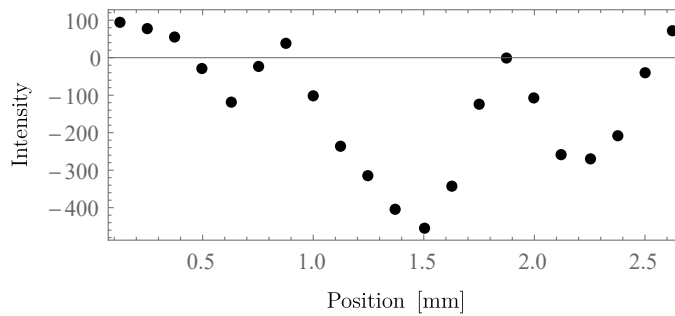
The modulation transfer function obtained from all slices and all lines is shown as a density histogram in figure 8.18.

Based on the edge spread function, using the ESF-MTF analysis method, a resolution of 446.5 ± 8.9 has been obtained.

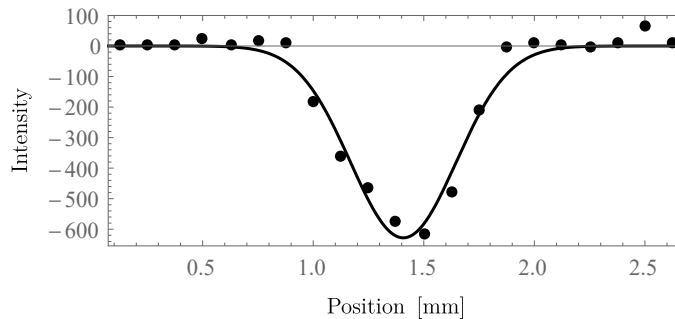
8.7.3.2 Point Spread Function using Gaussian Fits

An analysis was also performed using Gaussian fits and baseline correction as for the standard protocol. Fits were performed using `fityk`[10].

The analysis was performed based on the $(565.8 \pm 0.2)\mu m$ PSF phantom structure.



(A) Without baseline correction



(B) With fit and baseline correction

FIGURE 8.19: Line spread function obtained by integrating the PSF in x direction for the DA-3DPR improved standard protocol. Also showing one of the Gaussian fits used for the resolution analysis.

One of the line spread functions obtained by integrating the PSF in x direction is shown in figure 8.19.

The following FWHM were obtained by fitting after baseline correction: $\{561.8, 476.4, 689.8, 246.8, 753.8, 353.9\}\mu m$.

The resulting resolution based on these FWHM is $(514. \pm 80.)\mu m$. This is well within error margins of the ESF-MTF method and the phantom object size.

8.7.4 Edge Overshoot

Edge overshoot was also analyzed using the same methods as for the standard protocol, based on the Mathematica Analysis Toolkit, section 2.5.

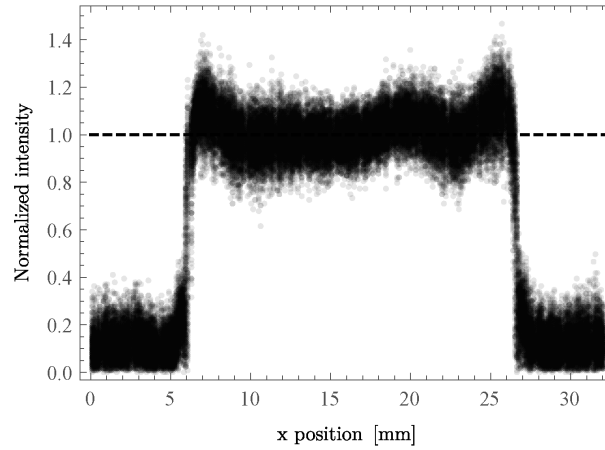


FIGURE 8.20: Line profiles of all lines used for the edge overshoot analysis in the DA-3DPR improved standard protocol. Normalized by dividing each line by the mean inside the edges.

All lines used for the edge overshoot analysis are shown in figure 8.20.

Based on this analysis the edge overshoot for the DA-3DPR improved protocol is $(126.28 \pm 0.45)\%$.

8.7.5 Results

All the results for the improved standard protocol are presented in table 8.7.

SNR	14.008 ± 0.062
SNR_{corr}	9.175 ± 0.041
SNR_{diff}	20.79 ± 0.15
Resolution, ESF [μm]	446.5 ± 8.9
Resolution, PSF Y [μm]	$514. \pm 80.$
Edge overshoot [%]	126.28 ± 0.45

TABLE 8.7: Measurement results for the DA-3DPR improved standard protocol.

The SNR_{corr} of 9.175 ± 0.041 is a significant improvement over the standard protocol with $SNR_{\text{corr}} = 3.965 \pm 0.016$ and edge overshoot of only $(126.28 \pm 0.45)\%$ for the improved protocol

compared to $(210.5 \pm 4.2)\%$ in the standard protocol. Resolution improved according to the ESF-MTF method with a resolution of $(446.5 \pm 8.9)\mu m$ in the improved protocol and $(565.8 \pm 0.2)\mu m$ in the standard protocol. The results of the PSF Gaussian fit method are equal to each other within error margins with $(514. \pm 80.)\mu m$ for the improved sequence and $(478 \pm 91)\mu m$ for the standard sequence.

8.8 Slice Thickness

Artefacts were too strong in all measurements for obtaining meaningful slice thickness values.

IMBA 15.2T

9.1 Introduction

Comparison measurements have been performed at an ultra high field strength 15.2T Bruker pre clinical imaging system.

These measurements have been performed in cooperation with the Institute for Molecular Biology of the Austrian Academy of Sciences. Thanks to Jelena Zinnanti and Lydia Zopf for making these measurements and therefore this part of this thesis possible.

All of these measurements have been performed using the phantom described in this thesis on the 24th of June 2015.

9.2 Analysis

The analysis was performed using the methods as laid out in chapter 2. Employing the custom developed Mathematica Analysis Toolkit, section 2.8. An additional module was developed to import the Bruker 2dseq data files.

Some problems were caused by the circular truncation in this sequences and therefore only very little noise data was left for the calculation of signal to noise ratios using the ROI method. This should be taken into account when considering the SNR and SNR_{corr} values calculated here.

To overcome this problem a second method of calculating the SNR, the NEMA difference images method was also used to analyze the SNR.

The extension of signal due to blurring into the noise area is somewhat mitigated by the fact that, as defined in equation 2.2, the standard deviation of the noise is used in this calculation instead of the mean value. [23]

9.3 Measurements

Two different sequences were available for the analysis of materials with very short T_2^* times. A Bruker UTE3D sequence and a zero TE sequence.

What is notable about both of these sequences is that they use a spherical field of view. Which causes the slices to be truncated in a circular pattern, with reducing radius as the position moves away from the center.

9.4 Bruker UTE3D

9.4.1 Sequence

The sequence used is a 3D UTE sequence. No sequence diagram is provided for this sequence in Brukers Paravision manual.[14]

A sequence diagram is provided for the 2D UTE sequence, this is similar to the one shown in figure 1.16, with gradient spoiling.

9.4.2 Measurement

A comparison measurement was performed with the goal of using protocol parameters which are as close as possible to the standard protocol parameters as defined in section 5.3.

Parameter	Value	Parameter	Value
TE	0.67 ms	BW	$305 \frac{Hz}{px}$
TR	10 ms	Avg	2
α	7°	Projections	205 000
FOV	(32 mm x 32 mm)	Polar undersampling	on
Matrix	256x256x256	TA	34m

TABLE 9.1: Parameters for the Bruker 15.2T comparison measurement.

The parameters chosen for the UTE sequence are printed in table 9.1.

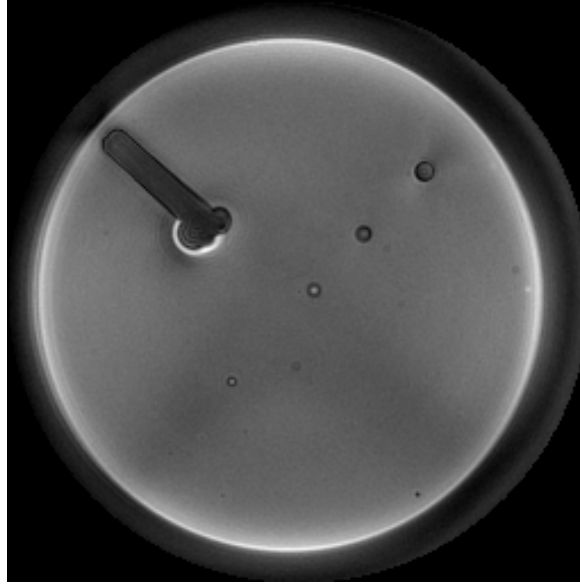


FIGURE 9.1: Bruker 15.2T UTE comparison measurement.

9.4.3 Signal to Noise Ratio using ROIs

Signal to noise ratio has been determined in two ways. The first one is the region of interest method, as described in section 2.3.

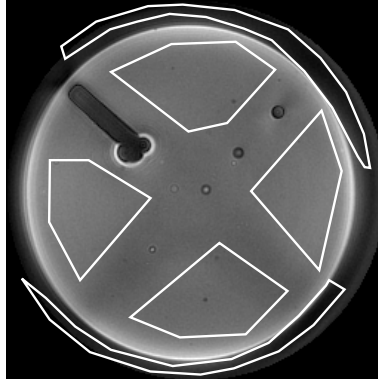


FIGURE 9.2: Regions of interest used for the SNR analysis in the Bruker UTE3D measurement.

The results of the single slices were $\left\{ \frac{8275.2}{910.8}, \frac{8250.4}{906.4}, \frac{8222.5}{905.8}, \frac{8187.9}{902.4}, \frac{8160.8}{897.7}, \frac{8138.}{890.3}, \frac{8113.4}{889.1}, \frac{8086.8}{886.}, \frac{8065.3}{878.3}, \frac{8036.}{880.3}, \frac{8011.6}{870.3} \right\}$, which results in a mean SNR obtained using the ROI method for the Bruker UTE3D sequence of 9.122 ± 0.013 and 5.9748 ± 0.0085 after correction.

9.4.4 Signal to Noise Ratio using Difference Images

As can be seen in figure 9.2 the regions of interest for the noise data are rather small and can thereby not be chosen in such a way that they are mostly artefact free, therefore this measure for the SNR is expected to yield better results.

Difference images of successive slices were calculated, based on these images the SNR_{diff} was calculated as described in section 2.3.3.

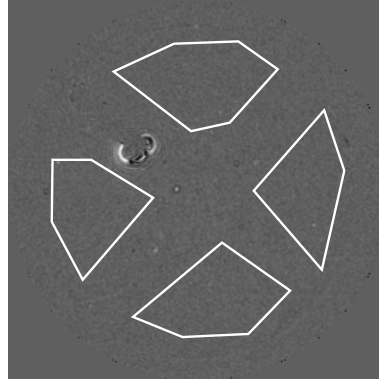


FIGURE 9.3: Difference image of two successive slices used for SNR calculation of the Bruker UTE3D measurement.

Figure 9.3 shows one of the difference images used for the analysis and the regions of interest used.

Five difference images were produced and used for the analysis.

The SNR obtained from difference images SNR_{diff} was calculated to be 26.67 ± 0.58 for the Bruker UTE3D sequence.

This is a very significant difference to the signal to noise ratio obtained from the ROI method, this result is far more trustworthy as the noise ROIs are very small and close to the phantom structure in the ROI method.

9.4.5 Resolution

9.4.5.1 Edge Spread Function using Modulation Transfer Function

Resolution analysis was performed using the ESF-MTF method, as described in section 2.4.1.

A smooth density histogram of the modulation transfer function, as obtained from the ESF using its derivative, the LSF, is shown in figure 9.4.

Based on this analysis this measurement of the Bruker UTE3D sequence has a resolution of $(544. \pm 17.)\mu m$.

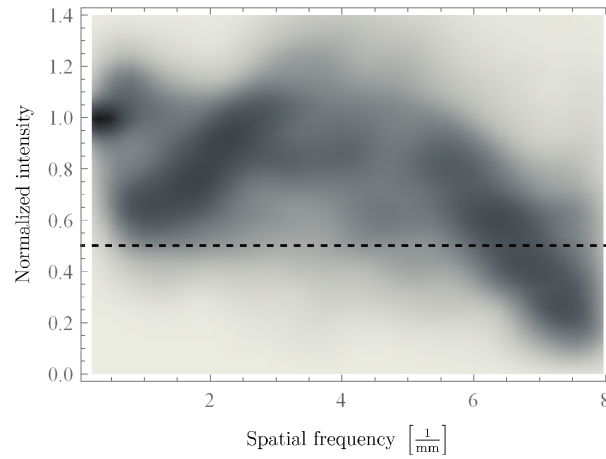


FIGURE 9.4: Modulation transfer function obtained from the ESF using numerical derivatives of the LSF for the Bruker UTE3D sequence. Showing a smooth density histogram of 484 MTFs. Please note that this plot is only provided to illustrate the shape of the MTF and was not used for the analysis of the resolution.

9.4.5.2 Point Spread Function using Gaussian Fits

Resolution has also been measured by fitting Gaussian functions into the integrated point spread function, the LSF. Before these fits were performed in `fityk`, a baseline correction was applied.

The $(204.8 \pm 0.2)\mu\text{m}$ phantom structure was used for this analysis.

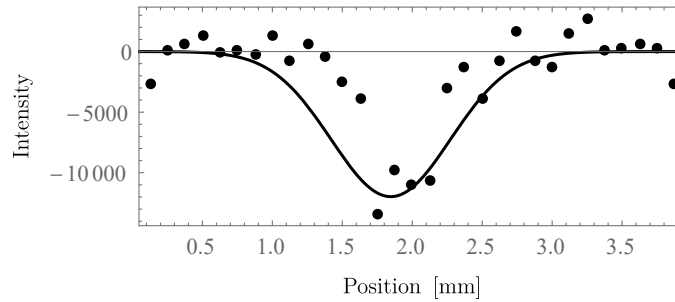


FIGURE 9.5: Point spread function analysis using Gaussian fits in Bruker UTE. Data points shown are without spline baseline subtraction but with constant baseline adjustment performed by subtracting the average of the data points left of the peak.

The Gaussian fits had FWHM of $\{600. \pm 530., 863. \pm 21., 379. \pm 18., 997. \pm 34., 870. \pm 37., 741. \pm 90., 1092. \pm 88.\}\mu\text{m}$.

Based on these results a monte carlo simulation[41] with an ensemble size of $12 \cdot 10^6$ members has been performed. The mean value of this simulation was used as the result and the standard deviation as the error.

As can be seen from the example fit in figure 9.5, the shape of the PSF, and therefore the shape of the LSF, is very complicated, and non Gaussian, making the fit less reliable and the result less trustworthy.

The result for this resolution analysis of the Bruker UTE3D sequence is $(790. \pm 310.)\mu m$.

9.4.6 Edge Overshoot

This analysis has been performed by obtaining line profiles from 14 different slices. Line profiles (in x direction) 119 through 136 (y direction) were used. Inside these line profiles an average inside the signal area was calculated from pixel 88 to pixel 170. The whole line profile was divided by this average. The maximum inside this line was used as the edge overshoot value. From all the line profiles a mean value was obtained. Furthermore a mean value of all these results in the 14 slices was obtained.

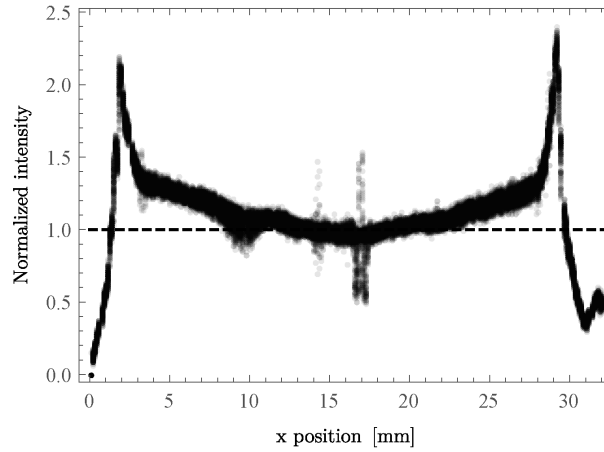


FIGURE 9.6: Line profiles of all lines used for the edge overshoot analysis in the Bruker UTE3D measurement. Normalized by dividing each line by the mean inside the edges.

All these line profiles are shown in figure 9.6.

This analysis resulted in an edge overshoot of $(224.2 \pm 1.7)\%$ in this Bruker UTE3D measurement.

9.4.7 Results

Results of the analysis of the measurement are shown in table 9.4.

SNR	9.122 ± 0.013
SNR _{corr}	5.9748 ± 0.0085
SNR _{diff}	26.67 ± 0.58
Resolution, ESF [μm]	$544. \pm 17.$
Resolution, PSF Y [μm]	$790. \pm 310.$
Edge overshoot [%]	224.2 ± 1.7
Diameter [mm]	28.557 ± 0.011
Geometric error [%]	1.198 ± 0.062

TABLE 9.2: Measurement results for comparison protocol of the Bruker 15.2T UTE sequence.

9.4.8 Artefacts

9.4.8.1 Blurring

As can be seen in, for example figure 9.1, blurring is visible in the image.

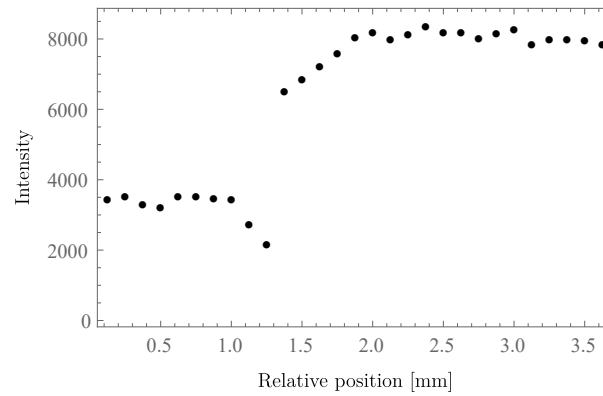


FIGURE 9.7: Edge spread function for the comparison measurement using the UTE sequence on the Bruker 15.2T system.

This blurring is also visible along the edge of the edge spread function, thereby reducing the resolution. As can be seen in figure 9.7.

9.4.8.2 Edge Enhancement

Edge enhancement is also quite considerable for the comparison sequence with an overshoot of $(224.2 \pm 1.7)\%$.

To illustrate this phenomenon a line profile from the comparison measurement, section 9.4, is shown in figure 9.8.

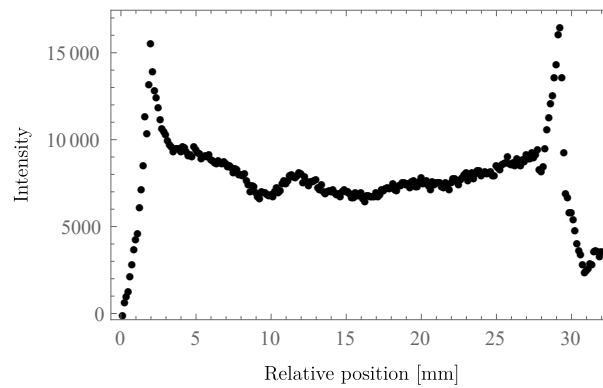


FIGURE 9.8: Line profile from a slice in the comparison measurement, figure 9.1, UTE on Bruker 15.2T.

9.5 Bruker ZTE

Measurements were also performed with the provided ZTE sequence.

9.5.1 Sequence

The Bruker ZTE sequence offers measurements with zero echo time, it uses non selective excitation with a constant gradient during excitation and acquisition.

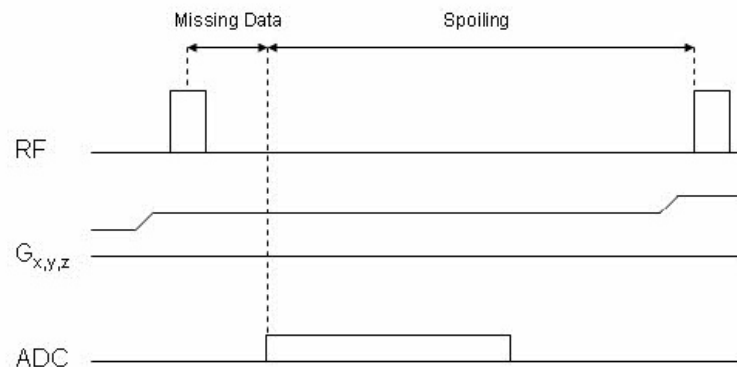


FIGURE 9.9: Bruker ZTE sequence diagram.
Image source: Bruker, Paravision 6.0 manual[14]

Bruker has two different sequence diagrams in its Paravision manual, these measurements were performed with the “GradOff=No” option set and the correct sequence diagram for this option is shown in figure 9.9.

9.5.2 Measurement

The settings used in this measurement are shown in table 9.3.

Parameter	Value	Parameter	Value
TR	10 ms	BW	$390 \frac{\text{Hz}}{\text{px}}$
α	7°	Avg	1
FOV	(32 mm x 32 mm)	Projections	100 000
Matrix	256x256x256	Polar undersampling	on
Pulse length	0.0128ms		
Pulse sharpness	3		

TABLE 9.3: Parameters for the Bruker 15.2T comparison measurement.

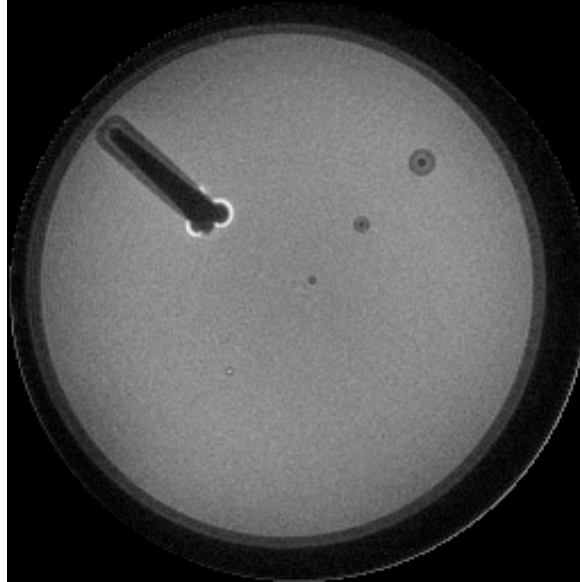


FIGURE 9.10: Bruker 15.2T zero TE measurement.

9.5.3 Signal to Noise Ratio using ROIs

SNR has been analyzed using the ROI method. This analysis used 11 slices.

The results for the slices are $\{\frac{7570.}{466.2}, \frac{7573.2}{459.3}, \frac{7562.9}{467.7}, \frac{7566.2}{467.1}, \frac{7555.1}{466.4}, \frac{7555.3}{474.9}, \frac{7550.8}{464.6}, \frac{7548.3}{471.8}, \frac{7538.7}{473.6}, \frac{7543.3}{469.}, \frac{7538.3}{478.6}\}$, this results in a SNR based on the ROI method for the Bruker ZTE sequence of 16.11 ± 0.062 and a SNR after correction of 10.552 ± 0.041 .

The regions of interest used for this analysis are shown in figure 9.11.

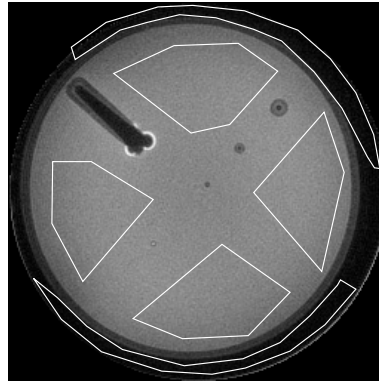


FIGURE 9.11: Regions of interest used for the SNR analysis in the Bruker ZTE measurement.

9.5.4 Signal to Noise Ratio using Difference Images

Due to the small noise region of interest available in these images a second method of calculating the signal to noise ratio has been applied. This method is described in more detail in section 2.3.3.

The same regions of interest as for the signal area in the ROI bases SNR calculation were used, figure 9.12.

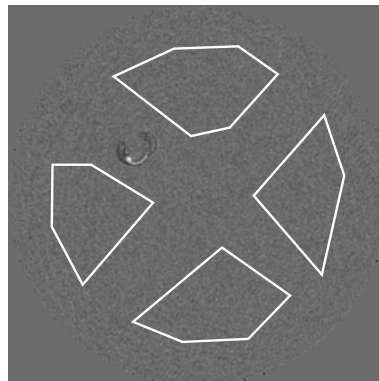


FIGURE 9.12: Difference image of two successive slices used for SNR calculation.

As only one measurement was available for this sequence neighbouring slices were used to produce the difference images, all even numbered slices were subtracted from the odd numbered slices, the mean signal was always obtained from the odd numbered slice. In total 11 slices were used for this analysis, yielding 5 difference images.

Using this method a SNR_{diff} of 27.43 ± 0.11 was obtained.

9.5.5 Resolution

9.5.5.1 Edge Spread Function using Modulation Transfer Function

This analysis was performed by obtaining the Fourier transform of the line spread function which was obtained by calculating the numerical derivative of the edge spread function.

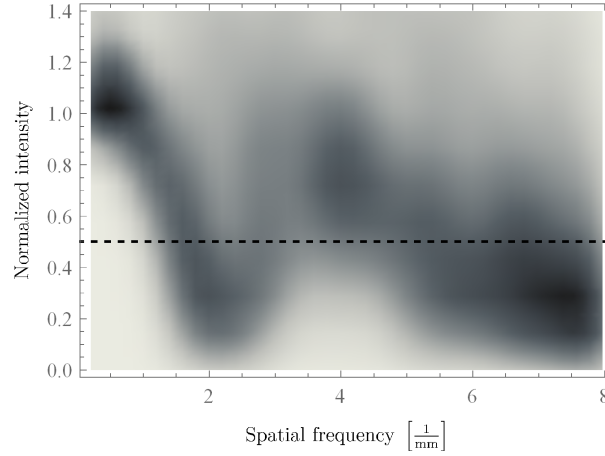


FIGURE 9.13: Modulation transfer function obtained from the ESF using numerical derivatives of the LSF for the Bruker ZTE sequence. Showing a smooth density histogram of 484 MTFs.

Based on the data in all slices a modulation transfer function smooth density histogram has been calculated and is presented in figure 9.13.

Using the ESF-MTF method a resolution of $(551.7 \pm 5.8)\mu\text{m}$ has been measured for this measurement using the Bruker ZTE sequence.

The second dip in the MTF is caused by the special kind of artefacts in this measurement as explained in section 9.5.8.

9.5.5.2 Point Spread Function using Gaussian Fits

An additional analysis of the resolution has been performed using Gaussian fits of the point spread function.

For this analysis baseline correction and Gaussian fitting have been performed in `fityk`[10].

The $(204.8 \pm 0.2)\mu\text{m}$ phantom structure was used for this analysis.

One of the data sets and fits obtained from that data set are shown in figure 9.14.

A good fit could not be achieved for all slices, but the following FWHMs could be determined from Gaussian fits: $\{421. \pm 19., 452. \pm 80., 784. \pm 64., 418. \pm 24., 1000. \pm 250., 600. \pm 150.\}\mu\text{m}$.

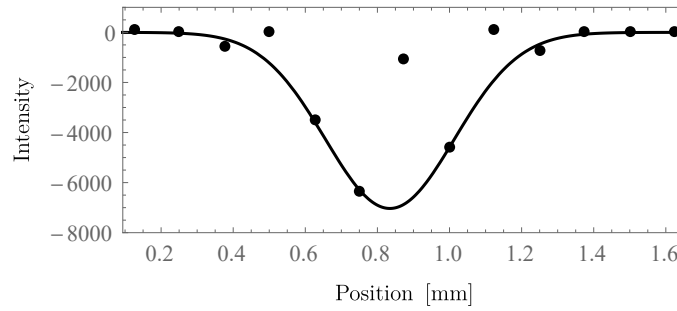


FIGURE 9.14: Point spread function analysis using Gaussian fits in Bruker ZTE. Data points shown are without spline baseline subtraction but with constant baseline adjustment performed by subtracting the average of the data points left of the peak.

Using a monte carlo simulation, with an ensemble size of $12 \cdot 10^6$, the mean value and error based on the ensembles standard deviation were obtained.

The resolution for the Bruker ZTE sequence using PSF-Gaussian analysis is $(610. \pm 260.)\mu\text{m}$.

9.5.6 Edge Overshoot

Edge overshoot analysis has also been performed using the Mathematica Analysis Toolkit.

A mean value inside the signal region has been calculated for each line profile, the line profile was normalized using this value and the maximum for the whole line profile was used as the edge overshoot of this line. This analysis has been repeated for multiple lines inside each slice and for multiple slices. A mean value and standard error have been calculated from these values. The same lines and pixel positions as for the Bruker UTE3D have been used.

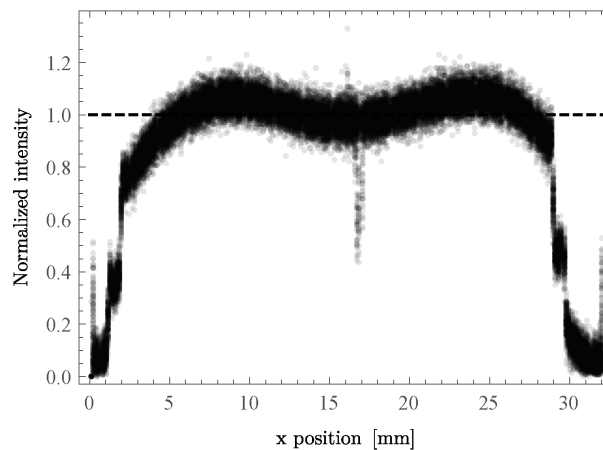


FIGURE 9.15: Line profiles of all lines used for the edge overshoot analysis in the Bruker ZTE measurement. Normalized by dividing each line by the mean inside the edges.

All the 198 lines used in this analysis are shown in figure 9.15.

As can be seen from this figure there is no overshoot on the outside edges. The edge enhancement artefact in this case is realized as a reduction of signal along the edges, this will be discussed in further detail in section 9.5.8. Therefore no edge overshoot value has been obtained for this measurement.

9.5.7 Results

Results of this acquisition are shown in figure 9.10. The parameters in table 9.3 were used for this measurement.

SNR	16.11 ± 0.062
SNR _{corr}	10.552 ± 0.041
SNR _{diff}	27.43 ± 0.11
Resolution, ESF [μm]	551.7 ± 5.8
Resolution, PSF Y [μm]	$610. \pm 260$
Diameter [mm]	28.946 ± 0.042
Geometric error [%]	4.349 ± 0.062

TABLE 9.4: Measurement results for comparison protocol of the Bruker ZTE sequence.

9.5.8 Artefacts

This sequence has some strong edge artefacts, in which signal drops around the edges. Edge enhancement can also have this effect of signal dropout. The difference in signal along the lines marked with arrows in figure 9.16 have no physical explanation and are similar along all edges. The edge spread function phantom structure is made of the same material throughout and while the lower signal along the outside would make sense due to a different material being used there, it would not match the outside of the phantom based on the total diameter. The two largest phantom structures are glass capillaries, therefore it would also seem highly doubtful that those are visible in this measurement. which appear more sharply delineated than the edge enhancements encountered in the other UTE sequences in this thesis. See figure 9.10.

A line profile was taken from a purely circular part of the phantom, containing no structures and is shown in figure 9.17.

This artefact is not properly described by the edge overshoot quantity but leads to a worse resolution of only $(975.8 \pm 9.8)\mu m$. It can be seen in figure 9.10 that this artefact also has a significant impact on the shape of the point spread function.

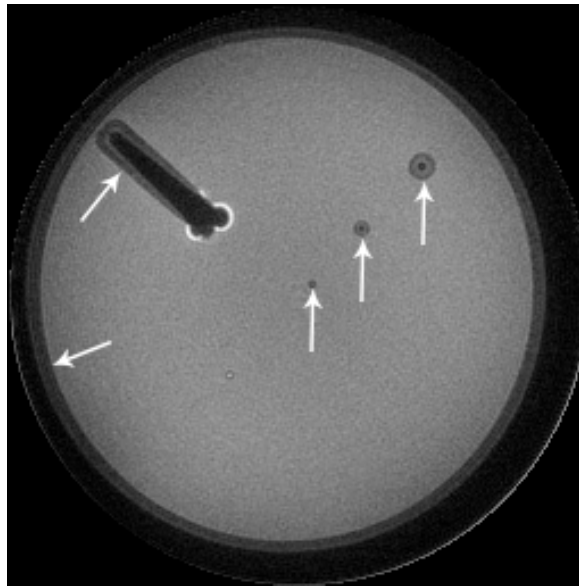


FIGURE 9.16: Edge artefact in which the edge has a lower signal around its corner in the Bruker ZTE sequence.

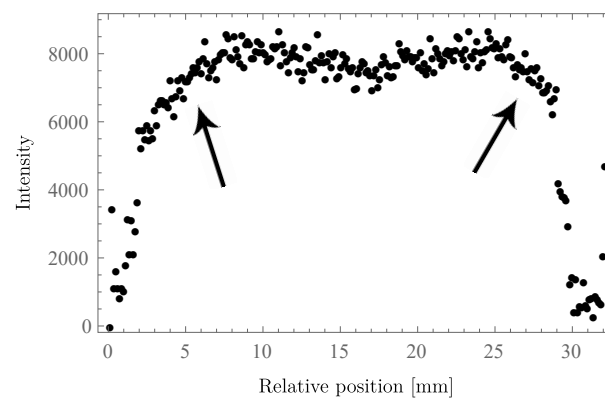


FIGURE 9.17: Line profile from a circular part of the slice in the Bruker 15.2T ZTE sequence, taken from figure 9.10.

Results

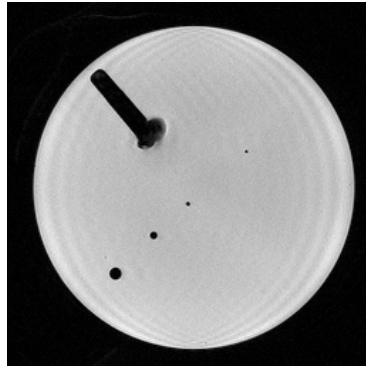
10.1 Reliability of Results

Due to the strong and sometimes severe artefacts in these measurements a color coded system for rating the reliability and trustworthiness of each of the results has been established.

This system will be used in the charts in this chapter. The grading system goes from 1 through 4, where 1 is a highly unreliable result and 4 is a highly reliably result, an overview of the grading system used is given in table 10.1.

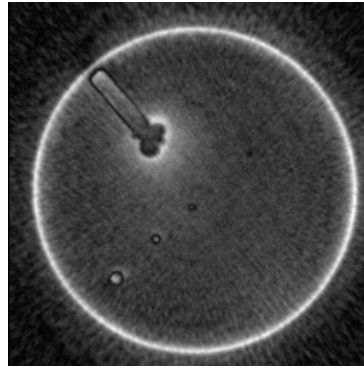
4	Highly reliable. The result is based on intermediate data which seem very reliable, the analysis module has been verified, the result confirms to results obtained from other methods. Evidence is generally good for this result.
3	Reliable. This result has been obtained from input data which seems trustworthy. The intermediate data seems sound and it confirms to general expectations for the data input.
2	Unreliable. The result seems unreliable due to the intermediate results, strong artefacts, unconfirmed method, etc.
1	Highly unreliable. The result seems wrong, the intermediate data seems to not be meaningful, this result is in stark contradiction to other results which are more reliable.

TABLE 10.1: Overview of the grading system for result reliability.



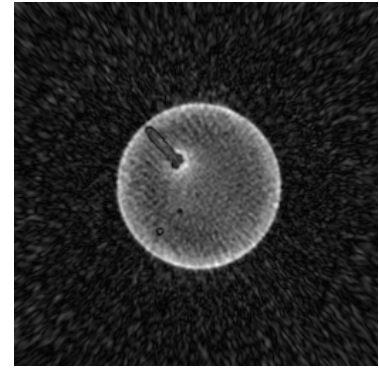
TE	0.67 ms
TR	200 ms
Avg	3
FOV	(32. x 32.) mm ²
BW	300 $\frac{Hz}{Px}$
Slice	400 μm
α	39°
Matrix	256 x 256
Voxel	(125. x 125. x 400.) μm^3
TA	20:33

(A) XD VTE



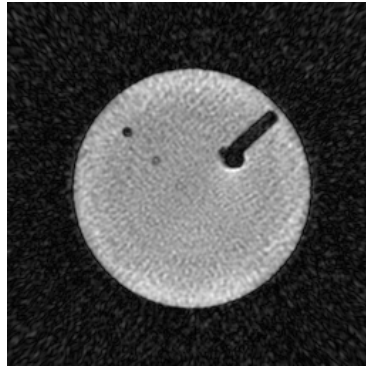
TE	0.67 ms
TR	200 ms
Avg	2
FOV	(32. x 32.) mm ²
BW	300 $\frac{Hz}{Px}$
Slice	125. μm
α	39°
Matrix	256 x 256
Voxel	(125. x 125. x 125.) μm^3
TA	21:45

(B) CV UTE



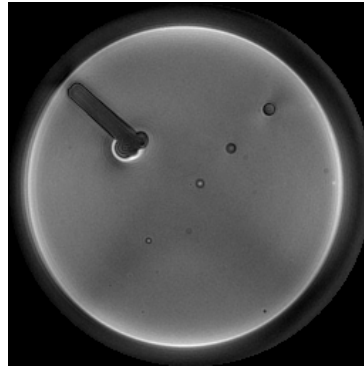
TE	0.67 ms
TR	200 ms
Avg	2
FOV	(62.7 x 62.7) mm ²
BW	343.643 $\frac{Hz}{Px}$
Slice	244.9 μm
α	39°
Matrix	256 x 256
Proj.	3000
Voxel	(244.9 x 244.9 x 244.9) μm^3

(C) DA-3DPR



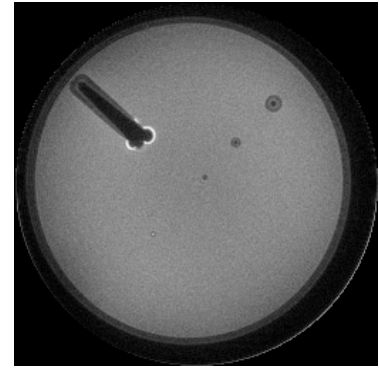
TE	0.67 ms
TR	200 ms
Avg	1
FOV	(43.1 x 43.1) mm ²
BW	343.643 $\frac{Hz}{Px}$
Slice	168.5 μm
α	39°
Matrix	256 x 256
Proj.	6000
Voxel	(168.5 x 168.5 x 168.5) μm^3

(D) DA-3DPR improved



TE	0.67 ms
TR	10 ms
Avg	2
FOV	(32.0 x 32.0) mm ²
BW	305 $\frac{Hz}{Px}$
Slice	125 μm
α	7°
Matrix	256 x 256 x 256
Proj.	205 000
Voxel	(125 x 125 x 125) μm^3

(E) Bruker UTE3D



TR	10 ms
Avg	1
FOV	(32.0 x 32.0) mm ²
BW	390 $\frac{Hz}{Px}$
Slice	125 μm
α	7°
Matrix	256 x 256 x 256
Proj.	100 000
Voxel	(125 x 125 x 125) μm^3
Pulse length	0.0128ms

(F) Bruker ZTE

FIGURE 10.1: Standard protocols for the XD VTE, CV UTE and DA-3DPR sequences and images acquired using these standard protocols. Images acquired for the comparison with the 15.2T pre clinical imaging system using the Bruker UTE3D and Bruker ZTE sequences and the parameters used in those sequences.

10.2 Standard Protocols

Standard protocols have been defined for the XD VTE, CV UTE and DA-3DPR sequences with the goal of obtaining measurements which are as comparable as possible. The total acquisition time was chosen as the primary optimization criterion and set to be 20min.

For the DA-3DPR sequence a second, improved standard protocol, has been defined implementing improvements from insights gained during this investigation.

Further details on how the standard protocols were defined can be found in section 5.3.

The standard protocols defined for the XD VTE, CV UTE and DA-3DPR sequences are shown in figure 10.1.

10.3 Resolution

Two different methods were used to determine the resolution. The first one will be called the **ESF** method and describes the method of obtaining a modulation transfer function (MTF) by calculating the numerical derivative of the edge spread function (ESF), the line spread function (LSF). Details are provided in section 2.4.1.

The resolution limit definition for the MTF was chosen at 50%.

The second method will be referred to as the **PSF Y** method. In this method the point spread function (PSF) was integrated in y direction in order to obtain the line spread function (LSF) in x direction. This LSF was then analyzed by performing a baseline correction and Gaussian fit in fityk[10]. This was repeated for multiple slices and the mean and standard error were calculated.

Results for the different standard protocols are shown in figure 10.2.

The best results of all the standard protocols were obtained for the XD VTE sequence with resolutions down to $(205.5 \pm 1.8)\mu m$ (ESF) / $(203 \pm 33)\mu m$ (PSF Y). This sequence has a very short echo time but not an ultra short echo time, unlike all the other sequences in this thesis.

For the UTE sequences the best resolutions were achieved with the improved DA-3DPR protocol, $(446.5 \pm 8.9)\mu m$ (ESF) / $(514 \pm 80)\mu m$ (PSF Y). Within error margins the DA-3DPR standard protocol is close by, but this result is also less reliable. One problem is that with the strong artefacts present in all the UTE sequences and the ZTE sequence all these resolution results are rather unreliable.

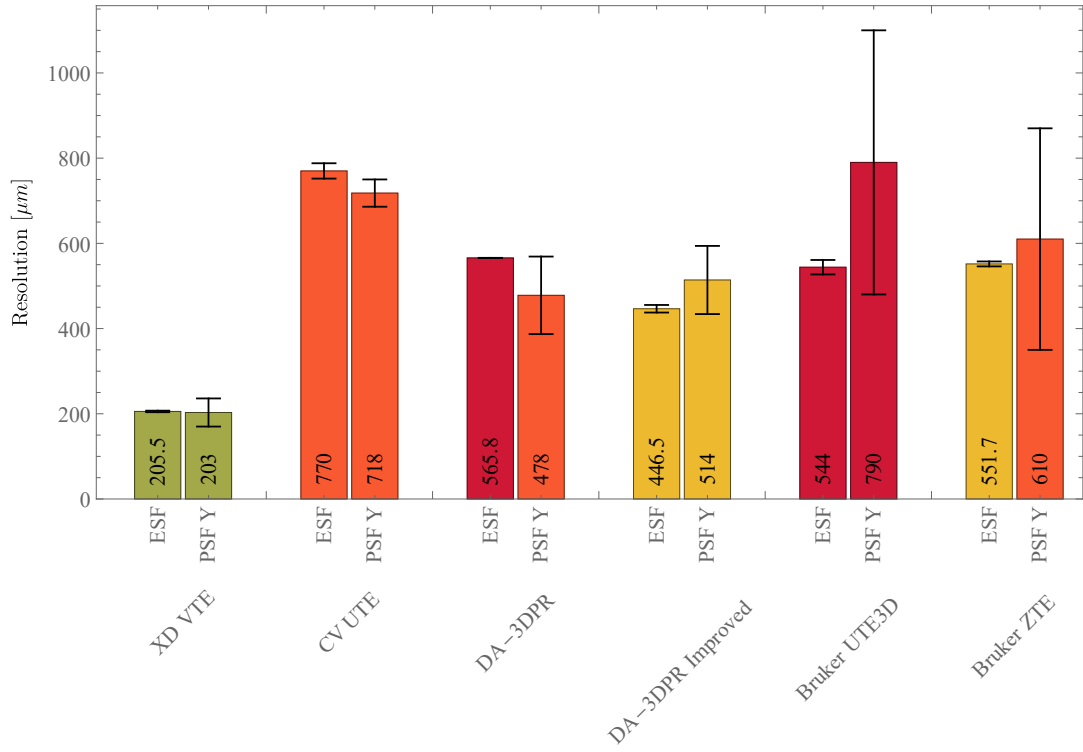


FIGURE 10.2: Resolution results for the different standard protocols in this thesis. The color of the bars refers to the reliability of each measurement as provided in table 10.1. ESF is the ESF-MTF method. PSF Y is the Gaussian fits on the LSF in y direction from PSF integration in x direction method. Please note that two graphs have errors so small that the error bars are not visible. Pixel sizes for the XD VTE, CV UTE, Bruker UTE3D and Bruker ZTE are $125\mu\text{m}$, the DA-3DPR standard protocol has a pixel size of $244.9\mu\text{m}$ and the DA-3DPR improved protocol pixel size is $168\mu\text{m}$.

It is also noteworthy that the 15.2T pre clinical imaging system did not achieve a higher resolution than the 7T wholebody system with microgradient insert.

The highest resolution of $(103.02 \pm 0.8)\mu\text{m}$ was achieved in the high resolution overnight measurement using the XD VTE sequence. For more details see section 6.6.

10.4 Signal to Noise Ratio

Please note that these measurements have not been performed with exactly the same settings. Signal to noise ratios should therefore not be directly compared on a quantitative basis and charts showing all the results on one figure are just placed here to provide a better overview to the reader.

Two different methods were used for analyzing the signal to noise ratios (SNR) in the investigated images.

The automated analysis used for all the parameter variations was the **ROI** method. This SNR is shown in result tables as SNR_{corr} . It is based on the region of interest method whereby the mean signal inside the signal ROIs is divided by the standard deviation inside the noise areas. This value has also been corrected for the Rician distribution of the noise by multiplying the result with a correction factor of 0.665.

The second method applied was the difference images method, based on the NEMA standards[4]. Abbreviated as “**Diff**”. This method is based on the calculation of difference images from two consecutive measurements which need to be performed with the same system calibration. ROIs are set inside the signal area. The mean signal inside these ROIs, obtained from the first image, is divided by the standard deviation inside the ROI of the differences image. This standard deviation also has to be corrected for the fact that the noise was obtained by a subtraction operation. This is done by dividing the standard deviation value by $\sqrt{2}$.

Two consecutive measurements were not available for all measurements, for these a slightly different procedure has been applied of using consecutive slices. These results are marked with a “*” in figure 10.3.

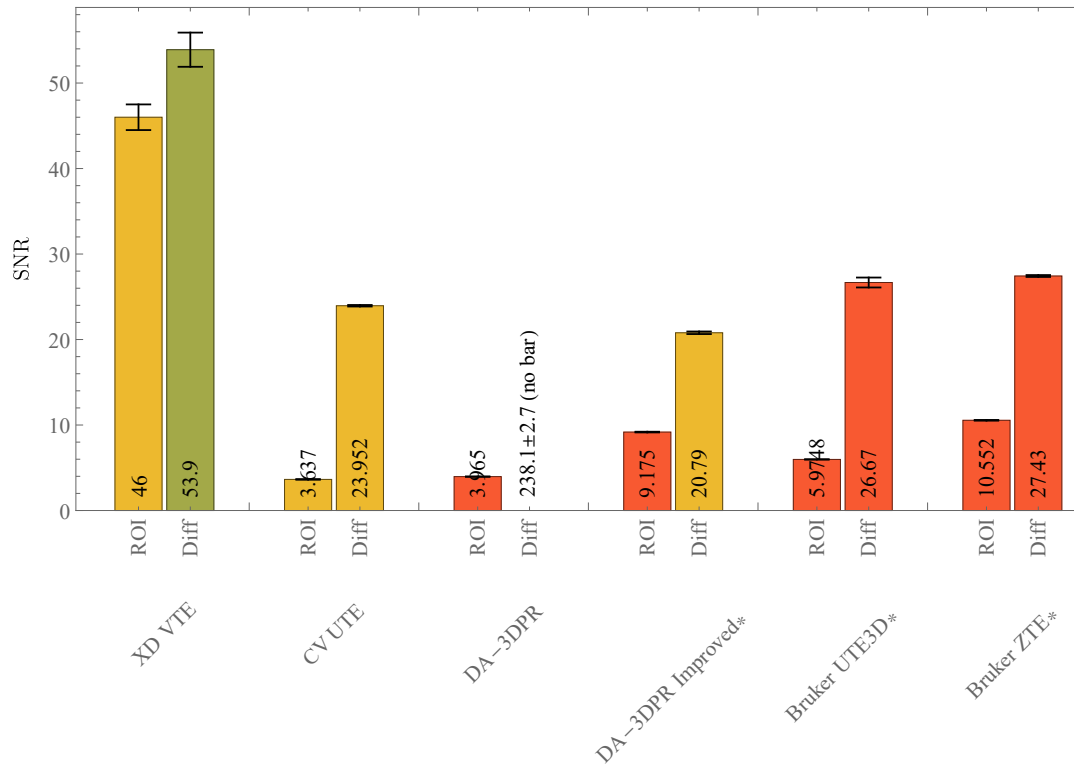


FIGURE 10.3: Signal to noise ratio results. Two different methods, ROI and Diff are shown. These are the region of interest method and the difference images method. For all values marked with a “*” the difference image has been obtained using consecutive slices instead of different measurements.

Figure 10.3 shows all the SNR values obtained, except for the SNR_{diff} value of the DA-3DPR standard protocol of 238.1 ± 2.7 . Including this measurement would have negatively impacted the readability of this chart because it is much larger than all the other SNR results which would have made all the other bars very small and therefore hard to compare to each other.

The SNR results are not directly comparable, but all the UTE sequences show similar performance, when looking at the difference image method based results. When looking at the ROI based results the CV UTE sequence performs worse than the other sequences.

The large differences between the ROI and difference images methods can be explained by the fact that the artefacts play a far larger role in the ROI method. In the case of the ROI method artefacts which are present outside of the signal area contribute to the overall noise level. These same artefacts are mostly canceled out in the differences method. This is also visible in the difference images in this thesis, figures 6.3, 7.3, 8.6, 8.17, 9.3 and 9.12.

The question remains which method of defining the signal to noise ratio is more useful. Arguments for both can be made and there is value in having the artefacts, which are ultimately present in the final image, to also be represented in the SNR measure.

Overall the best SNRs for the standard protocols were achieved in the XD VTE sequence.

10.5 Edge Overshoot and Ringing

Edge overshoot and ringing were quantified by taking multiple x direction line profiles, obtaining the mean value inside the non affected signal intense area and normalizing the whole profile to this mean value. The edge overshoot was then measured by taking the maxima of each of the line profiles and calculating a mean of these results. This process was repeated for multiple slices, for details see section 2.5.

A value of 100% would be a perfect, indicating that there is no overshoot along the edges of the phantoms.

Figure 10.4 shows the results for different sequences and protocols. 100% would be the optimal value, corresponding to no artefacts.

The Bruker ZTE shows no edge overshoot but has a different kind of edge enhancement artefact resulting in reduction of signal along the edge. This is explained in more detail in section 9.5.8. For this reason the Bruker ZTE sequence is not included in figure 10.4.

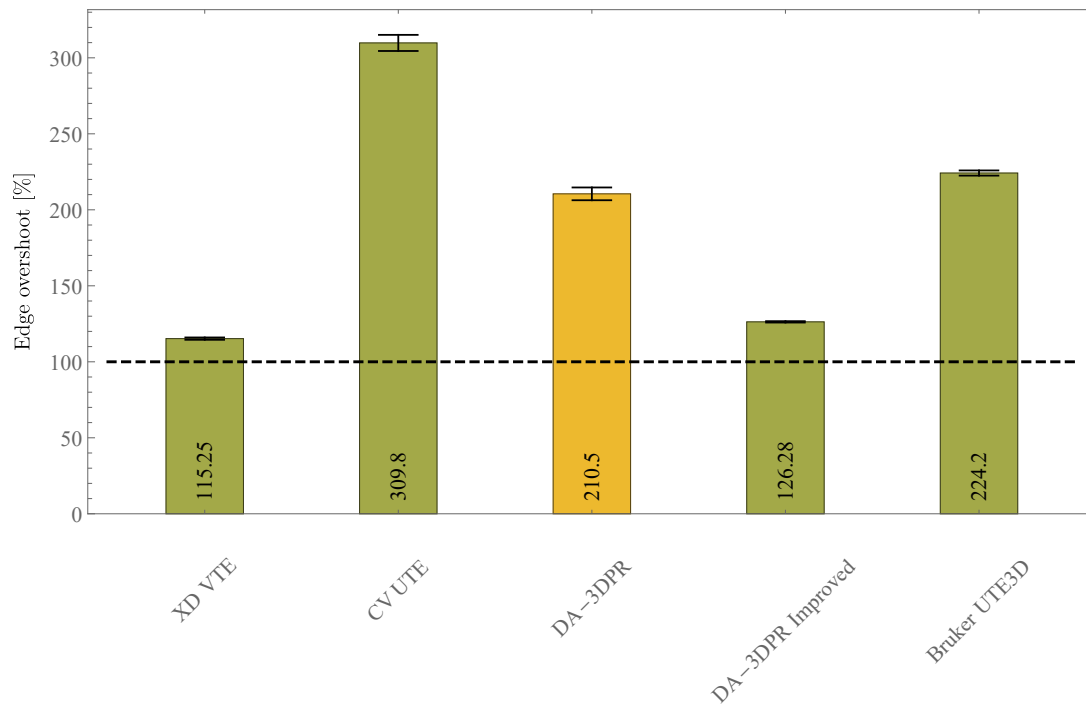


FIGURE 10.4: Edge enhancement and ringing results. 100% means that there is no overshoot and this would be the ideal situation. The artefact described in the XD VTE sequence is best understood as ringing, or a mixture of ringing and edge enhancement. The other overshoots along the edge are due to edge enhancement.

In this analysis the XD VTE sequence shows the least artefacts with an edge overshoot of only $(115.25 \pm 0.76)\%$. But the improved DA-3DPR protocol performs only a little bit worse on this measure with edge overshoot of $(126.28 \pm 0.45)\%$ and is a UTE sequence.

The strongest edge enhancement artefacts were visible in the CV UTE overnight measurements with values of up to $(702.8 \pm 4.4)\%$. See section 7.7 for more details.

Conclusions & Outlook

Artefacts remain a major issue with UTE, ZTE and VTE sequences. While the VTE sequence had the longest minimum TE it also achieved the best results. These artefacts are primarily caused by non ideal gradient performance and the resulting k-space trajectory errors. Corrections which can improve these artefacts have been implemented before[2, 3] but are not readily available to users of UTE sequences.

Within the scope of this thesis no such corrections could be implemented and the images therefore showed very strong artefacts.

When measurements are considered where echo times of about 0.67ms are sufficient, the XD VTE sequence clearly provides the best performance, with the relatively lowest artefacts shown. With this XD VTE sequence resolutions of up to $(103.02 \pm 0.8)\mu m$ at a pixel size of $62.5\mu m$ were achieved. This resolution was measured based on the edge spread function by obtaining the numerical derivative of the ESF which yields the line spread function and analyzing the LSF by obtaining the MTF using a discrete Fourier transformation. The resolution limit was set to 50% modulation in the MTF.

The highest resolution achieved using UTE sequences was $(446.5 \pm 8.9)\mu m$ (ESF) / $(514 \pm 80)\mu m$ (Point spread function, Gaussian fit FWHM) at a pixel size of $125\mu m$.

If TEs below 0.5ms are necessary only the CV UTE, DA-3DPR, Bruker UTE3D or Bruker ZTE can be used. The last two sequences are not available on the 7T whole body scanner. These provided minimum TEs down to 0.07ms.

The major issue with the UTE and ZTE sequences are edge enhancement and blurring artefacts, most likely caused by shifts in k space, section 3.2.

These severely limit the usefulness of the CV UTE sequence and the resolutions achieved were in the order of the resolution of its standard protocol, $(770. \pm 18.)\mu m$. At signal to noise ratios of only 5.553 ± 0.053 , and SNR_{corr} of 3.637 ± 0.035 .

This sequence might also be more useful for objects which have very few lower spatial frequencies. Therefore performance for highly detailed objects without larger signal intense areas might be far better. As lower k-space frequencies are distorted the most.[2]

Edge enhancement causes overshoots along the edge of up to $(309.8 \pm 5.3)\%$, for the standard protocol of the CV UTE sequence. The DA-3DPR sequence is the best performing UTE sequence in this regard with overshoots of $(126.28 \pm 0.45)\%$.

Some filters can improve the final image quality obtained, but none of the filters or settings were able to improve the low resolution due to artefacts.

The second option available for UTE imaging on this micro gradient system is the DA-3DPR sequence with minimum detection times of 0.08ms. It provides the least comfortable user experience, placing the measurement always in the isocenter, no online reconstruction and more complicated parameters for set up of the field of view size and measurement. But it also shows the most promising performance with extensive tuning.

With this DA-3DPR sequence quite a few initial problems were encountered when performing measurements, and some files failed to reconstruct in a meaningful way.

Highest resolution achieved for the DA-3DPR sequence was $(446.5 \pm 8.9)\mu m$ (ESF-MTF), at a pixel size of $168\mu m$, using the improved standard protocol, with further tuning of parameters and optimizing the measurements, higher resolutions might be achievable on this system. This process proves very tedious as the results of ones actions can not be seen immediately and the impact of different settings is sometimes not quite clear. The signal to noise ratios for this measurement were 9.175 ± 0.041 according to the ROI method and 20.79 ± 0.15 according to the difference images method[4].

As far as geometric accuracy is concerned, it can be observed that both the CV UTE and DA-3DPR sequences cause objects to appear slightly larger than they really are due to edge enhancement, but don't cause any significant distortions in the shape of these objects. The

XD VTE sequence provides the most accurate measurements of structure size. The diameter analysis measure overestimates this effect as the signal inside the signal intense area is very low and the 50% threshold of this mean value, defined as the outer edge, is therefore reached prematurely.

In future studies an improvement of the corrections for gradient performance for the radial UTE sequences would prove useful. One such correction was previously performed on this system for the CV UTE sequence.[3] The issue with these improvements is that they are version specific and need to be redone after upgrades of the scanner system version, the advantage is that these corrections are available inside the online reconstruction. A second option would be to implement a post processing k space improvement[2], which would be relatively independent of the system version used but would also require quite a bit of work to be done.

The DA-3DPR sequence would greatly benefit from online reconstruction options and more thorough documentation of the settings available.

Mathematica Analysis Toolkit

A.1 Introduction

This chapter contains the Mathematica[21] program code for the analysis as described in section 2.8.

Please note that some of the settings which need to be adjusted for each slice are inside the functions. These are clearly marked with comments and the word SET.

Scaling of the settings, for different matrix sizes, can be implemented by introducing a scalingFactor and changing all settings to include a rounding and the scalingFactor e.g. `setX` becomes `Round[scalingFactor setX]`.

A.2 Documentation

A.2.1 General Functions

These functions provide general utility features.

```
dicomFindMetaData[dicomMeta_, name_]
```

- Searches a dicom metadata list for a specific key.
- *Parameters*
 - `dicomMeta`: The dicom metadata list
 - `name`: The key to search for
- *Return*: The value associated with the key

`rotateMatrix[matrixIn_, angle_]`

- Rotates the matrix by the given angle cropping it to its original dimensions and using quadratic interpolation.
- *Parameters*
 - `matrixIn`: Input matrix
 - `name`: Rotation angle
- *Return*: Rotated matrix, cropped to original dimensions

A.2.2 Signal to Noise Ratio

This functions provides the analysis functionality for the signal to noise ratio measure.

`snr[data_]`

- Calculates the SNR for a single slice using the masks set in the settings. And as defined by equation 2.2.
- *Parameters*
 - `data`: Input matrix of the slice
- *Return*: SNR as per equation 2.2

A.2.3 Ringing and Edge Overshoot

These functions provide edge analysis functionality.

`edgeAnalysis[data_]`

- Analyzes multiple line profiles inside the single slice provided.
- *Parameters*

- **data:** Input matrix of the slice
- *Return:* Mean of the edge analysis within the single line profiles

A.2.4 Resolution

These functions provide the resolution analysis modules.

Line Spread Function

`lsfSingleLine[matrixIn_, pixelSize_]`

- Calculates the modulation transfer function from the line spread function, as described in section 2.4.1. The resolution criterion used is the one given in equation 2.9.
- *Parameters*
 - **matrixIn:** Input matrix of the slice
 - **pixelSize:** Real number representing the pixel size
- *Return:* Spatial frequency which satisfies the resolution criterion, eq 2.9

Edge Spread Function

`esfSingleLine[matrixIn_, pixelSize_]`

- Calculates the resolution in a single slice by extracting the ESF, calculating the numerical derivative of the ESF, the LSF and calling the `lsfSingleLine` function to analyze the data.
- *Parameters*
 - **matrixIn:** Input matrix of the slice
 - **pixelSize:** Real number representing the pixel size
- *Return:* Spatial frequency which satisfies the resolution criterion, eq 2.9

`esf[matrixInTop_, pixelSizeTop_]`

- Determines the resolution as obtained from the edge spread function from the left and right side, every other line of the edge is used to avoid correlation between neighbouring lines.

- *Parameters*
 - `matrixInTop`: Input matrix of the slice
 - `pixelSizeTop`: Real number representing the pixel size
- *Return*: Resolution in `pixelSize` units (inverted spatial frequency).

Point Spread Function

`psf[matrixIn_, pixelSize_]`

- Calculates the resolution by using the point spread function. The point spread function taken from the center set in `psfCenter` and around radius `radius` is integrated along the y direction and the `esfSingleLine` function is used to analyze the result of this integration.
- *Parameters*
 - `matrixIn`: Input matrix of the slice
 - `pixelSize`: Real number representing the pixel size
- *Return*: Resolution in `pixelSize` units (inverted spatial frequency).

`psfAngle[matrixIn_, pixelSize_, angle_]`

- Calculates the resolution by using the point spread function and rotates the input matrix before performing the calculation. The point spread function taken from the center set in `psfCenter` and around radius `radius` is integrated along the y direction and the `esfSingleLine` function is used to analyze the result of this integration.
- *Parameters*
 - `matrixIn`: Input matrix of the slice
 - `pixelSize`: Real number representing the pixel size
- *Return*: Resolution in `pixelSize` units (inverted spatial frequency).

A.2.5 Geometric Accuracy

`lineDiameter[line_, pixelSize_]`

- Finds the diameter of a single line profile. The criterion used for this is given in equation 2.17.

- *Parameters*
 - `line`: Input line profile
 - `pixelSize`: Real number representing the pixel size
- *Return*: Diameter in `pixelSize` units.

`sliceDiameter[matrixIn_, pixelSize_]`

- Finds the diameter within a whole slice by analyzing several diameters using the `lineDiameter` function and taking the maximum value from the resulting data set.
- *Parameters*
 - `matrixIn`: Input matrix of the slice
 - `pixelSize`: Real number representing the pixel size
- *Return*: Diameter in `pixelSize` units for the input slice.

`diameter[matrixIn_, pixelSize_]`

- Finds the diameter within all rotations of a single slice by using the `sliceDiameter` function for each slice.
- *Parameters*
 - `matrixIn`: Input matrix of the slice
 - `pixelSize`: Real number representing the pixel size
- *Return*: Diameter in `pixelSize` units for the input slice.

A.3 General Functions

```
dicomFindMetaData[dicomMeta_, name_] :=
Module[{dicomList, pos},
  dicomList = List @@@ dicomMeta;

  pos = Position[dicomList, name, 2][[1, 1]];
  dicomList[[pos, 2]]
]

findBelowVal[function_, value_, x0_, xMax_] := Module[
  {increment, xCur},
  increment = 0.0001;
```

```

    xCur = x0;

    (* Search for the first point where the function is smaller than \
our target value *)
    While[xCur <= xMax,
      If[function[xCur] < value,
        Return[xCur]];

    xCur += increment;
  ];

];

(** Rotates the matrix by the given angle
cropping it to its original dimensions and
using quadratic interpolation

@param matrixIn Input matrix
@param angle Rotation angle

@return Rotated matrix, cropped to original dimensions
**)
rotateMatrix[matrixIn_, angle_] :=
  ImageData[
    ImageRotate[
      Image[matrixIn],
      angle,
      Dimensions[matrixIn],
      Resampling -> "Quadratic"
    ]];

(** Converts the value and error
to Latex output with two significant error digits
and correct rounding

@param val Value
@param error Error of value

@return Latex String

**)
Latex[val_, error_] :=
  Module[{valN, errorN, errorSigExponent},
    valN = QuantityMagnitude[val];
    errorN = QuantityMagnitude[error];
    (* Find significant error digit *)

```

```

errorSigExponent = Catch[Do[
  If[Mod[errorN, 10i] != errorN, Throw[i]] ,
  {i, 20, -20, -1}]
];

valN = Round[valN, 10(errorSigExponent - 1)] // N;
errorN = Ceiling[errorN, 10(errorSigExponent - 1)] // N;

"$" <> ToString[valN] <>
" \pm " <>
ToString[errorN] <> "$"
]

```

A.4 Settings

```

maskNoise = Binarize[<insert image>];
maskImageData = Binarize[<insert image>];
psfCenter={142,127};

```

A.5 Signal to Noise Ratio

```

(** Function for calculating the SNR

@param data Input matrix containg the image data
@returns {SNR, sigmaSNR} where SNR is the signal to noise ratio and sigmaSNR the
        standard deviation of this value
**)
snr[data_]:=Module[{noiseTable,imageDataTable,SNR,sigmaSNR},
(* Define hand drawn masks for the noise and image data regions *)

(* Apply the mask by obtaining the matrix representation and then flatten it to
   a table for further statistical analysis *)

noiseTable=Flatten[Pick[data,ImageData@maskNoise,1]];
imageDataTable=Flatten[Pick[data,ImageData@maskImageData,1]];

SNR=Mean[imageDataTable]/StandardDeviation[noiseTable];
sigmaSNR=StandardDeviation[imageDataTable]/(Mean[noiseTable] );

{SNR,sigmaSNR}
];

```

A.6 Ringing and Edge Overshoot

```

(** Analyze mutltiple slices in the edge for overshoot
this can be used as a measure of Gibbs ringing and edge enhancement

@param data Image values matrix
@return Overshoot as a relative value for multiple lines inside the data matrix.

**)
edgeAnalysis[data_]:=Module[{lineAnalysis,linesSelected,lineResults},
(** Analyses a single line in the data

@param line list of values in the line which is to be analysed.
@return overshoot over mean in this line as relative value. 1.0 means no
overshoot
**)
lineAnalysis[line_]:=Module[{mean,xStart,xEnd,overshoot},
(* Calculate mean
SET x Values here *)
xStart=88;
xEnd=170;

mean=Mean[line[[xStart;;xEnd]]];

(* Look only at the left side here *)
overshoot=Max[line]/mean;

(* return *)
overshoot
];

(* SET the lines which will be used *)
linesSelected = Table[i,{i,119,136}];

lineResults=lineAnalysis[data[[#]]]&/@linesSelected;

(* return *)
Mean[lineResults]
];

```

A.7 Resolution

A.7.1 Line Spread Function

```

(** Calculates the edge spread function for a single line and the
resulting mtf resolution value in frequency space where the mtf
obtains a value of 0.5

```

```

@param matrixIn Single line input matrix. CAUTION Single line matrix!
@param pixelSize Pixel size will determine the units of the resulting frequency
    value

@return Frequency Space value where the MTF reaches the value 0.5
**)
lsfSingleLine[matrixIn_, pixelSize_] := Module[
{m, n, l, wMin, wMax, rangeMTF, matrix2dft,
lineSelect, mtfScaled2DFT, mtfNormalized,
interpol, mtfResult, rowSelect, mtfVertical, mtfDiagonal,
interpolVertical, interpolDiagonal, fourierTrans, zeroPadded, lsf},
(* m x n input matrix *)
n = Length[matrixIn];

(* Zero pad the matrix for artificial FFT detail used to find the final value *)
(* Make sure not to truncate the list, by using Max *)
zeroPadded = PadRight[matrixIn, Max[65536, Length[matrixIn]]];

(* Scaling of the MTF x-Axis / spatial frequency *)
l = n * pixelSize;
wMin = 1/l;
wMax = n/l;
rangeMTF = Range[wMin, wMax, (wMax - wMin)/(Length[zeroPadded] - 1)*2];

(***** HORIZONTAL *****)
fourierTrans = Abs[Fourier[zeroPadded]];

(* Correction for having both sides of k space in the Fourier transform in
    Mathematica *)
fourierTrans = Drop[fourierTrans, -(Length[fourierTrans]/2)];

mtfNormalized = fourierTrans / fourierTrans[[1]];

mtfScaled2DFT = Table[{rangeMTF[[i]], mtfNormalized[[i]]}, {i, 1, Length[rangeMTF]}];

For[i = 1, i <= Length[mtfScaled2DFT], i++,
If[mtfScaled2DFT[[i, 2]] <= 0.5,
Return[mtfScaled2DFT[[i, 1]]];
];
];

Return[];
];

```

A.7.2 Edge Spread Function

```

esfSingleLine[matrixIn_, pixelSize_] := Module[{lsf},
  lsf = Differences[
    matrixIn
  ];

  Return[lsfSingleLine[lsf, pixelSize]];
]

(* Returns the resolution as obtained from the edge spread function
from the left and right side, every other line of the edge is used to avoid
correlation between the neighbour lines
@param matrixInTop Input data matrix of the whole dicom image
@param pixelSizeTop Size of a single pixel in the input matrix, these are the
pixels in x direction

@return Mean of the resolution values of both sides an multiple lines
**)
esf[matrixInTop_, pixelSizeTop_] := Module[{extractEsf, esfLeftExtract,
  esfRightExtract,
  resultEsfLeft, resultEsfRight},

  extractEsf[matrixInExtr_] := Module[{xStart, xEnd, yStart, yEnd,
    cutImage, rotatedImageLeft, rotatedImageRight, esfRight, esfLeft},
    (* SET part of image to be used here *)
    xStart = 40;
    xEnd = 110;
    yStart = 30;
    yEnd = 100;

    (* Take only part of the image to continue with *)
    cutImage = Take[matrixInExtr, {yStart, yEnd}, {xStart, xEnd}];

    (* rotate the image so that the edge is aligned along the
y axis *)
    rotatedImageRight = ImageData[
      ImageRotate[
        Image[
          cutImage
        ], -41 Degree]
    (* SET rotation angle for right side here *)
  ];

  rotatedImageLeft = ImageData[
    ImageRotate[
      Image[
        cutImage

```



```

],-39Degree]
(* SET rotation angle for left side here *)
];

(* SET part which is used for the ESF here *)
esfRight = Take[rotatedImageRight,{34,70},{47,70}];
esfLeft = Take[rotatedImageLeft,{34,70},{20,55}];

(* return *)
{esfLeft,esfRight}
];

{esfLeftExtract,esfRightExtract} = extractEsf[matrixInTop];

resultEsfLeft=Table[
esfSingleLine[esfLeftExtract[[i]],pixelSizeTop],
{i,1,Length[esfLeftExtract],2}
];

resultEsfRight=Table[
esfSingleLine[esfRightExtract[[i]],pixelSizeTop],
{i,1,Length[esfRightExtract],2}
];

Mean[Join[1/resultEsfLeft,1/resultEsfRight]]
];

```

A.7.3 Point Spread Function

```

psf[matrixIn_,pixelSize_] := Module[{center,radius,lsf,baseline},
center=psfCenter;
(* Center for 321 \[Mu]m object {142,127} *)
(* Center for 200 \[Mu]m object {104,168} *)
radius=15;

(* Extract the PSF from the total image *)
lsf=Take[matrixIn,
{center[[1]]-radius,center[[1]]+radius},
{center[[2]]-radius,center[[2]]+radius}];

(* Integrate along the y axis *)
lsf=Total[lsf];

(* Calculate a baseline and subtract it *)
baseline=Mean[lsf[[1;;8]]];

```

```

lsf=lsf-baseline;

(* now we can use the lsf module to analyze
the data we have so far *)
Return[1/lsfSingleLine[lsf,pixelSize]];
];

psfAngle[matrixIn_,pixelSize_,angle_]:= Module[{lsf,baseline},
center=psfCenter;
(* Center for 321 \[Mu]m object {142,127} *)
(* Center for 200 \[Mu]m object {104,168} *)
radius=20;

(* Extract the PSF from the total image *)
lsf=Take[matrixIn,
{center[[1]]-radius,center[[1]]+radius},
{center[[2]]-radius,center[[2]]+radius}];

(* Rotate the matrix by the given angle *)
lsf=ImageData[ImageRotate[Image[lsf],angle,"SameRatioCropping"]];

(* Sometimes white pixels are encountered along the outer
edge, this causes servere issues with the analysis, therefore
cut the border out *)

lsf=Take[lsf,{2,Dimensions[lsf][[1]]-1},{2,Dimensions[lsf][[2]]-1}];

(* Integrate along the y axis *)
lsf=Total[lsf];

(* Calculate a baseline and subtract it *)
baseline=Mean[lsf[[1;;8]]];

lsf=lsf-baseline;

(* now we can use the lsf module to analyze
the data we have so far *)
Return[1/lsfSingleLine[lsf,pixelSize]];
];

```

A.8 Geometric Accuracy

```

(** Finds the diameter in a single line profile
by looking for the first and last position where the

```

```

intensity reaches a value of  $1/\sqrt{2}$   $I_{\max}$  or more

@param line Line profile
@param pixelSize Size of a single pixel

@return Diameter of this line given by the criterion above

*)
lineDiameter[line_, pixelSize_] := Module[{firstPos, lastPos, maxI},
  firstPos = Null;
  lastPos = Null;
  maxI = Mean[line];

  (* firstPos Search *)
  For[i = 1, i <= Length[line], i++,
    If[line[[i]] >= 1/Sqrt[2] maxI,
      firstPos = i;
      Break[];
    ]
  ];

  (* lastPos Search *)
  For[i = Length[line], i >= 1, i--,
    If[line[[i]] >= 1/Sqrt[2] maxI,
      lastPos = i;
      Break[];
    ]
  ];

  Return[(lastPos - firstPos)*pixelSize];

];

(** Finds the maximum diameter within a single slice

@param matrixIn Input slice as a 2D matrix
@param pixelSize Size of a single pixel

@return Maximum diameter within this slices,
criterion as described in lineDiameter function

*)
sliceDiameter[matrixIn_, pixelSize_] :=
Module[{diameterSet, start, end},
  start = Round[Length[matrixIn]/4];
  end = Length[matrixIn] - start;

  diameterSet =

```

```

    lineDiameter[#, pixelSize] & /@ matrixIn[[start ;; end]];

Return[Max[diameterSet]];

];

diameter[matrixIn_, pixelSize_] := Module[{allRotations},
  allRotations =
    Table[sliceDiameter[rotateMatrix[matrixIn, i Degree], pixelSize],
      {i, 0, 180, 10}];

  Return[{Mean[allRotations], StandardDeviation[allRotations]}];
];

```

A.9 Usage Example

```

(*Load Data*)
dicomData = Import[#, "Data"]&/@sliceFiles;
dicomMeta = Import[#, "MetaInformation"]&/@sliceFiles;

(* sliceFiles is a list of DICOM slice file paths *)

(*Signal to Noise Ratio*)
snrAllSlices=Parallelize[snr/@dicomData[[All,1]]];

snrMean=Mean[snrAllSlices[[All,1]]];
snrError=StandardDeviation[snrAllSlices[[All,1]]]/Sqrt[Length[snrAllSlices[[All,1]]]];

snrMeanCorrected=snrMean*0.655;
snrErrorCorrected =snrError*0.655;

(*Edge Analysis*)
edgeAllSlices=Parallelize[edgeAnalysis/@dicomData[[All,1]]];

edgeMean=Mean[edgeAllSlices];
edgeError=StandardDeviation[edgeAllSlices]/Sqrt[Length[edgeAllSlices]];

(*Edge Spread Function*)
(* The factor 1/5 is necessary for the 7T micro imaging system, to convert
pixel size inside the system to actual pixel size *)
pixelSize=dicomFindMetaData[dicomMeta[[1]], "PixelSpacing"]/5;

esfAllSlices=Parallelize[esf[#,pixelSize[[1]]]&/@ dicomData[[All,1]]];

esfMean=Mean[esfAllSlices]*1000 ;

```

```

esfError=StandardDeviation[esfAllSlices]/Sqrt[Length[esfAllSlices]]*1000;

(* POINT SPREAD FUNCTION *)
(*Integrated in y Direction*)
psfAllSlices=Parallelize[psf[#,pixelSize[[1]]]&/@ dicomData[[All,1]]];
psfAllSlices=DeleteCases[psfAllSlices, _?(Not[NumberQ[#]]&)];

psfMean=Mean[psfAllSlices]*1000 ;psfError=StandardDeviation[psfAllSlices]/Sqrt[
    Length[psfAllSlices]]*1000 ;

(*Integrated in x Direction*)
psfAllSlicesX=psfAngle[#,pixelSize[[1]],90 Degree]&/@ dicomData[[All,1]]];
psfAllSlicesX=DeleteCases[psfAllSlicesX, _?(Not[NumberQ[#]]&)];

psfMeanX=Mean[psfAllSlicesX]*1000 ;psfErrorX=StandardDeviation[psfAllSlicesX]/
    Sqrt[Length[psfAllSlicesX]]*1000 ;

(*Geometric Accuracy*)
diameterAllSlices=Parallelize[diameter[#,pixelSize[[1]]]&/@dicomData[[All,1]]];

diameterMean=Mean[diameterAllSlices[[All,1]]];diameterStandardError=
    StandardDeviation[diameterAllSlices[[All,1]]]/Sqrt[Length[diameterAllSlices
    [[All,1]]]];

diameterStandardDeviation=Mean[diameterAllSlices[[All,2]]];
diameterStandardDeviationStandardError=StandardDeviation[diameterAllSlices[[All
    ,2]]]/Sqrt[Length[diameterAllSlices[[All,2]]]];

diameterStandardDeviationRel = diameterStandardDeviation/diameterMean;
diameterStandardDeviationStandardErrorRel =
    diameterStandardDeviationStandardError/diameterMean;

```

A.10 Difference Images SNR

```

analyzeDiffSNR[n_]:=Module[{},diffSlices=usedSlices[[n]]-usedSlices[[n+1]];
maskImageData=Binarize[(* Signal area mask *)];

newWidth=Round[ImageDimensions[maskNoise][[1]]*scalingFactor];

maskNoise=ImageResize[maskNoise,newWidth];
maskImageData=ImageResize[maskImageData,newWidth];
(* Apply the mask by obtaining the matrix representation and then flatten it to
    a table for further statistical analysis *)

noiseTable=Flatten[Pick[diffSlices,ImageData@maskImageData,1]];
imageDataTable=Flatten[Pick[usedSlices[[n]],ImageData@maskImageData,1]];

```

```
SNR=Mean[imageDataTable]/(StandardDeviation[noiseTable] / Sqrt[2]);

SNR]
```

A.11 T1 Analysis

This listing shows the Mathematica [21] code used for the analysis of the T1 of the phantoms silicone material.

```
Needs["ErrorBarPlots`"]

dicomFindMetaData[dicomMeta_, name_] :=
Module[{dicomList, pos},
  dicomList = List @@@ dicomMeta;

  pos = Position[dicomList, name, 2][[1, 1]];
  dicomList[[pos, 2]]
]

loadSlice[directory_, seq_, slice_] :=
  FileNames[
    directory <> "*.MR.SEQUENCEREGION_USERSEQUENCES_VB17." <> seq <>
    "." <> slice <> "*.IMA"];

dir = "T:\\Documents\\MSc\\Messdaten\\2015_09_12-uniform\\";

loadSequenceSlice[dir_, seqStart_, seqEnd_, sliceNr_] :=
  Table[loadSlice[dir, IntegerString[i, 10, 4],
    IntegerString[sliceNr, 10, 4]][[1]], {i, seqStart, seqEnd}];

signalAnalysisSingleMatrix[matrixIn_] := Module[{mask, signalData},
  mask = Binarize[\\!\\(\\*
GraphicsBox[
{EdgeForm[{GrayLevel[1.], Opacity[1.], AbsoluteThickness[1]}],
  DiskBox[{74.2330623306233, 64.17344173441735},
    42.67935563844658]}],
Background->GrayLevel[0],
BaseStyle->GrayLevel[1],
ImagePadding->{{0., 0.}, {0., 0.}},
ImageSizeRaw->{128, 128},
PlotRange->{{0., 128.}, {0., 128.}},
PlotRangePadding->Automatic]\\);
  signalData = Flatten[Pick[matrixIn, ImageData@mask, 1]];

  Return[{Mean[signalData],
```

```

        StandardDeviation[signalData]/Sqrt[Length[signalData]]}];

];

signalT1singleSlice[data_, metaData_] := Module[{analysis, tr},
  analysis = signalAnalysisSingleMatrix[data];

  tr = dicomFindMetaData[metaData, "RepetitionTime"]/1000;

  {{tr, analysis[[1]]}, ErrorBar[analysis[[2]]]}

];

signalT1data[dir_, seqStart_, seqEnd_, sliceNr_] :=
Module[{fileList, dicomMeta, result, max, scale},
  fileList = loadSequenceSlice[dir, seqStart, seqEnd, sliceNr];

  (*Load Data*)
  dicomData = Import[#, "Data"] & /@ fileList;
  dicomMeta = Import[#, "MetaInformation"] & /@ fileList;

  result =
    Table[signalT1singleSlice[dicomData[[i, 1]], dicomMeta[[i]]], {i,
      1, Length[dicomData]}];

  max = First[result][[1, 2]];

  scale[in_] := in/max;

  (* rescale intensity and y error to relative scale from 0 to 1 *)
  result = MapAt[scale, result, {{All, 1, 2}, {All, 2, 1}}];

  Return[result];

];

fitT1[data_] := Module[{dataForFit, fit},
  dataForFit = data[[All, 1]];

  fit = NonlinearModelFit[dataForFit, M0 (1 - Exp[-tr/t1]),
    {{M0, 1}, {t1, 1.4}}, tr];

  Return[fit];
];

```


Simulations

B.1 XD VTE K Space Distortion

```

(* Generate image for simulation *)
diskImg=Rasterize[Graphics[Disk[]],ImageSize->230,AspectRatio->1]
diskNeg=ColorNegate[diskImg]
diskFinished=ColorConvert[ImagePad[diskNeg,{{13,13},{13,13}}],GrayLevel]
diskData=ImageData[diskFinished];

(* Perform DST Fourier transform and normalize *)
coef=FourierDST[diskData,1]1/Sqrt[Length[diskData]];

(* Weighting function and weights for manipulation of k space *)
cutOff=35;

weightFunc[x_]:=If[x<= cutOff,
1,
Exp[-(x-cutOff)/10]
]

weights2=Table[weightFunc[j],{i,1,256},{j,1,256}];

(* Simulation of the k space effect *)
simResult=FourierDST[coef*weights2,1];

(* Output image generation *)
outImage=ImageAdjust[Image[simResult,{1.9,7}];

```


Curriculum Vitae

Persönliche Daten

Fabian Valka, BSc
Währinger Straße 115/4
1180 Wien

Telefon: +43 (699) 129 167 69
E-Mail: fabian.valka@univie.ac.at

Geboren am 6. Juni 1985 in Wien

Ledig

Schulbildung

09/2003-03/2007 Berufsschule für Informationstechnologie
Lehre als IT-Informatiker

10/2006-10/2007 VHS21, Höhere Bundeslehranstalt für wirtschaftliche Berufe
Berufsreifeprüfung

Zivildienst

10/2007-06/2008 Berufsrettung Wien
Rettungssanitäter

Studienverlauf

10/2008-01/2009 Medizinische Universität Wien
Humanmedizin
nicht abgeschlossen

03/2009-03/2013 Universität Wien
Bachelor of Science in Physik

Studienschwerpunkte:

- Experimentalphysik
- Computational physics
- Umwelt und Biophysik

Bachelorarbeit:

“Development of a Multi Step Controller for the Cooling System of the Vienna Environmental Research Accelerator”

zusätzliche Lehrveranstaltungen aus Mathematik

03/2013-laufend Universität Wien
Master of Science in Physik

Studienschwerpunkte:

- Medizinische Physik
- Experimentalphysik
- Quantenphysik

Masterarbeit extern an der Medizinischen Universität Wien

Auslandsaufenthalte

08/2012-02/2013 Aarhus University, Dänemark
Im Rahmen des Erasmusprogramms.

Schwerpunkte:

- Experimentalphysik
- Regelungstechnik
- Windenergie

Berufserfahrung

- 06/2003-07/2006 BitXtreme
 Lehre Informationstechnologie Informatik
- 06/2009-laufend Vektorraum
 Selbständig als Softwareentwickler
- 10/2011-01/2012 Universität Wien
 Projektmitarbeiter am VERA
- 04/2014-06/2014 Universität Wien
 Karenzvertretung als Techniker, Elektroniker

Sprachkenntnisse

Deutsch, Muttersprache

Englisch, Fließend

Wien, November 2, 2015

Bibliography

- [1] M. D. Robson, P. D. Gatehouse, M. Bydder, and G. M. Bydder. Magnetic resonance: an introduction to ultrashort TE (UTE) imaging. *J Comput Assist Tomogr*, 27(6):825–846, 2003.
- [2] Masahiro Takizawa, Hikaru Hanada, Kuniharu Oka, Tetsuhiko Takahashi, Etsuji Yamamoto, and Masahiko Fujii. A robust ultrashort te (ute) imaging method with corrected k-space trajectory by using parametric multiple function model of gradient waveform. *IEEE Trans. Med. Imaging*, pages 306–316, 2013.
- [3] C. Horn. Parameter selective mr-microimaging of biomaterials with short t2s. Master’s thesis, TU Wien, 2012.
- [4] NEMA Standards Publication. *Determination of signal-to noise ratio (SNR) in diagnostic magnetic resonance imaging*. National Electrical Manufacturers Association, 2001.
- [5] Lars G Hanson. Is quantum mechanics necessary for understanding magnetic resonance? *Concepts in Magnetic Resonance Part A*, 32(5):329–340, 2008.
- [6] G. E. Boyle, M. Ahern, J. Cooke, N. P. Sheehy, and J. F. Meaney. An interactive taxonomy of MR imaging sequences. *Radiographics*, 26(6):e24; quiz e24, 2006.
- [7] Erwin L Hahn. Spin echoes. *Physical review*, 80(4):580, 1950.
- [8] Damian J Tyler, Matthew D Robson, R Mark Henkelman, Ian R Young, and Graeme M Bydder. Magnetic resonance imaging with ultrashort te (ute) pulse sequences: technical considerations. *Journal of Magnetic Resonance Imaging*, 25(2):279–289, 2007.
- [9] X Deligianni, P B K Scheffler, S Trattnig, and O Bieri. High-resolution fourier-encoded sub-millisecond echo time musculoskeletal imaging at 3 tesla and 7 tesla. *Magnetic Resonance in Medicine*, 70(5):1434–1439, 2013.
- [10] Marcin Wojdyr. *Fityk*: a general-purpose peak fitting program. *Journal of Applied Crystallography*, 43(5 Part 1):1126–1128, Oct 2010. doi: 10.1107/S0021889810030499. URL <http://dx.doi.org/10.1107/S0021889810030499>.

- [11] V. Jellus, P. Speier, and T. Benner. Applications guide ute 3d imaging with ultrashort echo times (work-in-progress), Jul 2011.
- [12] C. F. Chan, N. G. Keenan, S. Nielles-Vallespin, P. Gatehouse, M. N. Sheppard, J. J. Boyle, D. J. Pennell, and D. N. Firmin. Ultra-short echo time cardiovascular magnetic resonance of atherosclerotic carotid plaque. *J Cardiovasc Magn Reson*, 12:17, 2010.
- [13] A. M. Nagel, F. B. Laun, M. A. Weber, C. Matthies, W. Semmler, and L. R. Schad. Sodium MRI using a density-adapted 3D radial acquisition technique. *Magn Reson Med*, 62(6):1565–1573, Dec 2009.
- [14] Bruker. *Paravision 6.0 operating manual*. Bruker, 2014.
- [15] Richard P Feynman, Frank L Vernon Jr, and Robert W Hellwarth. Geometrical representation of the schrödinger equation for solving maser problems. *Journal of applied physics*, 28(1):49–52, 1957.
- [16] DI Hoult. The origins and present status of the radio wave controversy in nmr. *Concepts in Magnetic Resonance Part A*, 34(4):193–216, 2009.
- [17] Lars G Hanson. Introduction to Magnetic Resonance Imaging techniques, August 2009.
- [18] W. R. Nitz and P. Reimer. Contrast mechanisms in MR imaging. *Eur Radiol*, 9(6):1032–1046, 1999.
- [19] G. B. Chavhan, P. S. Babyn, B. Thomas, M. M. Shroff, and E. M. Haacke. Principles, techniques, and applications of T2*-based MR imaging and its special applications. *Radio-graphics*, 29(5):1433–1449, 2009.
- [20] D. B. Twieg. The k-trajectory formulation of the NMR imaging process with applications in analysis and synthesis of imaging methods. *Med Phys*, 10(5):610–621, 1983.
- [21] Wolfram Research, Inc. Mathematica 10.0. URL <https://www.wolfram.com>.
- [22] L Kaufman, D M Kramer, L E Crooks, and D A Ortendahl. Measuring signal-to-noise ratios in MR imaging. *Radiology*, 173(1):265–267, October 1989. ISSN 0033-8419. doi: 10.1148/radiology.173.1.2781018. PMID: 2781018.
- [23] M J Firbank, A Coulthard, R M Harrison, and E D Williams. A comparison of two methods for measuring the signal to noise ratio on mr images. *Physics in Medicine and Biology*, 44(12):N261, 1999. URL <http://stacks.iop.org/0031-9155/44/i=12/a=403>.
- [24] M. J. Firbank, R. M. Harrison, E. D. Williams, and A. Coulthard. Quality assurance for MRI: practical experience. *Br J Radiol*, 73(868):376–383, Apr 2000.

-
- [25] A. Kayugawa, M. Ohkubo, and S. Wada. Accurate determination of CT point-spread-function with high precision. *J Appl Clin Med Phys*, 14(4):3905, 2013.
 - [26] M. D. Robson, J. C. Gore, and R. T. Constable. Measurement of the point spread function in MRI using constant time imaging. *Magn Reson Med*, 38(5):733–740, Nov 1997.
 - [27] J.W. Goodman. *Introduction to Fourier Optics*. McGraw-Hill, 2nd edition, 1996.
 - [28] S. Smith. *Digital Signal Processing: A Practical Guide for Engineers and Scientists: A Practical Guide for Engineers and Scientists*. Demystifying technology series. Elsevier Science, 2013. ISBN 9780080477329.
 - [29] The American College of Radiology. Phantom test guidance for the acr mri accreditation program, 2005.
 - [30] J.T. Bushberg. *The Essential Physics of Medical Imaging*. Lippincott Williams & Wilkins, 2001. ISBN 9780683301182.
 - [31] E. Han G. Bydder M. Carl, J-T. Chiang and K. King. Bloch Simulations of UTE, WASPI and SWIFT for imaging short T2 tissues. *Proc. Intl. Soc. Mag. Reson. Med.*, 18, 2010.
 - [32] J. Rahmer, P. Bornert, J. Groen, and C. Bos. Three-dimensional radial ultrashort echo-time imaging with T2 adapted sampling. *Magn Reson Med*, 55(5):1075–1082, May 2006.
 - [33] E. Pusey, R. B. Lufkin, R. K. Brown, M. A. Solomon, D. D. Stark, R. W. Tarr, and W. N. Hanafee. Magnetic resonance imaging artifacts: mechanism and clinical significance. *Radiographics*, 6(5):891–911, Sep 1986.
 - [34] C.D. Gregory. MRI artefact gallery, April 1997. URL <http://chickscope.beckman.uiuc.edu/roosts/carl/artifacts.html>. Accessed: 2015-10-03.
 - [35] Allen D Elster. Sellar susceptibility artifacts: theory and implications. *American journal of neuroradiology*, 14(1):129–136, 1993.
 - [36] D. Weishaupt, V.D. Köchli, and B. Marincek. *How does MRI work?: An Introduction to the Physics and Function of Magnetic Resonance Imaging*. Springer Berlin Heidelberg, 2006. ISBN 978-3-540-37845-7.
 - [37] M. Bencsik, A. Al-Rwaili, R. Morris, D. J. Fairhurst, V. Mundell, G. Cave, J. McKendry, and S. Evans. Quantitation of MRI sensitivity to quasi-monodisperse microbubble contrast agents for spatially resolved manometry. *Magn Reson Med*, 70(5):1409–1418, Nov 2013.
 - [38] Silikonfabrik.de. Online datasheet for "Silikon SF00", 2015. URL http://www.silikonfabrik.de/product_info.php?info=p2_Silikon-SF00---0-5-KG.html. Accessed: 2015-10-03.

- [39] L. Petrakis. Spectral line shapes: Gaussian and lorentzian functions in magnetic resonance. *Journal of Chemical Education*, 44(8):432, 1967. doi: 10.1021/ed044p432.
- [40] P. S. Tofts. Methods for quantitative relaxation parameter mapping: measuring T1 and T2. ISMRM April 18th 2009 Hawaii, 2009. URL http://www.paul-tofts-phd.org.uk/talks/ismrm2009_rt.pdf.
- [41] Victor R Vasquez and Wallace B Whiting. Accounting for both random errors and systematic errors in uncertainty propagation analysis of computer models involving experimental measurements with monte carlo methods. *Risk analysis: an official publication of the Society for Risk Analysis*, 25(6):1669–1681, December 2005. ISSN 0272-4332. doi: 10.1111/j.1539-6924.2005.00704.x. PMID: 16506991.
- [42] R. I. Grossman, J. M. Gomori, K. N. Ramer, F. J. Lexa, and M. D. Schnall. Magnetization transfer: theory and clinical applications in neuroradiology. *Radiographics*, 14(2):279–290, Mar 1994.
- [43] U. Tietze and C. Schenk. *Halbleiter-Schaltungstechnik: [neuer Teil: Nachrichtentechnische Schaltungen]*. Springer, 2002. ISBN 9783540428497.
- [44] A. Nagl. DA-3DPR sequence installation guide.